THE UNIVERSITY *of* EDINBURGH

Measurements of $B^{\pm}$ Meson Production at LHCb and Characterisation of Hybrid Photon Detectors

Ross Young

Thesis submitted for the degree of Doctor of Philosophy

School of Physics & Astronomy
The University of Edinburgh
2012

Abstract

LHCb is an experiment designed to make precision measurements of Charge-Parity violation in the B meson system. We report a measurement of the $B^{\pm}$ cross-section and production asymmetry, using $B^{\pm} \rightarrow J/\psi K^{\pm}$ decays collected at the LHCb detector in 2010 and 2011. Using 27.6 pb^{-1} of pp collisions at a centre-of-mass energy 7 TeV, we obtain a $B^{\pm}$ cross-section of [41.6 $\pm$ 0.6 (stat.) $\pm$ 3.0 (sys.) $\pm$ 4.2 (lumi.)] μb in the rapidity region 2 to 4.5. Using 371.1 pb^{-1} of pp collisions at a centre-of-mass energy 7 TeV, we obtain a $B^{\pm}$ production asymmetry of [$-$2.09 $\pm$ 1.20 $\pm$ 0.8 (CP)]% in the same rapidity region. The Ring Imaging Cherenkov system of LHCb uses Hybrid photon detectors (HPDs) for single photon detection. This thesis summarises the use of ion feedback measurements as indicators of HPD vacuum quality.

Declaration

This work represents the concerted effort of the LHCb collaboration, of which I have been member since starting my PhD. I have been actively involved in the LHCb-RICH group, working on the characterisation of the Hybrid Photon Detectors. The work presented in this thesis has not been submitted for any other degree or professional qualification except as specified. The data analysis procedures and writing of the thesis have been entirely my own work.

Acknowledgements

First of all, I'd like to thank my family for their love and support, without which I don't think I could have done this. They are always a great inspiration to me.

I'd like to thank all of my colleagues at the Particle Physics Experiment group for giving me the opportunity to undertake this PhD and making me feel very welcome. I'd like to thank in particular my supervisor Steve Playfer for his continued help and patience throughout my course, and I'm grateful for all the advice he gave to me. Thanks also to my second supervisor Stephan Eisenhardt for his guidance on the study of Hybrid Photon Detectors, and to Thierry Gys and the rest of the LHCb-RICH group for their help while I was working at CERN. I'd also like to thank the postgraduate school secretary Jane Patterson who has always provided the best help whenever I needed it. I greatly thank the Science and Technology Facilities Council for funding my PhD both here and at CERN.

My Edinburgh and Geneva friends have been amazing and I thank you all for the unforgettable times, as well as the hazy ones. I'd like to thank my worthy office chair-jousting foe Gemma, my other big sister Hajrah, Dr Pearce, Conor the barman-ian, and many more for putting up with me and giving me some great laughs.

Contents

List of Figures

List of Tables

Chapter 1

Introduction

One of the fundamental questions asks why our universe exists naturally as matter and not anti-matter? If there were any region of antimatter within our local cluster of galaxies, we would be able to see radiation from matter—anti-matter annihilations at the boundaries. We know that just one second after the Big Bang, antimatter had all but disappeared, leaving matter to form everything that we see around us—from the stars and galaxies, to the Earth and all life that it supports.

In 1967, Andrei Sakharov proposed a set of three necessary conditions [1] that a baryon-generating interaction must satisfy to produce matter and antimatter at different rates, one of which is CP violation. First observed in 1964 for the weak interaction of kaon decays [2], CP violation describes the breaking of the laws of physics under a combined charge (C) and parity (P) inversion. Maskawa and Kobayashi extended the CP violation formalism to include three generations of quarks [3], a prediction that was confirmed experimentally four years later by the discovery of the bottom quark [4].

The Standard Model is a way in which the matter particles, and the particles mediating the interactions, can be described in a unified way. Over time and through many experiments by many physicists, the Standard Model has become established as a well-tested physics theory. Nevertheless, the level of CP violation predicted within the framework of the Standard Model is too small to explain the observed dominance of matter over anti-matter. The subtle manifestations of

CP violation in the B-meson (bottom) and D-meson (charm) system have been proposed, which may provide explanations of CP violation in the realm of new physics.

November 2009 was a landmark for the scientific community, which saw the most powerful physics experiment that has ever been built, the Large Hadron Collider (LHC), become operational and begin taking data. The LHC collides particles at the tera-electron-volt scale, recreating the conditions that existed a fraction of a second after the Big Bang. The Large Hadron Collider beauty (LHCb) experiment exploits the abundance of available B-hadrons to make precision measurements of CP violating parameters and rare decays in the B-meson system. The results obtained from this experiment will provide the greatest scrutiny of the Standard Model in this region of physics.

This thesis outlines the testing of Hybrid Photon Detectors for the LHCb experiment at CERN, and an analysis of the decay $B^{\pm} \rightarrow J/\psi K^{\pm}$. Chapter 2 gives a brief introduction of the Standard Model and the CP violating mechanisms it predicts. In Chapter 3, an introduction to the LHC leads on to an overview of LHCb, with particular focus on the aspects of the detector that are relevant to this physics analysis. Chapter 4 describes the operation of the Hybrid Photon Detectors for fast, low noise and sensitive photon detection in the LHCb Cherenkov counters. Chapters 5, 6 and 7 detail a measurement of the $B^{\pm}$ cross-section and asymmetry using $B^{\pm} \rightarrow J/\psi K^{\pm}$ decays, beginning with an introduction to the measurements (Chapter 5), then an analysis using simulated data (Chapter 6), and finally a confirmation of the analysis using collision data (Chapter 7). A summary of the thesis findings can be found in Chapter 8.

Chapter 2

Theoretical Overview

2.1 Standard Model

The fundamental particles of the Standard Model (SM) can be split into two distinct groups: *fermions* and *bosons*. Fermions are spin-1/2 particles obeying Fermi-Dirac statistics, and can be further divided into the *quarks* and *leptons* that constitute the matter of our universe. Bosons are integral spin particles obeying Bose-Einstein statistics that mediate the interaction forces between quarks and leptons.

The properties of all observed leptons [5] are listed in Table 2.1. Under the weak interaction, the leptons form doublets, each consisting of a charged and neutral lepton (neutrino). Though there is no theoretical constraint on the number of allowed generations in the Standard Model, only three generations have experimentally been observed. All leptons can participate in the weak interaction, whereas only charged leptons can participate in the electromagnetic interaction. While the neutrinos and e^- are stable, heavier charged leptons have a relatively short lifetime, and quickly decay through the weak interaction to lighter leptons as observed for the muon decay:

$$\mu^- \rightarrow e^- + \overline{\nu_e} + \nu_\mu \tag{2.1}$$

Lepton number is a conserved quantity for each generation (e, μ, τ), with each lepton assigned +1 and anti-lepton –1. There is a difficulty in measuring neutrino properties as, unlike the charged leptons that participate in the electromagnetic interaction, neutrinos can participate in only the weak interaction. Though the neutrinos are predicted to have zero mass in the Standard Model, evidence for non-zero mass differences has been found through the observation of neutrino oscillations between generations. One of the primary goals of the T2K experiment is a measurement of the mass mixing parameters by detecting the appearance of electron neutrinos (ν_e) from an almost pure muon neutrino beam. As reported in Ref. [6], 6 ν_e pass the selection criteria, while the expected number of background events—assuming no mass mixing—is 1.5 $\pm$ 1.3 (syst.). The probability to observe six or more candidate events due to background is 0.7%, equivalent to 2.5 σ significance.

Flavour	Mass (GeV/c)	Mean Life (s)	Electric Charge
Electron (e^-)	0.5110	> 4.6 x 10^{26} yr	$-e$
Electron neutrino (ν_e)	0^{SM}	Unknown	0
Muon (μ^-)	105.658	2.197 x 10^{-6}	$-e$
Muon neutrino (ν_μ)	0^{SM}	Unknown	0
Tau (τ^-)	1777	(290.6 $\pm$ 1.0) x 10^{-15}	$-e$
Tau neutrino (ν_τ)	0^{SM}	Unknown	0

Table 2.1: Properties of the SM leptons. Neutrinos are predicted to be massless according to the SM (as denoted by the 0^{SM} terms) though non-zero mass differences have been found by various experiments.

Quarks, like leptons, are fundamental fermions. The properties of the Standard Model [5] quarks are listed in Table 2.2. There are 6 different types, or *flavours*, of quark that have so far been experimentally observed, defined as *up, down, strange, charm, top, bottom*. They can be further categorised into three generations of weak doublets, consisting of an up-type quark of electric charge $+\frac{2}{3}$ and a down-type quark of electric charge $-\frac{1}{3}$. Changes in the flavour of a quark is possible via the weak interaction, though the net number of participating quarks never changes, as observed in the weak decay of a neutron:

$$\mathrm{n} \rightarrow \mathrm{p} + \mathrm{e}^- + \overline{\nu_e} \tag{2.2}$$

Quarks also participate in the strong interaction, the consequence of which is that these elementary particles do not exist isolated in nature but are confined in multi-quark systems called hadrons. The bare quark masses are difficult to determine, as the majority of the energy contribution in a hadron comes from the binding gluon fields. The quark masses, listed in Table 2.2, have been obtained with non-perturbative quantum chromodynamics (QCD) calculations. The associated uncertainties are related to the renormalisation scheme of the strong coupling α_s. QCD calculations of the $b\overline{b}$ quark pair cross-section are described in more detail in Chapter 5.

Flavour	Mass	Electric Charge
Up (u)	(3.02 ± 0.33) MeV/c^2	$+\frac{2}{3}e$
Down (d)	(5.49 ± 0.39) MeV/c^2	$-\frac{1}{3}e$
Strange (s)	$0.101^{+0.029}_{-0.021}$ GeV/c^2	$-\frac{1}{3}e$
Charm (c)	$1.27^{+0.07}_{-0.09}$ GeV/c^2	$+\frac{2}{3}e$
Bottom (b)	$4.19^{+0.18}_{-0.06}$ GeV/c^2	$-\frac{1}{3}e$
Top (t)	$172.0 \pm 0.9 \pm 1.3$ GeV/c^2	$+\frac{2}{3}e$

Table 2.2: Properties of the SM quarks. The bare masses for the u and d quark have been obtained from Ref. [7]; for the s, c, b, and t quark have been obtained from Ref. [5].

There are four fundamental types of interaction that exist in nature, defined as the strong, electromagnetic, weak and gravitational interaction. The interactions are mediated not through direct fermion interaction but through the exchange of virtual particles, referred to as *gauge bosons*. The properties of the SM bosons [5] are shown in Table 2.3. Many of the miraculous properties of the fundamental interactions stem from gauge symmetry, that is, an invariance of observable quantities e.g. charge, to a change (gauge transformation) in the underlying field. The force-carrying bosons arise from a *local* gauge symmetry, where the transformations are applied independently at each space-time point.

Invariance under $SU(2)_L \times U(1)_Y$ group transformations leads to the electroweak theory, a theory that unifies the description of interactions involving photons and the weak bosons $W^{\pm}$, Z^0. This is described in more detail in section 2.1.1. Similarly, invariance under SU(3) group transformations leads to the theory of Quantum Chromo-Dynamics (QCD), in which the colour forces are transmitted by colour gauge bosons referred to as *gluons*. This is described in more detail

in section 2.1.2. In order to explain the observed non-zero masses of the weak $W^{\pm}$, Z^0 bosons and the charged fermions it is assumed that the $SU(2)_L \times U(1)_Y$ symmetry is '*spontaneously*' broken. One of the proposed symmetry breaking mechanisms is the Higgs model, described in section 2.1.3. The introduction of three quark generations allows the possibility of flavour mixing within the SM, which is described in section 2.1.4. This concludes with the description of Charge-Parity (CP) violation and its various manifestations, in section 2.1.5. On the scales of particle physics, gravitational forces are insignificant, and the consideration of the gravitational field is excluded from this thesis.

Force	Boson	Mass (GeV)	Spin	Range (m)
Strong	gluons (g)	0	1	10^{-15}
Electromagnetic	photons (γ)	0	1	∞
Weak	$W^{\pm}$	80.399 ± 0.023	1	10^{-18}
	Z^0	91.188 ± 0.002	1	10^{-18}
Gravitation	gravitons		2	∞

Table 2.3: Properties of the SM bosons.

2.1.1 Electroweak Interaction

The electromagnetic field acts on particles with electric charge. It appears as a consequence of the invariance of the Lagrangian under a local U(1) transformation, which leads to the conservation of charge. The formulation of the underlying theory of Quantum Electrodynamics (QED) results in the quantisation of the force-carrying particles called *photons*. The photon couples to all charged particles (including quarks and charged leptons) but does not self-interact as it carries no charge. In QED, the coupling between the radiation field and fermionic field is determined by the charge on the electron e. It is natural to introduce the dimensionless parameter α, the fine structure constant:

$$\alpha_{em} = \frac{e^2}{4\pi\hbar c} \approx \frac{1}{137} \tag{2.3}$$

α_{em} is an experimentally-determined quantity that characterises the strength of the electromagnetic coupling. Figure 2.1.1 depict a particular type of $2 \rightarrow$

2 QED process called s-channels. The momentum transfer is defined by the lorentz-invariant Mandelstam variable s, and is equal to the squared centre-of-mass energy of the incoming particles.

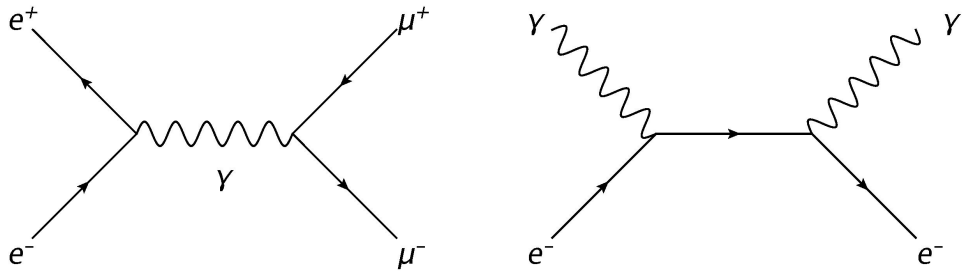

Figure 2.1: Feynman diagrams (time on the x-axis; space on the y-axis) of QED processes at the leading order: (left) s-channel electron-positron annihilation producing a $\mu^+\mu^-$ pair; (right) elastic scattering of photon and electron.

The weak interaction, so named because of its much smaller coupling strength compared to the electromagnetic and strong interactions, is mediated through the exchange of virtual $W^{\pm}$ or Z bosons. Compared to the massless photon that has an unlimited range, the weak interaction has a short-range (10^{-18} m) due to the large $W^{\pm}$ and Z boson masses.

Although at low energies the electromagnetic and weak interactions can be treated separately, it was the pioneering work of S. Glashow, S. Weinberg, and A. Salam [8] that unified the forces into a single interaction, the *electroweak* interaction. The unified electroweak interaction is described by the $SU(2)_L \times U(1)_Y$ gauge group.

Gauge invariance under an $SU(2)_L$ transformation can be preserved with the introduction of a vector gauge field $W_\mu(x)$. The generators of the $SU(2)_L$ group, defined as τ^k below, are identical to the Pauli spin matrices:

$$W_\mu(x) = {W_\mu}^k(x)\tau^k = \begin{pmatrix} {W_\mu}^3 & {W_\mu}^1 - i{W_\mu}^2 \\ {W_\mu}^1 + i{W_\mu}^2 & -{W_\mu}^3 \end{pmatrix} \tag{2.4}$$

The physical W^+ and W^- bosons carry an electric charge and are said to mediate the weak *charged-current* interactions. They can be expressed as linear combinations of the gauge field components ${W_\mu}^1$ and ${W_\mu}^2$:

$$\mathrm{W}^+ \equiv \frac{\mathrm{W}_1 + \mathrm{W}_2}{\sqrt{2}} \tag{2.5}$$

$$\mathrm{W}^- \equiv \frac{\mathrm{W}_1 - \mathrm{W}_2}{\sqrt{2}} \tag{2.6}$$

The L subscript indicates that the SU(2) transformation acts only on left-handed fermion doublets (and equivalently, right-handed antifermion doublets). This is known as parity violation of the particle helicity, and was first observed in the beta decays of cobalt-60 [9]. Figure 2.2 depicts the beta decay of a neutron at quark level, where the $(\mathrm{u},\ \mathrm{d})_L$ doublet couples with a charged W^- boson, which then decays almost immediately to a $(\mathrm{e}^-, \overline{\nu_e})_L$ doublet. In general, the interactions are governed by the transfer of *weak isospin* (T_3), where a weak doublet with $(T_3 = 1/2, -1/2)$ can couple to one of the charged bosons W^+ ($T_3 = +1$) or W^- ($T_3 = -1$). The SU(2) singlets e_R, ν_R, u_R and d_R are invariant under SU(2) transformations and do not couple to the gauge bosons W^1_μ, W^2_μ and W^3_μ.

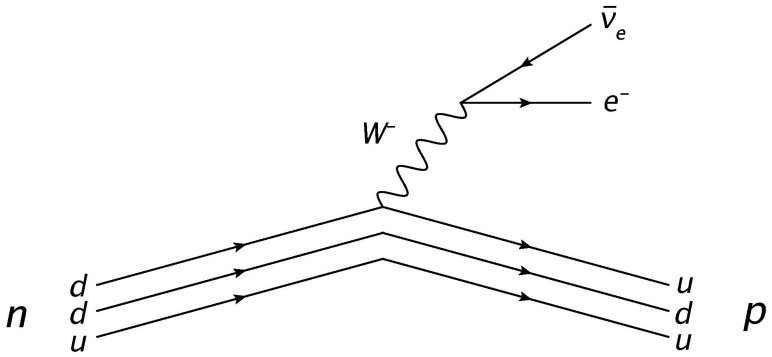

Figure 2.2: Quark-level Feynman diagram of beta decay, where the $(\mathrm{u},\ \mathrm{d})_L$ doublet couple to the W^-, which in turn emits a $(\mathrm{e}^-, \overline{\nu_e})_L$ doublet.

Interactions of the gauge group $\mathrm{U}(1)_Y$ are governed by a separate quantum number called *weak hypercharge* Y. In contrast to the SU(2) group, the group $\mathrm{U}(1)_Y$ can transform right-handed fermions[1] as well as left-handed fermions. The weak isospin and hypercharge quantum numbers are related to the electric charge by the formula:

[1] apart from right- (left-) handed (anti)neutrinos, which are excluded in the Standard Model

$$Q = T_3 + Y/2 \tag{2.7}$$

The physical Z_μ and A_μ (photon) bosons mediate *neutral-current interactions*, and are expressed as a mixing of the gauge fields W^3_μ and B_μ, parameterised by the mixing angle θ_w, as defined below:

$$Z_\mu \equiv \cos\theta_w W^3_\mu - \sin\theta_w B_\mu \tag{2.8}$$

$$A_\mu \equiv \cos\theta_w B_\mu + \sin\theta_w W^3_\mu \tag{2.9}$$

2.1.2 Strong Interaction

The theory of *Quantum Chromodynamics* (QCD) offers an explanation for the phenomenon of quark confinement within hadronic states. Quarks and anti-quarks participate in strong interactions via the transfer of three colour (or anticolour for antiquarks) charges, and are given the arbitrary definitions [red, green, blue]. Gauge invariance under SU(3) colour transformations requires the existence of eight massless vector bosons, referred to as *gluons*, each carrying their own colour-anticolour charge. Because of this, gluons are able to interact not only with quarks but with other gluons as well. The strength of the strong interaction is dependent on a coupling factor α_s, which has a strong dependence on the relative momentum between the partons, Q^2 (Figure 2.3).

At large inter-quark distances, the required energy to separate a quark from a hadron exceeds the required energy for quark pair-production, which explains why collisions at particle accelerators result in the formation of jets of hadrons rather than individual quarks. Conversely, at small inter-quark distances the effective gluon colour charge is screened and $\alpha_s \to 0$. The partons are allowed to move freely in this case, a process referred to as *asymptotic freedom*. A perturbative approach to QCD calculations at high Q^2 is described in Chapter 5.

In addition to creating a mechanism for strong interactions, the introduction of colour charge also solves the spin-statistics problem for baryon quark structures.

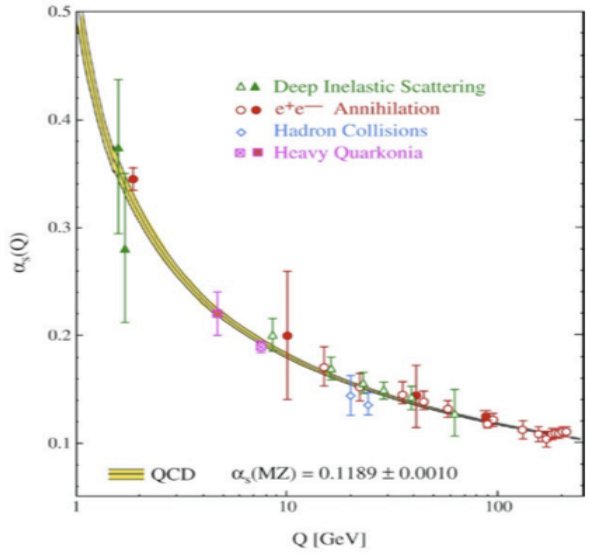

Figure 2.3: The QCD coupling constant has a 'running' dependence on the number of active quark flavours that are described the distribution functions, which is in turn dependent on the energy scale Q^2 at which we are probing [10].

The Δ^{++} baryons contains 3 u-quarks whose identical spin configuration would violate the Pauli Exclusion Principle. The introduction of colour charge makes the Δ^{++} anti-symmetric under quark interchange.

2.1.3 Spontaneous Symmetry Breaking

In an unbroken gauge symmetry the gauge bosons must be massless, which is ideal for describing the massless photon and massless gluon. This becomes a problem when extending the theory to describe the weak interaction, since through measurement the carriers (W and Z bosons) are massive. Simply adding a mass term to the Lagrangian will destroy the renormalisability of the theory. By spontaneously breaking the gauge symmetry the theory remains renormalisable, allowing the gauge bosons to acquire mass. Consider a Lagrangian density for a complex scalar field Φ that includes the following potential:

$$V(\Phi) = -\mu^2\Phi^*\Phi + \lambda(\Phi^*\Phi)^2 \tag{2.10}$$

Assuming positive constants μ^2 and λ, this potential yields a non-zero minimum at $\Phi^*\Phi = \frac{1}{2}\mu^2/\lambda$, referred to as the "vacuum expectation value". In the unitary gauge the vacuum expectation value is written as:

$$\langle\Phi\rangle = \frac{1}{\sqrt{2}}\begin{pmatrix}0\\v\end{pmatrix} \tag{2.11}$$

The form of the potential is shown in Figure 2.4. It is clear that instead of one unique ground state there is an infinite set of degenerate ground states, corresponding to different phases of Φ. Choosing one of the states to be the true ground state breaks the symmetry of the theory. 'Zero-energy' excitations to different ground states would then be possible through the exchange of a massless *Goldstone* boson, and it is these excitations that give the W and Z bosons their mass. Massless gauge bosons have 2 degrees of freedom (polarisations) while massive spin-1 bosons have 3 degrees of freedom. In the spontaneously broken gauge theory, it is the Goldstone boson that provides the third (longitudinal) component to the gauge bosons, causing them to become massive. This theory, known as the Higgs mechanism, predicts the existence of at least one massive neutral scalar Higgs boson, the only particle in the Standard Model that has yet to be verified experimentally.

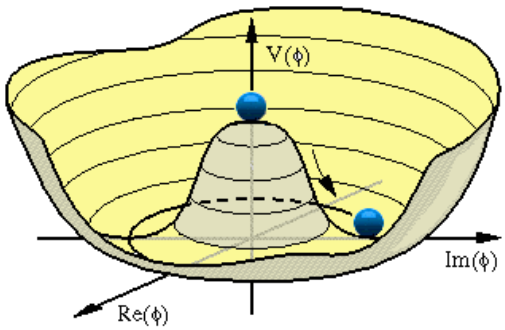

Figure 2.4: Higgs potential in the complex plane.

The fermionic fields couple to the Higgs field through a *Yukawa* interaction term in the Lagrangian. The $(u, d)_L$ doublet couples to the Higgs field Φ:

$$\mathcal{L}_{Yukawa} = -Y_{\mathrm{d}}\overline{(\mathrm{u},\mathrm{d})_L}\Phi \mathrm{d}_{\mathrm{R}} + h.c. \tag{2.12}$$

with Yukawa coupling constant Y_{d}. The vacuum expectation value introduced by the Higgs field (2.11) can be substituted into (2.12) to give a mass term for the d-quark:

$$m_{\mathrm{d}} = \frac{Y_{\mathrm{d}}}{\sqrt{2}}v = \sqrt{2}\frac{Y_{\mathrm{d}}M_{\mathrm{W}}}{g} \tag{2.13}$$

The strength of the d-quark coupling to the Higgs field is proportional to the mass of the quark and inversely proportional to the mass of the W-boson. Using similar techniques, the mass of the u-quark and electron can be derived from their corresponding Yukawa terms.

2.1.4 Quark Mixing and the CKM Matrix

Within the first generation of quarks, the weak interaction couples directly to the (u, d) mass eigenstates as explained in the previous section. Including a second generation of quarks complicates the interaction of the left-handed doublet states: the u quark in this case couples to a superposition of down-type quarks rather than directly to the d-quark state[1]:

$$\begin{pmatrix} \mathrm{u} \\ \tilde{\mathrm{d}} \end{pmatrix} = \begin{pmatrix} \mathrm{u} \\ \cos\theta_C \mathrm{d} + \sin\theta_C \mathrm{s} \end{pmatrix} \tag{2.14}$$

where θ_C is the Cabibbo mixing angle. This was proposed by Cabibbo in 1963 [11] when studying the decay rates of K^+ ($\mathrm{u}\bar{\mathrm{s}}$) and π^+ ($\mathrm{u}\bar{\mathrm{d}}$) particles. The coupling strength of the $\mathrm{u}\bar{\mathrm{s}}$ quarks ($\propto \sin\theta_C$) differed to the coupling strength of the $\mathrm{u}\bar{\mathrm{d}}$

[1]This is by convention, as partnering down-type quarks with superpositions of up-type quarks yields the same results.

quarks ($\propto \cos\theta_C$). In 1970 Glashow, Iliopoulos and Maiani [12] extended this model to include a second generation of mixed quark states:

$$\begin{pmatrix} \mathrm{c} \\ \tilde{\mathrm{s}} \end{pmatrix} = \begin{pmatrix} \mathrm{c} \\ -\sin\theta_C \mathrm{d} + \cos\theta_C \mathrm{s} \end{pmatrix} \tag{2.15}$$

The mixing of these flavour eigenstates describes strangeness violation in a charged weak interaction. Flavour changing via neutral weak interactions is forbidden at tree-level in the Standard Model. Contributions do exist from higher order loop corrections, and are a useful probe for physics beyond the Standard Model. This model actually predicted the existence of the charm (c) quark before its experimental discovery in 1974 [13, 14].

Adding a third generation (t, b) is achieved in a similar way. The three weak eigenstates are related to their mass eigenstates via the Cabbibo-Kobayashi-Maskawa (CKM) [3] matrix:

$$\begin{pmatrix} \tilde{\mathrm{d}} \\ \tilde{\mathrm{s}} \\ \tilde{\mathrm{b}} \end{pmatrix} = \mathbf{V_{CKM}} \begin{pmatrix} \mathrm{d} \\ \mathrm{s} \\ \mathrm{b} \end{pmatrix} = \begin{pmatrix} V_{\mathrm{ud}} & V_{\mathrm{us}} & V_{\mathrm{ub}} \\ V_{\mathrm{cd}} & V_{\mathrm{cs}} & V_{\mathrm{cb}} \\ V_{\mathrm{td}} & V_{\mathrm{ts}} & V_{\mathrm{tb}} \end{pmatrix} \begin{pmatrix} \mathrm{d} \\ \mathrm{s} \\ \mathrm{b} \end{pmatrix} \tag{2.16}$$

Only weak charged-current (CC) interactions, where a charged ($\mathrm{W}^{\pm}$) boson is exchanged, can cause quark flavour transitions within the Standard Model. The probability of a i $\leftrightarrow$ j flavour transition is determined by the magnitude of the element V_{ij}, which experimentally has been shown to be smaller for the off-diagonal elements. The CKM matrix is unitary ($VV^{\dagger} = \mathbf{I}$), which puts constraints on the CKM elements, one of which is shown below:

$$\sum_{\mathrm{k}} V_{\mathrm{ik}} V_{\mathrm{jk}}^{*} = 0 \tag{2.17}$$

For any fixed and different i and j, equation (2.17) constrains three complex numbers corresponding to the different values of k. Six different combinations of i and j gives rise to six different unitarity triangles in the complex plane. All

six unitarity triangles have the same area, and it is the presence of a complex phase in the CKM elements—and therefore a non-zero triangle area—that causes CP-violation in quark flavour transitions. The most commonly used unitarity triangle is shown in Figure 2.5, arising from the constraint:

$$V_{\mathrm{ud}}V_{\mathrm{ub}}^{*} + V_{\mathrm{cd}}V_{\mathrm{cb}}^{*} + V_{\mathrm{td}}V_{\mathrm{tb}}^{*} = 0 \tag{2.18}$$

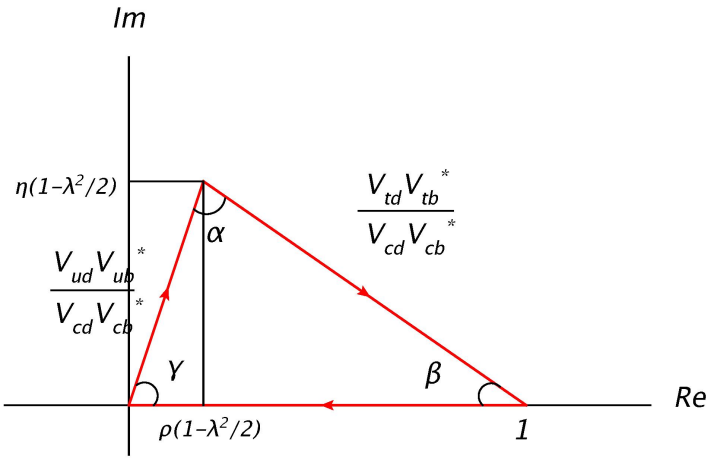

Figure 2.5: Unitarity Triangle resulting from equation (2.18), normalised to $V_{\mathrm{cd}}V_{\mathrm{cb}}^{*}$.

Various parameterisations exist to help in the numerical analysis of the CKM matrix. An appropriate representation of the CKM matrix is the Wolfenstein parameterisation [15], which introduces the four parameters λ, A, ρ and ν. This parameterisation ensures that $\overline{\rho} + i\overline{\nu} = -V_{\mathrm{ud}}V_{\mathrm{ub}}^{*}/V_{\mathrm{cd}}V_{\mathrm{cb}}^{*}$ (see 2.18) is phase-convention independent. With all parameters of order unity, except λ ($= 0.22518^{+0.00036}_{-0.00077}$ [16]), one can readily make order-of-magnitude calculations of CKM elements as expansions of λ. The unitarity of the CKM matrix is preserved to order λ^3, as shown below:

$$\mathbf{V_{CKM}} = \begin{pmatrix} 1-\lambda^2/2 & \lambda & A\lambda^3(\rho - i\eta) \\ -\lambda & 1-\lambda^2/2 & A\lambda^2 \\ A\lambda^3(1-\rho-i\eta) & -A\lambda^2 & 1 \end{pmatrix} + \mathcal{O}(\lambda^4) \tag{2.19}$$

The vertices of the (2.18) triangle, normalised to $V_{cd}V_{cb}^*$, are exactly (0,0), (1,0) due to the parameter definitions ($\overline{\rho}$, $\overline{\nu}$) as shown in the previous figure. The measurement of the 3 angles α, β, γ has become a highly anticipated test of flavour physics. Deviations from a closed triangle may provide an indication of physics beyond the Standard Model. Constraints on these angles can come from a variety of different measurements, resulting in a highly constrained combined fit provided by the CKM Fitter group (Figure 2.6) [16].

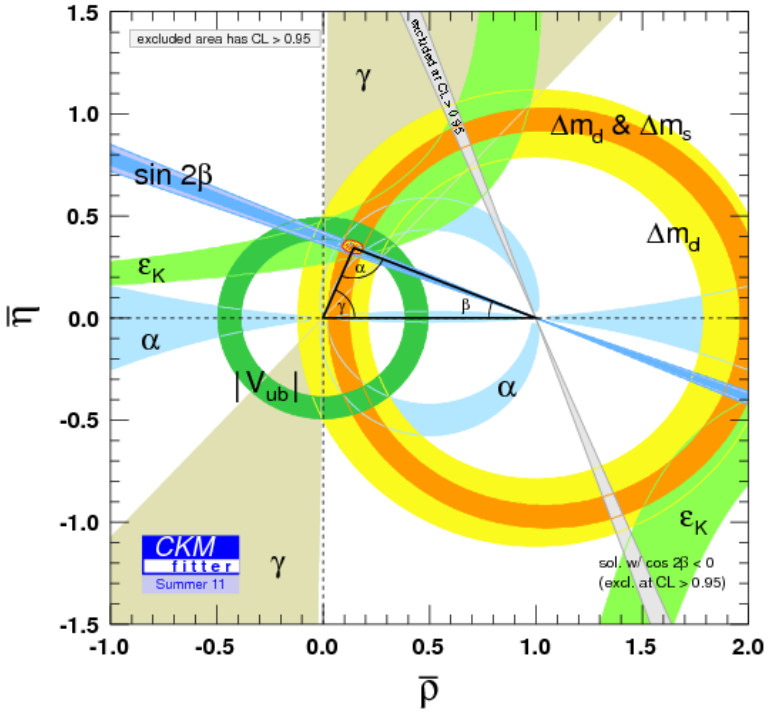

Figure 2.6: Latest global fit to the unitarity triangle, presented at 2011 EPS-HEP and Lepton-Photon conferences.

The measurement of CP violation in the B meson system provides many of the constraints on the angles. The next section describes these CP-violating decays, as well as other decays that may further our understanding of physics beyond the Standard Model.

2.1.5 CP Violation

The violation of CP conservation can be described as an asymmetry in processes between a particle and its anti-particle, that is after applying the charge conjugation C and parity inversion P operators to the particle wavefunction. The CP conjugate states are hermitian conjugates of each other, thus any complex coupling present in the interacting Hamiltonian will introduce an asymmetry between the states. The complex phase arising in the CKM matrix is an example of this, and is the cause of CP violation in the coupling of quarks to $W^{\pm}$.

CP violation manifests itself in 3 different ways directly via decay amplitudes, or indirectly via neutral meson mixing and interference processes, each of which are described in the following sections.

Direct CP Violation

This type of CP violation reflects the case where the transition amplitude to a final state f (A_{f}) differs from the transition for the charge conjugate state ($\overline{A}_{\bar{\mathrm{f}}}$):

$$\left|\frac{A_{\mathrm{f}}}{\overline{A}_{\bar{\mathrm{f}}}}\right| \neq 1 \tag{2.20}$$

The mechanism for this is based on the relative phase of two or more transition amplitudes contributing to the same transition. Decays with multiple tree-level decays, or higher-order loop corrections, such as penguin or box processes, can contribute to this relative phase.

The BaBar collaboration provided first compelling evidence [17] of direct CP violation in the decay $B^0_{\mathrm{d}} \to K^{\pm}\pi^{\pm}$. In the SM, the decay occurs through two different mechanisms ("penguin" and "tree"), which carry different weak phases and, in general, different strong phases. The direct CP-violating asymmetry is defined as:

$$A_{\mathrm{K}\pi} = \frac{n_{\mathrm{K}^-\pi^+} - n_{\mathrm{K}^+\pi^-}}{n_{\mathrm{K}^-\pi^+} + n_{\mathrm{K}^+\pi^-}} \tag{2.21}$$

where $n_{\mathrm{K}^-\pi^+}$ and $n_{\mathrm{K}^+\pi^-}$ are the measured yields for the two final states. Using a data sample of 227 million $\Upsilon(4\mathrm{S}) \rightarrow \mathrm{B}\overline{\mathrm{B}}$ decays, a total signal yield of 1606 $\pm$ 51 decays were observed with a corresponding asymmetry $A_{K\pi} = -0.133 \pm 0.030(stat.) \pm 0.009(syst.)$. The probability of observing such an asymmetry in the absence of direct CP violation is 1.3×10^{-5}, corresponding to 4.2 standard deviations. Background contributions to this measurement, namely through $\mathrm{B_d}$—$\overline{\mathrm{B_d}}$ mixing and particle reconstruction, have been taken into account.

Indirect CP Violation

Neutral mesons have been found to oscillate between particle and antiparticle states via flavour-changing neutral-current processes of the kind shown in Figure 2.7.

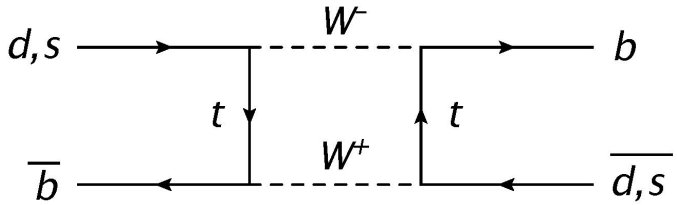

Figure 2.7: $\mathrm{B}^0 - \overline{\mathrm{B}}^0$ transition, proceeding through the transfer of a virtual t-quark.

For a neutral B meson (and indeed for a neutral K or D meson), the mass eigenstates exist as a linear combination of the flavour eigenstates:

$$|\mathrm{B_L}\rangle = p|\mathrm{B}^0\rangle + q|\overline{\mathrm{B}}^0\rangle \tag{2.22}$$

$$|\mathrm{B_H}\rangle = p|\mathrm{B}^0\rangle - q|\overline{\mathrm{B}}^0\rangle \tag{2.23}$$

where $\mathrm{B_L}$ and $\mathrm{B_H}$ denote the light and heavy mass eigenstates respectively. The normalised coefficients p and q represent the relative strengths of the B^0 and $\overline{\mathrm{B}}^0$ respectively. For the case that $|p| = |q| = \frac{1}{\sqrt{2}}$ the mass eigenstates are CP eigenstates and ultimately CP is conserved. However, the presence of a non-zero phase in the CKM matrix gives rise to a complex phase for the mass difference ΔM between $\mathrm{B_L}$ and $\mathrm{B_H}$, leading to the inequality

$$|\frac{p}{q}| \neq 1 \tag{2.24}$$

and the mass eigenstates are no longer CP eigenstates. The violation of CP conservation results in a net oscillation that favours either B^0 or $\overline{B}^0$ states.

For the case of the B^0—$\overline{B}^0$ oscillations shown in the previous figure, the dominant phase contributions come from a virtual t-quark exchange. This ratio for B_d mesons can be described by

$$\frac{p}{q} = \frac{V_{td}^* V_{tb}}{V_{td} V_{tb}^*} \tag{2.25}$$

while similarly for B_s mesons

$$\frac{p}{q} = \frac{V_{ts}^* V_{tb}}{V_{ts} V_{tb}^*} \tag{2.26}$$

Mixing-induced CP violation can be isolated for neutral meson semi-leptonic decays M, $\overline{M} \to l^{\pm} X$ where, within the Standard Model, the decay amplitudes for the charge conjugates are equal. The asymmetry A_{sl} can be measured via the asymmetry of "wrong-sign" decays induced by oscillations:

$$A_{sl}(t) = \frac{d\Gamma/dt[\overline{M^0_{phys}} \to l^+ X] - d\Gamma/dt[M^0_{phys} \to l^- X]}{d\Gamma/dt[\overline{M^0_{phys}} \to l^+ X] + d\Gamma/dt[M^0_{phys} \to l^- X]} \tag{2.27}$$

$$= \frac{1 - |q/p|^4}{1 - |q/p|^4} \tag{2.28}$$

The DØ collaboration has published world-leading results on the like-sign dimuon charge asymmetry A^b_{sl} for semileptonic b-hadron decays, in 9.0 fb^{-1} of $p\overline{p}$ collisions recorded at a centre-of-mass energy $\sqrt{s} = 1.96$ TeV at the Fermilab Tevatron collider [18]. Such like-sign dimuon events are only possible when one of the b-hadrons is a B^0 or B^0_s meson that oscillates and decays to a muon of charge

opposite to that expected from the original b quark[1]. The measured asymmetry, $A_{sl}^{\mathrm{b}} = (-0.787 \pm 0.172\ (\mathrm{stat.}) \pm 0.093\ (\mathrm{syst.}))$, differs by 3.9 standard deviations from the predictions of the Standard Model and provides evidence for anomalously large CP violation in semileptonic neutral B decay.

CP Violation from Interference

Now suppose the neutral meson decays to a final state that is common to both particle and antiparticle. There is then interference between mixed and unmixed states and the time-integrated CP asymmetry is dependent on phase contributions from both the decay amplitudes and mixing, and there is CP violation if

$$\mathcal{I}m(\lambda_{\mathrm{f}}) \neq 0 \tag{2.29}$$

with

$$\lambda_{\mathrm{f}} = \frac{p}{q}\frac{\overline{A}_{\mathrm{f}}}{A_{\mathrm{f}}} \tag{2.30}$$

Consider the neutral meson decay $\mathrm{B}^0 \rightarrow \mathrm{J}/\psi\mathrm{K_S}$, where the decay products are CP-odd eigenstates. Analagous to 2.22 and 2.23, the kaon mass eigenstate exists as a linear combination of flavour eigenstates:

$$|\mathrm{K_S}\rangle = p_{\mathrm{K}}|\mathrm{K}^0\rangle - q_{\mathrm{K}}|\overline{\mathrm{K}}^0\rangle \tag{2.31}$$

The phases in the CKM matrix introduce a phase in the ratio of p_{K} to q_{K}, which is calculated in a similar way to the quark transitions in Figure 2.7. In this case it is the exchange of an internal c-quark that dominates, so we have a factor

$$\frac{p_{\mathrm{K}}}{q_{\mathrm{K}}} = \frac{V_{\mathrm{cd}}^* V_{\mathrm{cs}}}{V_{\mathrm{cd}} V_{\mathrm{cs}}^*} \tag{2.32}$$

which, for complex phases in the CKM matrix, is $\neq 1$. This enters in the ratio of the decay amplitudes for the B_0:

[1] Charge conjugate is implied.

$$\frac{A_{\mathrm{J/\Psi K_S}}}{\overline{A}_{\mathrm{J/\Psi K_S}}} = -\frac{V_{\mathrm{cb}}V_{\mathrm{cs}}^*}{V_{\mathrm{cb}}^*V_{\mathrm{cs}}}\frac{V_{\mathrm{cd}}^*V_{\mathrm{cs}}}{V_{\mathrm{cd}}V_{\mathrm{cs}}^*} = -\frac{V_{\mathrm{cb}}V_{\mathrm{cd}}^*}{V_{\mathrm{cb}}^*V_{\mathrm{cd}}} \tag{2.33}$$

Combined with the asymmetry from B-meson mixing 2.25:

$$\mathcal{I}m\left(\frac{p}{q}\frac{A_{\mathrm{J/\Psi K_S}}}{\overline{A}_{\mathrm{J/\Psi K_S}}}\right) = -\frac{V_{\mathrm{td}}^*V_{\mathrm{tb}}}{V_{\mathrm{td}}V_{\mathrm{tb}}^*}\frac{V_{\mathrm{cb}}V_{\mathrm{cd}}^*}{V_{\mathrm{cb}}^*V_{\mathrm{cd}}} = \sin(2\beta) \tag{2.34}$$

In the Standard Model, the $\mathrm{B}^0 \rightarrow \mathrm{J}/\psi\mathrm{K_S}$ decay is dominated by the tree-level process and there is no direct CP violation. Therefore, the time-dependent CP asymmetry is a pure sine with the UT angle β as an amplitude:

$$A(t) \propto \sin(2\beta)\sin(\triangle m_{\mathrm{B}} t) \tag{2.35}$$

This channel is often referred to as the "golden" channel, due not only to this theoretical constraint but also to a clean experimental signature. This measurement has been performed using 772×10^6 $\mathrm{b\overline{b}}$ pairs collected at the $\Upsilon(4S)$ resonance with the Belle detector at the KEKB asymmetric-energy $\mathrm{e^+e^-}$ collider [19]. The study implements the use of 'tagging', where the flavour of the B^0 ($\rightarrow \mathrm{J}/\psi\mathrm{K}_S$) meson is identified from the decay products of the accompanying meson. From the distribution of the proper time intervals between the two B decays, the CP violation parameter was obtained:

$$\sin(2\beta) = 0.667 \pm 0.023(\mathrm{stat.}) \pm 0.017(\mathrm{syst.}) \tag{2.36}$$

2.2 Outlook

The Standard Model framework has been reviewed in this chapter, in a way that explains the main properties of the fundamental particles. Mixing of quark flavours is achievable through charged-current weak interactions. The

presence of three quark generations extends the parameterisation of quark-mixing to include a complex phase, which causes violation of charge-parity (CP) conservation. Experiments such as LHCb study the various manifestations of CP violation through the weak decay of B-hadrons, which includes direct searches (in decay) and indirect searches (in mixing, and interference between mixing and decay). Chapter 5 will describe how the channel $B^{\pm} \rightarrow J/\psi K^{\pm}$ can be used as a measurement of production asymmetry, examining the contribution to the measurement from direct CP violation in the decay.

Chapter 3

The LHCb Detector

Flavour physics in the b-quark sector provide a stringent test of CP violation mechanisms at and beyond the Standard Model. Notable experiments such as BaBar, Belle, CDF and DØ exploit the copious amount of B mesons produced from high-energy beam collisions to analyse these CP-violating parameters. The newest B-physics experiment, LHCb, began recording high-energy collisions at the start of 2010, and has already produced world-leading results. A brief introduction to the Large Hadron Collider is given at the start of this chapter, proceeding on to a description of the components that comprise the LHCb detector. Where possible, a review of the performance with beam collisions is given in each section.

3.1 The Large Hadron Collider

The Large Hadron Collider (LHC) is at the forefront of particle physics discovery. The energy levels of the LHC will probe the so far un-explored regions of particle physics, and will determine the existence, or non-existence, of hypothesised particle such as the Higgs boson or the large family of new particles predicted by supersymmetry. The design luminosity of the LHC exceeds that of any other particle accelerator, resulting in an abundant amount of data collected by the detectors that has already provided some definitive answers to these models.

Construction of the LHC was carried out by the European Organisation for

Nuclear Research (CERN) over the period 1998-2008, in the 27 km-long circular tunnel that formerly housed the Large Electron Positron (LEP) collider. The LHC is designed to accelerate two counter-clockwise beams of protons in a continuous ring of vacuum chambers. High intensity beams can be created, containing up to 2808 bunches per beam, with a maximum of 1.15×10^{11} protons per bunch. The beams undergo a pre-acceleration from 26 GeV to 450 GeV in a smaller ring, the Super Proton Synchotron (SPS), before injection into the LHC, where energies of up to 7 TeV per beam can be achieved.

Thousands of magnets of different size and type are used to direct the beams around the accelerator. These include 1232 dipole electromagnets, which provide the bending power required to keep the beam trajectory inside the ring. The dipole magnetic field, at 8.33 T, is considerable, drawing massive currents from the electromagnets. To minimise the resulting resistive losses, superconducting materials are chosen for the magnets, together with a liquid helium coolant system. A wide range of magnetic multipoles are used for other purposes: quadrupoles provide transverse squeezing of the propagating beams; tripoles focus the proton bunches at the detector points to maximise the number of collisions.

The six experiments at the LHC are all run by an international collaboration of institutions, bringing together scientists from all over the world. Each experiment is distinct, based on the detector design. ATLAS and CMS are general-purpose detectors searching for the myriad of particles produced in the proton collisions, of which the elusive Higgs boson forms a prominent search. The ALICE experiment aims to obtain a deeper understanding of the strong force by colliding beams of lead atoms—the high nucleon density creates a quark-gluon plasma where the particles can be treated as quasi-free. The smaller experiments, LHCf and TOTEM, are located near ATLAS and CMS respectively and are designed to detect particles in the forward angles. Cross-section and luminosity measurements at TOTEM are crucial for many analyses in the other LHC experiments.

3.2 The LHCb detector

The LHCb experiment is designed to measure CP violation and rare decays of hadrons involving the beauty (b) quark. The LHCb detector is a single-

arm spectrometer, covering an angular range from 10 mrad to 250 mrad in the non-bending plane, and 10 mrad to 300 mrad in the bending plane. The pseudorapidity ν ($= -\ln[\tan(\theta/2)]$) ranges from 1.9 to 4.9, covering the region where high $b\bar{b}$ production peaks (see Figure 3.1). It incorporates precision vertexing and tracking systems, particle identification over a wide spectrum and relies on relatively soft transverse momentum triggers, efficient for both leptonic and hadronic B decays.

A side-on view of the detector layout is shown in Figure 3.2. Starting closest to the interaction point (IP at z = 0) are the following sub-detectors: Vertex Locator (VELO); Ring-Imaging Cherenkov counter 1 (RICH1); Tracker Turencsis (TT); Magnet; Tracking Stations (T1-T3); Ring-Imaging Cherenkov counter 2 (RICH2); Muon Station (M1); Scintillator Pad Detector/Pre-Shower (SPD/PS); Electromagnetic Calorimeter (ECAL); Hadronic Calorimeter (HCAL); Muon Stations (M2-M5). In requiring the entire detector to be inside the LHCb angular acceptance, each sub-detector is designed to be projective, where the total sensitive area is proportional to its distance from the IP.

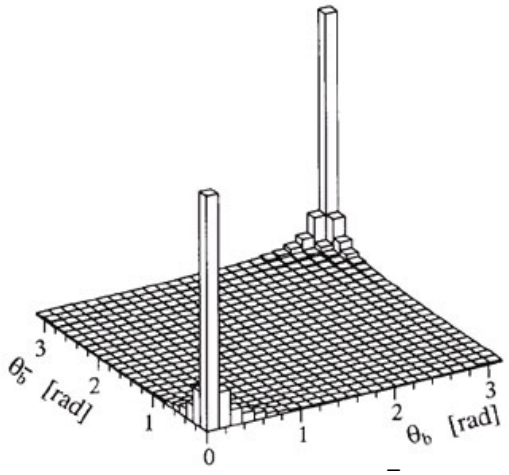

Figure 3.1: Polar angle of simulated B and $\bar{B}$ hadrons. The majority is contained within 300 mrad in the forward and backward directions.

The beam pipe holds the vacuum through which the proton beams traverse. It is constructed in conical sections so as to minimise interactions with decay particles. From the IP to RICH2, beryllium is used as the material for the beam pipe, which has good rigidity (against pressure differences) yet high transparency (to high rapidity particles). At larger distances from the IP, the effect of occupancy

from these secondary interactions is low and therefore stainless steel can be used.

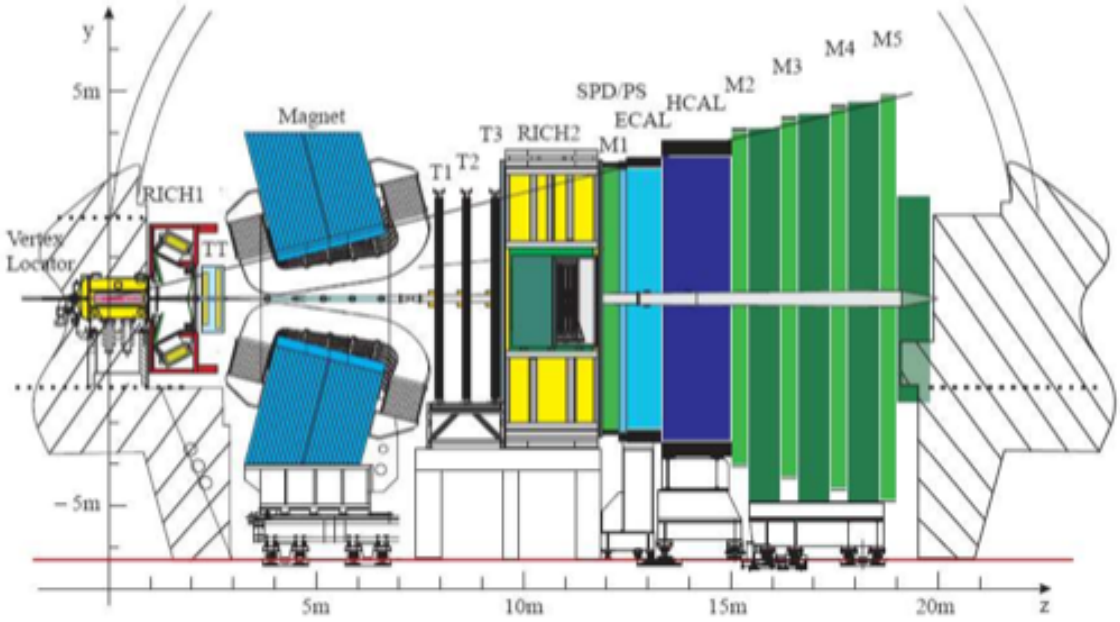

Figure 3.2: Schematic of the lhcb detector. The interaction region is located in the VELO (z = 0). All subdetectors are labelled in black.

3.3 VELO

The VELO provides precise measurements of charged particle track co-ordinates close to the interaction region. Locating the parton interaction point is an essential requirement for B-hadron lifetime measurements, and a precise determination is possible through the high multiplicity (> 30) of charged particle tracks generated by the interaction. This reconstructed vertex is given the term *primary vertex*.

The *impact parameter* quantifies how close the particle track passes the primary vertex, and provides strong separation power of particles decaying from B-hadrons against those produced directly from the primary vertex. The partons participating in a pp collision typically have unequal momenta, and this boosts the B-hadron by $\gamma = 15$-20 [1] with respect to the laboratory frame. The extended decay length (~ 1 cm) results in a vertex of B-decay particles (secondary vertex)

that is spatially detached from the primary vertex.

3.3.1 Design

The VELO comprises two detector halves, shown as a computer image in Figure 3.3. Each half is equipped with 21 pairs of semi-circular readout sensors centred around and intermittently along the beam pipe. Each pair contains an R-sensor that measures the radial coordinate and a Φ sensor that measures the azimuthal coordinate—the full readout of one pair yields a 3-dimensional position of the charged particle. Occupancy is highest at the innermost regions and drops off radially, and this is reflected in the increasing strip pitch approaching the outermost regions.

When combined with the opposite detector half, this gives 21 VELO stations, providing complete coverage of the detector acceptance. In normal running conditions, the VELO sensors are positioned as close as possible to the beam pipe ($\sim$ 5 mm) to shorten the extrapolation distance from the track to the primary vertex. During injection though, the required aperture of the LHC beam is larger than 5 mm, therefore the sensors are designed to retract by 15 mm. To minimise the amount of material traversed by the particle, the sensors are enclosed in a vessel and held at vacuum.

Of the 21 VELO stations, 6 are located upstream of the IP to reconstruct the vertices of collisions occuring outside the nominal interaction point, as well as provide a better reconstruction performance of the primary vertex. Two Pile-Up (PU) stations are located upstream of the VELO sensors and are used to identify multiple interactions. This is measured through the detected hit multiplicity and transmitted to the first stage of the trigger, where a decision is taken whether to reject the event. Information from the VELO is read out at a rate of 1 MHz and is used as input to the first stage of the High Level Trigger (HLT1).

3.3.2 Performance with Beam

Measurements of primary vertex resolution have been carried out by the VELO collaboration, by taking two separate sets of VELO tracks and recording the

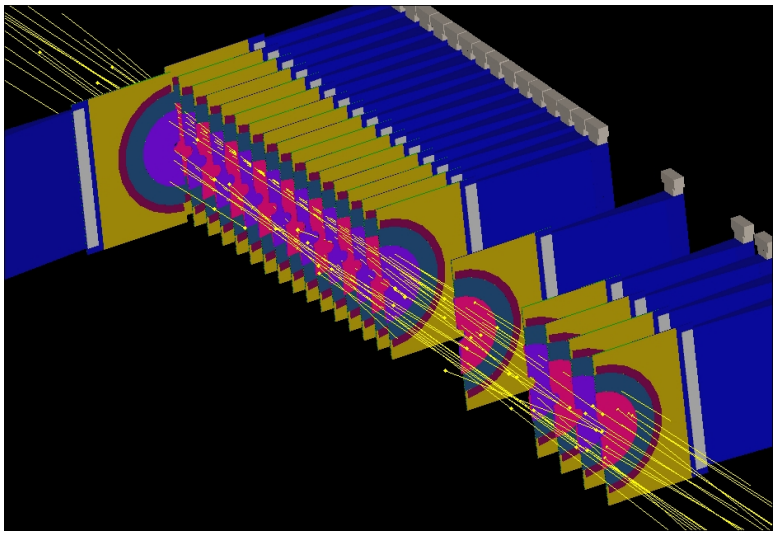

Figure 3.3: Cut-away computer image of VELO halves, taken with event display software. A test beam was sent down the transfer line to the LHC tunnel, striking a beam stopper just outside the LHCb cavern and producing the secondary particles that are observed in the VELO.

difference in the reconstructed primary vertex. Figure 3.4 shows a measurement of the x-coordinate primary vertex resolution as a function of number of VELO tracks, using events where exactly one primary vertex was reconstructed. The performance of the VELO with collision data is excellent, with a resolution of $\sim$ 13 μm for 25 tracks. The $\sim$20% discrepancy between simulated and collision data has yet to be explained, though it may be attributed to an incomplete description of the VELO material in simulation [20].

Figure 3.5 shows a measurement of the x-coordinate impact parameter resolution, obtained from minimum bias events i.e. events with minimal activity in the detector. Again, the performance of the VELO provides is excellent, with an impact parameter resolution of < 35 μm for tracks of $p_{\mathrm{T}} > 1$ GeV/c. The discrepancy between simulation and collision data is strongly correlated to the discrepancy in primary vertex resolutions.

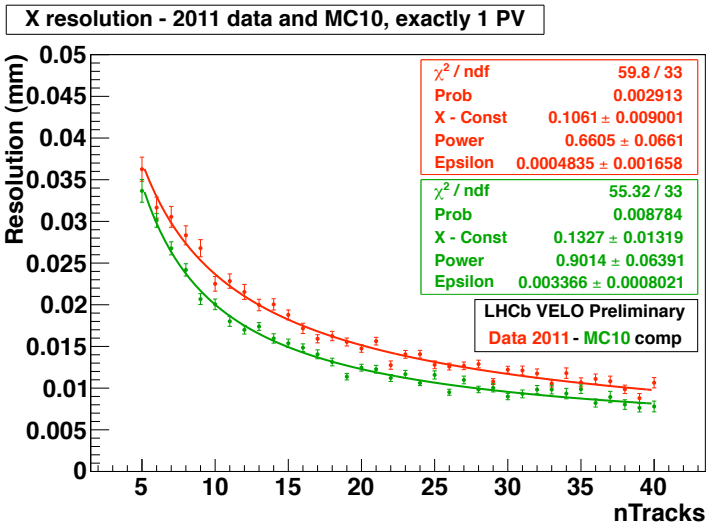

Figure 3.4: Primary vertex resolution in x-coordinate. Measured from two independent sets of VELO tracks. Events contain only one reconstructed primary vertex.

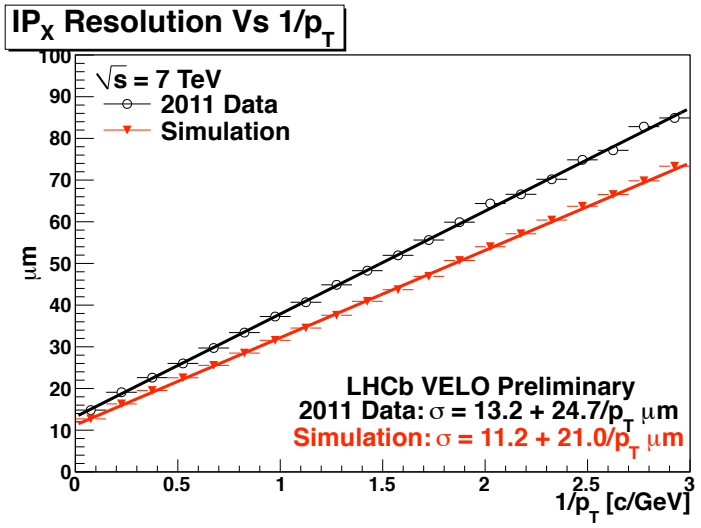

Figure 3.5: Impact Parameter in x-coordinate. Measured from minimum bias sample of tracks wrt z-coordinate of fitted primary vertex. Events contain only one reconstructed PV.

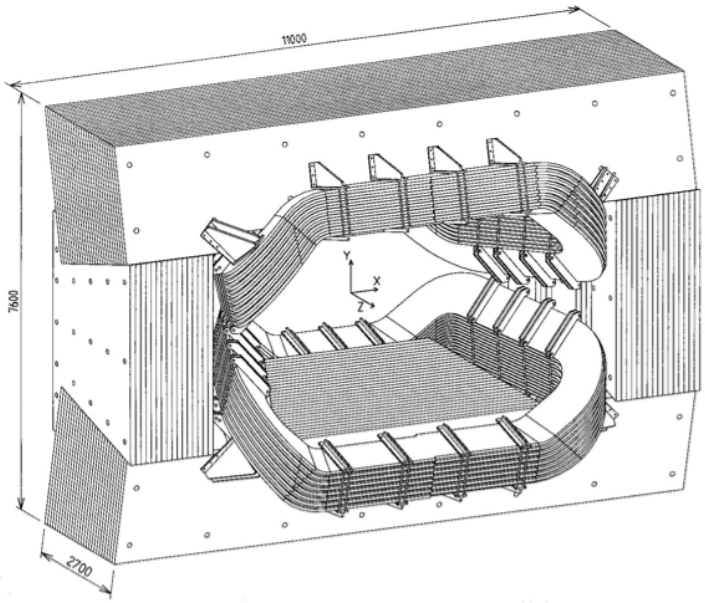

Figure 3.6: Schematic of magnet from a downstream perspective. To reduce electrical power requirements the pole faces are shaped to follow the acceptance angles of the experiment.

3.4 Magnet

A warm dipole magnet, located 5 m downstream from the interaction region, deflects charged particles in the horizontal plane. The curvature of the deflected track then provides a measurement for the momentum of the charged particle. High momentum precision is required at LHCb—a mass resolution of 10 MeV/c^2 for the decay $B_s \rightarrow {D_s}^+\pi^-$ demands a momentum resolution $\delta p/p \sim 0.4\%$ for momenta up to 200 GeV/c [21]. The integrated magnetic field of 4.2 Tm provides considerable bending power to make this required precision possible. The magnet consists of two trapezoidal coils bent at 45° on the two transverse sides, arranged inside an iron yoke of window-frame configuration. Rapid ramping-up of the magnetic field is possible with this magnet, as is field inversion.

3.5 Tracking stations

The Tracking system consists of the Tracker Turencsis (TT) located upstream of the magnet, and Tracking Stations T1, T2, T3 located downstream of the magnet. Based on a similar concept as the VELO, the Tracking system provides precise measurements of charged particle track co-ordinates. The stations T1-T3 can be further divided into two sub-detectors that cover different regions of the acceptance—these are called the Inner Tracker (IT) and Outer Tracker (OT). Both the TT and IT use silicon micro-strip technology and are described in section 3.3.1. The OT uses straw-tube technology and is described in section 3.3.2.

The majority of decay particles from interesting physics channels are high momentum charged particles. The Tracking Stations (T1, T2, T3) measure track co-ordinates downstream of the magnet which, when combined with upstream tracking and VELO information, enables the charge and momentum of the particle to be determined. Information from the Tracking system is read out at a rate of 1 MHz and is used as input to the first stage of the High Level Trigger (HLT1).

3.5.1 Silicon Trackers

The TT and IT form the 4 silicon tracker stations. Both the TT and IT use silicon micro-strip technology with strips of pitch ~ 200 μm. Each of the stations comprises a light-tight and thermally insulated detector box within which are 4 detection layers. The first and fourth detection layers have vertical readout strips, while the second and third layers have readout strips rotated by a stereo angle of $+5^\circ$ and -5° respectively. The individual modules that make up these layers can be retracted for beam pipe maintenance. Adjacent modules are staggered in z by a few mm and overlap in x by a few mm to fill acceptance gaps and facilitate relative alignment of modules.

Tracker Turencsis (TT)

The TT is used for measurement of track coordinates upstream of the magnet. This is particularly important in the reconstruction of long-lived neutral particles

(K_S, Λ) that decay outside the VELO and also of low momentum particles that are bent out of the LHCb acceptance by the magnet. The TT consists of two pairs of planar detection layers separated by approximately 30cm. The TT layers are 150 cm wide and 130 cm high and cover the full angular acceptance of LHCb.

Particle flux is highest at the innermost regions and drops off radially, which is accounted for by increasing strip lengths from innermost to outermost sensors (K-sector to L-sector) as shown in Figure 3.7. This keeps hit occupancy below a few percent on all channels whilst minimising the number of channels used.

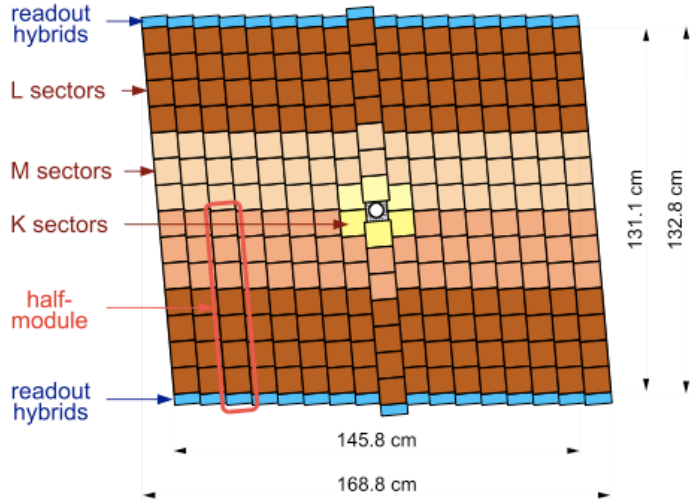

Figure 3.7: Arrangement of half-modules to form the third TT layer. Strip pitch varies between inner (K), middle (M) and outer (L) sectors.

Inner Tracker (IT)

The Inner Tracker (IT) is used for measurement of track co-ordinates downstream of the magnet, in a region where charged particle density is still significantly large (up to the order 10^{-2} cm^{-2}). Each detector box contains 4 detection layers 125 cm in width and 41 cm in length. The chosen width reflects the expected spread of deflected particles in the horizontal direction. The modules of the layers are arranged in a criss-cross pattern, with groups of 7 adjacent modules located above and below the beam pipe (comprising 1 sensor + 1 readout hybrid) and to either side of the beam pipe (comprising 2 sensors + 1 readout hybrid) as shown in Figure 3.8.

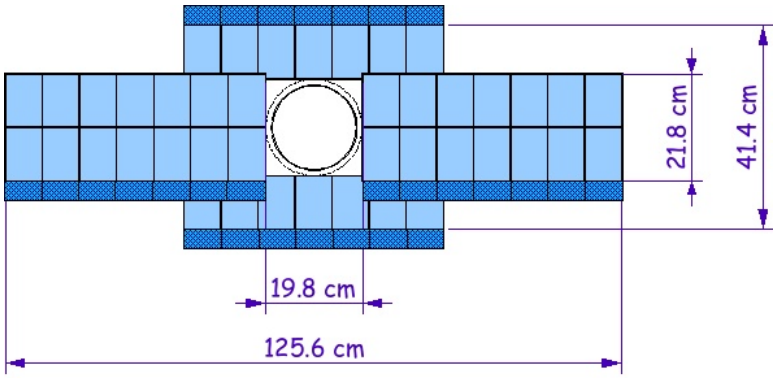

Figure 3.8: Schematic of IT layer, showing criss-cross arrangement of modules with readout hybrids on outer-edge (dark blue).

Two types of sensors are used in the IT, differing only in the thickness. The sensors are 7.6 cm wide and 11 cm long, and are 320 μm thick on one-sensor modules and 410 μm thick on two-sensor modules. The choice in thickness was a compromise between maximising signal-over-noise whilst minimising the material budget.

3.5.2 Outer Tracker (OT)

The OT is used for tracking of charged particles and for measurement of their momentum over a large acceptance area. High hit resolution is required to achieve a momentum resolution as low as 0.4%. As with the silicon trackers, an OT station is split into four detection layers, each with an active area of approximately 1.49 $\times$ 1.21 m. The first and fourth layers have vertical tubes while the second and third layers have tubes rotated by a stereo angle of $+5^\circ$ and -5° respectively. Each layer-half is retractable and contains 7 long modules and 4 short modules as shown in Figure 3.9.

The OT is a drift-time detector, incorporating layers of adjacent gas-filled straw tubes, each with inner diameter 4.9 mm. A charged particle passing through the tube ionises the gas molecules, producing electrons. The position of the track is found by timing how long the electrons take to reach an anode wire situated down the centre length of each tube. The counting gas in the tubes is a mixture of Argon (70%) and CO_2 (30%), chosen in order to guarantee a fast response time (below

50 ns) and a sufficient drift co-ordinate resolution ($\sim$ 200 μm). Two staggered layers of drift tubes are arranged into, and operated as, a single module. A module is either F-type, containing 256 straws, or S-type, containing 128 straws. The entire OT module comprises 168 F-type modules and 72 S-type modules.

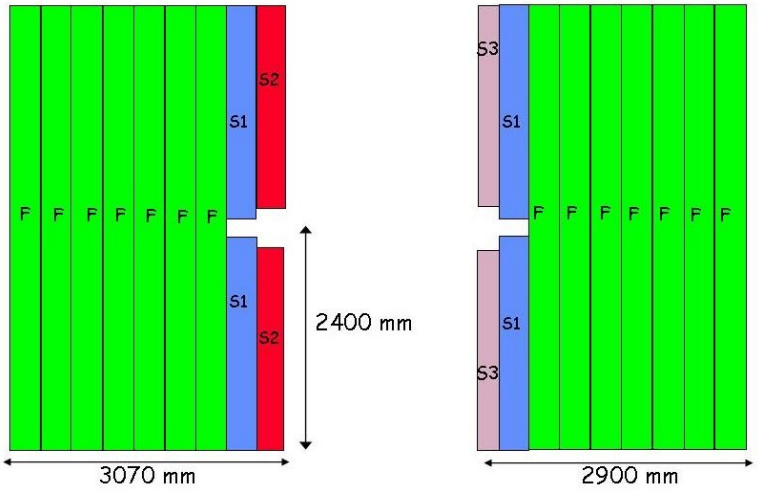

Figure 3.9: Layout of an OT detection layer. The two detector halves are moved together to surround the IT.

3.5.3 Performance

The Tracking system provided one of the first physics measurements at LHCb. A study of the prompt production of $K_s \rightarrow \pi^+\pi^-$ decays was carried out on $\sqrt{s}$ = 900 GeV beam data taken in 2009 [22]. The selection uses downstream charged pion tracks only i.e. using information from the TT and T-stations. This measurement was possible despite the VELO being fully retracted at the time, given that the majority of K_s particles decay after the VELO. Among the set of cuts imposed was the requirement that the reconstructed K_s pointed back to the primary vertex, itself independently reconstructed using beam-beam and beam-gas events.

The invariant mass distribution of selected K_s particles is shown in Figure 3.10. The K_s cross-section as a function of transverse momentum, calculated using a knowledge of detector efficiencies and the beam luminosity, shows good consistency between collision data and simulated data as shown in Figure 3.11.

The cross-section is shown in the rapidity region $3 < y < 3.5$, where K_s production peaks ($y = \frac{1}{2}\ln\frac{E+p_L}{E-p_L}$).

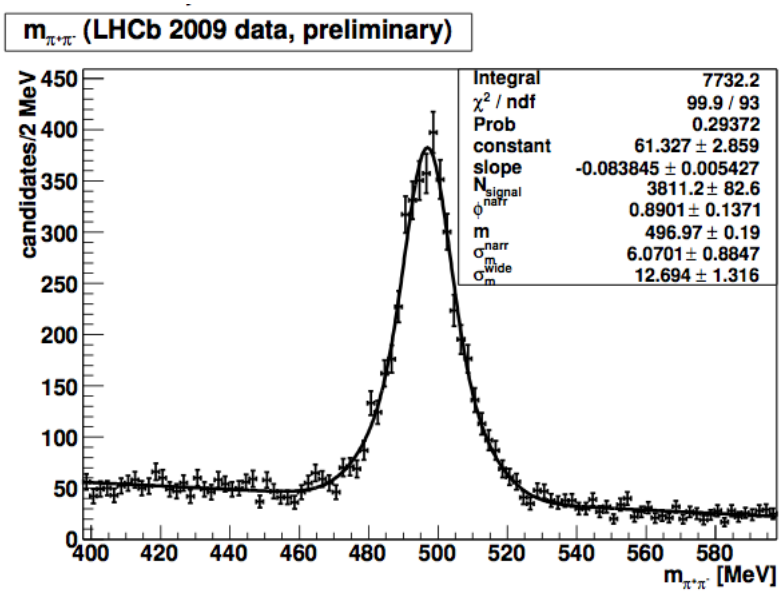

Figure 3.10: Invariant mass distribution of $K_s \to \pi^+\pi^-$ decays, with double Gaussian fit overlaid.

3.5.4 Long track reconstruction

Downstream tracking, described previously, is just one of a number of categories of track reconstruction. *Long track* reconstruction combines information from the VELO and tracking stations, providing the most precise momentum estimate of all the track categories. This explains the pre-dominant use of long tracks for physics analyses (including an analysis of $B^\pm \to J/\psi K^\pm$ decays carried out in the later parts of this thesis). A comparison of track categories in the detector is shown in Figure 3.12. A complete description of the tracking algorithms and a detailed study of their performance can be found in Ref. [23].

VELO tracks serve as the seeds for long track finding. The magnetic field in the VELO is sufficiently low that tracks can be considered as straight lines. The algorithm starts by making three-dimensional space points, combining r and ϕ clusters. Then, triplets of space points are searched in the most downstream stations. Clusters in the more upstream stations are added by extrapolating the

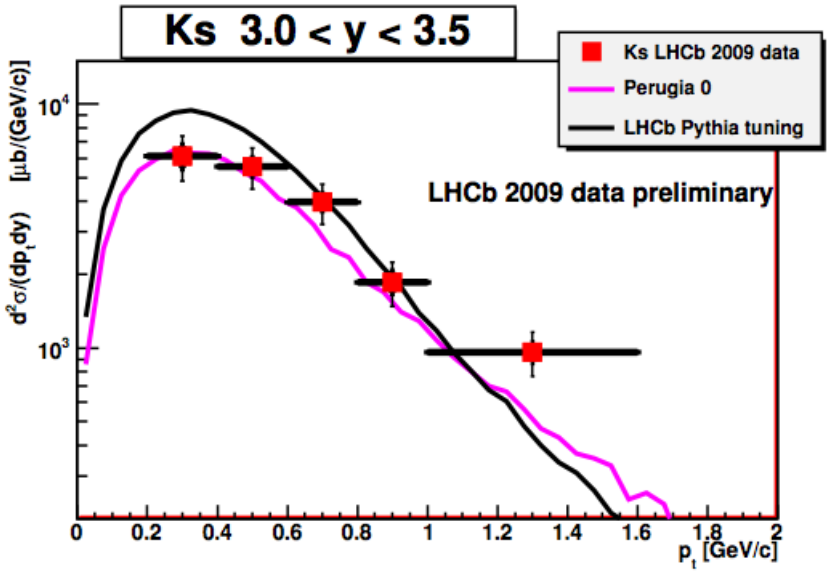

Figure 3.11: Production cross-section of K_s particles as a function of p_T.

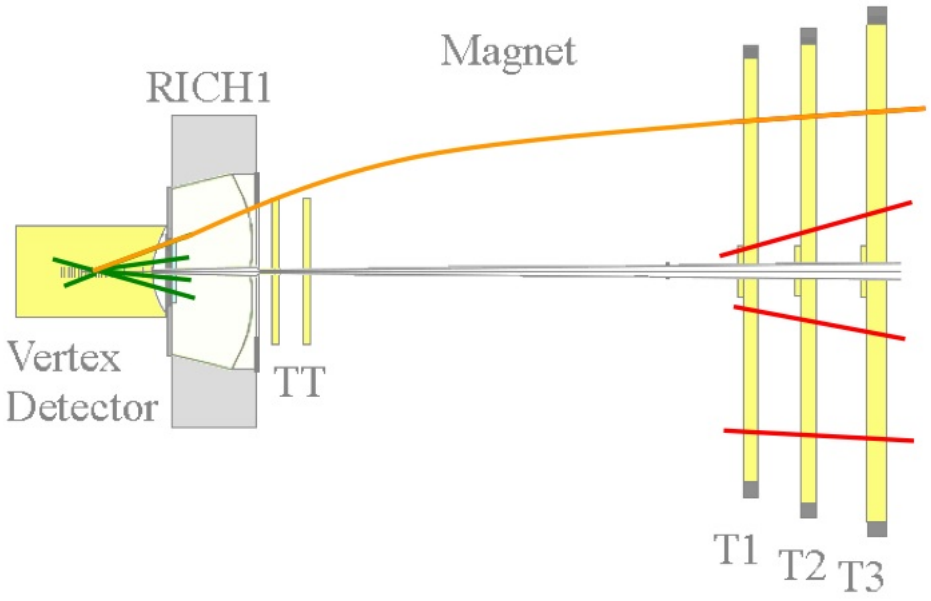

Figure 3.12: Trajectories through the LHCb detector of long tracks (orange), VELO tracks (green) and downstream tracks (red).

candidate track towards the interaction point.

In the *forward tracking* algorithm, tracks are searched in the T stations by parametrizing the expected position in T as a function of the VELO seed track parameters and the position of a single hit in T. Further T station hits in a window around the expected position in different stations and layers are picked up. If the combination of a VELO seed and some T station hits satisfies some quality cuts, it is promoted to a long track. Hits in TT are picked up if they are close enough to a track through VELO and T station hits.

Long tracks have an accurate momentum estimate, achieving a momentum-averaged resolution of 0.35% from simulated $b\bar{b}$ events. Figure 3.13 shows the momentum dependence of the resolution for long tracks found by the forward tracking and track-matching[1] algorithms, alongside a "cheated" pattern recognition. The rise in $\delta p/p$ towards low momenta in the curve for the real pattern recognition can be ascribed to the decrease in hit purity. The increasing momentum resolution towards higher momenta is explained by the decrease in curvature of the track. The tracking performance with collision data is described in chapter 6.

3.6 Calorimetry

The Calorimetry system is used for the identification of electrons, photons and hadrons as well as a measurement of their energies and positions. All components of the system are synchronous and operate with a total latency of 4 μs with respect to the pp interaction. The fast response time enables the calorimetry system to operate at the LHC frequency (40 MHz) and provide high transverse energy hadron, electron, and photon candidates for the Level-0 (first stage) trigger [24].

The sub-detectors all work on the same principle: incident particles interact with a layer of absorption material creating a shower of secondary particles [21]. These induce light in a layer of scintillator, which is transmitted via wavelength-shifting fibres to photomultiplier tubes. The amount of light detected by the

[1] An alternative to forward tracking for long tracks reconstruction, track-matching combines VELO seeds with T station seeds. This method yields a higher purity, but also a significantly reduced efficiency, of reconstructed tracks compared with the forward tracking method.

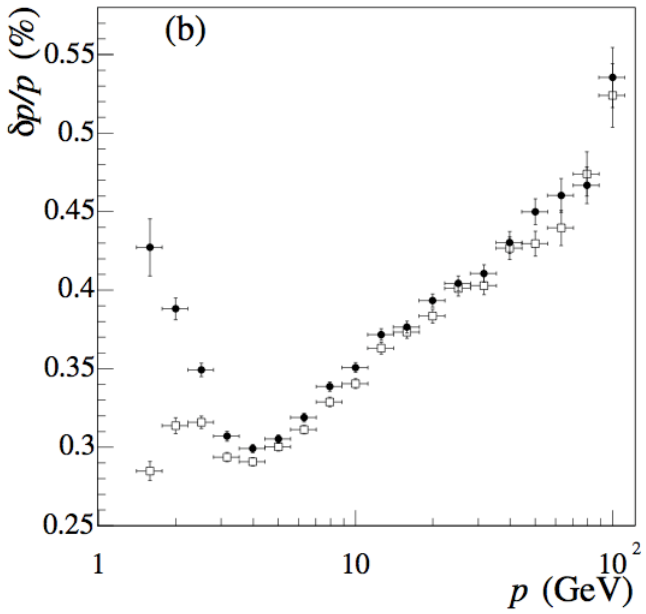

Figure 3.13: Momentum dependence of long tracks found by the matching and forward algorithms (filled circles) and of all particles reconstructible as long tracks (open boxes). The momentum resolution is determined from a single Gaussian fit in each momentum bin.

tubes provides a measure of the particle energy. All of the components have been designed and tested to be resistant to long-term exposure of high-energy radiation.

3.6.1 Scintillator pad detector/preshower and electromagnetic calorimeter

The electromagnetic calorimeter (ECAL) detects high-energy electrons and photons through the initiation and sampling of electromagnetic showers in the traversed material. The 3312 cuboid-shaped modules of the ECAL are orientated parallel to the beam line and incorporate a 'Shashlik' design, consisting of alternating layers of 2-mm thick (lead) absorber and 4 mm-thick scintillator material. With a total depth corresponding to 25 electromagnetic radiation lengths, the ECAL modules fully contain showers from high energy photons, minimising the energy resolution for these measurements. The chosen scintillator and absorber thicknesses has been chosen to maximise trigger performance, while

keeping the energy resolution to a level that satisfies physics performance. This is indeed the case for the energy resolution, as has been measured with an electron beam to be:

$$\frac{\sigma_E}{E} = \frac{10\%}{\sqrt{E}} \oplus 1\% \tag{3.1}$$

Two almost identical planes of scintillator, named the scintillator pad detector (SPD) and preshower (PS), sandwich a 15 mm-thick layer of lead absorber, directly in front of the ECAL. The SPD—in front of the absorber—detects only charged particle, which proves effective in tagging ECAL candidates as electrons or photons. It is particularly useful for rejecting the high background of $\pi^0 \rightarrow \gamma\gamma$ decays with high E_{T} that would otherwise swamp the electron trigger. Furthermore, the SPD provides a fast estimation of the charged track multiplicity per event for the Level-0 trigger [24]. The preshower (PS)—behind the absorber—provides separation between electrons and charged hadrons (pions in particular) by providing additional information on the shower shape [25].

At the calorimeters, the particle flux from the beam line to the outer edges differs by two orders of magnitude. Furthermore, the spatial resolution towards the outer edges is dominated by multiple scattering. The active areas of the SPD/PS and ECAL are therefore divided into three regions of different cell granularity—40.4×40.4 mm^2 (inner), 60.6×60.6 mm^2 (middle) and 121.2×121.2 mm^2 (outer)—as a compromise between occupancy, number of channels and spatial resolution. A photograph of the three different types of ECAL modules can be seen in Figure 3.14.

3.6.2 Hadronic Calorimeter

High energy hadrons can interact with matter via the strong nuclear force, generating a shower of lower energy hadrons. The HCAL, located behind the ECAL, is a sampling device made from iron absorber and scintillating tiles orientated parallel to the beam line. In the lateral direction, tiles are interspersed with 1 cm-thick iron, matching the radiation length in the material.

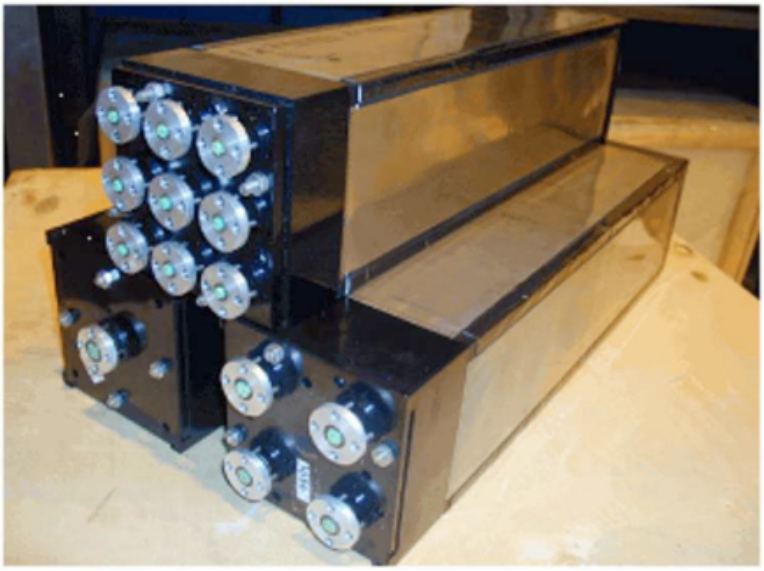

Figure 3.14: Photograph of the outer (bottom left), middle (bottom right) and inner (top) type ECAL modules.

Longitudinally, alternating absorber and scintillator tile are arranged on to master plates—the combined depth of one absorber and scintillator tile corresponds to the hadron interaction length in the material. This periodic structure is illustrated in Figure 3.15. The light in this structure is collected by WLS fibres running along the detector towards the back side where photomultipliers tubes (PMTs) are located.

The HCAL's only function is providing the Level-0 (first stage) trigger for high E_{T} hadrons, which requires a moderate energy resolution. The longitudinal space available for the HCAL to occupy (120 cm, equivalent to 5.6 hadronic interaction lengths in the HCAL structure) is adequate for this purpose. Similar to the ECAL and SPD/PS, the HCAL cell sizes are divided into zones, with an inner zone containing 860 square cells of size $\sim 13 \times 13$ cm^2 and an outer zone containing 608 square cells of size $\sim 26 \times 26$ cm^2. Readout cells of different sizes are defined by grouping together different sets of fibres onto one photomultiplier tube that is fixed to the rear of the sampling structure [21].

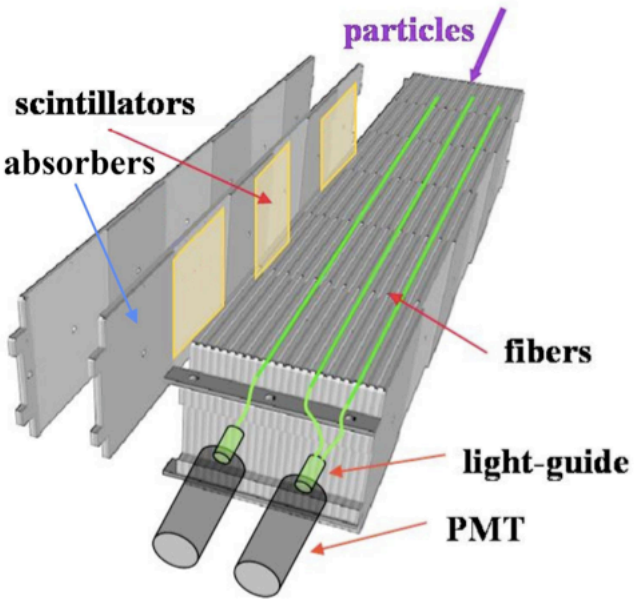

Figure 3.15: A schematic of the HCAL internal cell structure. The exploded view of two *scintillator/absorber* layers illustrates the elementary periodic structure of an HCAL module.

3.7 Muon system

Triggering and identification of muons is a vital step in reconstructing many interesting B-decays. The Muon system is located at the far-end of the detector and is used for the identification and tracking of high-momentum muons. The fast readout time (20 ns) enables the system to trigger on high p_T muons.

3.7.1 Design

The Muon system comprises 5 rectangular detector stations M1-M5 interspersed with iron filters that act as shields to traversing hadrons, as shown in Figure 3.16. The geometry of the 5 stations is projective, with transverse dimensions that scale with the distance from the IP. The full system comprises 1380 chambers. Each of the 276 chambers that are incorporated in a station are of an area dependent on the radial region in the station (R1-R4) as shown in Figure 3.17. As for the previous detectors mentioned, this is to maintain a constant particle flux and channel occupancy over the entire station. The granularity in the horizontal

(bending) direction is higher than in the vertical (non-bending) direction to provide a more precise determination of muon p_{T}.

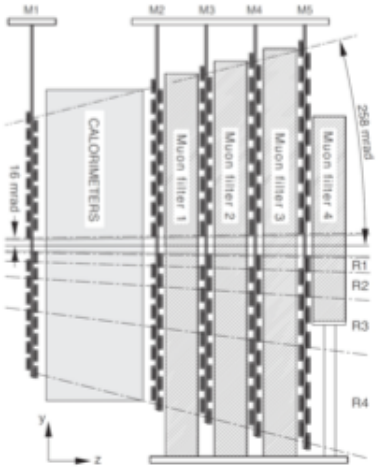

Figure 3.16: Muon station M1, located in front of calorimeter, and stations M2—M5, located behind calorimeter and interspersed with iron filters.

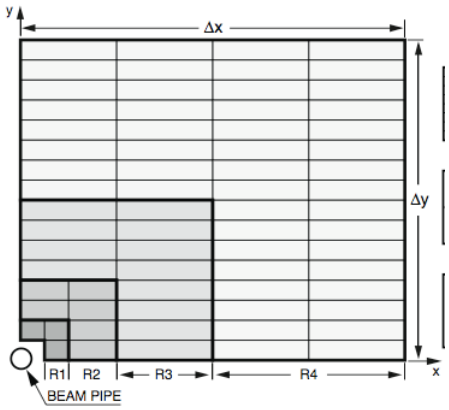

Figure 3.17: Planar view of chambers, with segmentation dependent on radial sectors R1—R4.

Muon detection is achieved through Multi-Wire Proportion Chambers (MWPCs), with the exception of the innermost region (R1) of M1 that uses Gas Electron Multiplier (GEM) technology. The technologies work on similar principles, where an incident charged particle ionises a chamber of gas and the resulting electron is accelerated under high voltage towards the anode. In the case of MWPCs, a cascade of electrons occurs in the vicinity of the anode, giving a resulting gain of the order 10^5 [26]. GEM technology uses a dielectric layer sandwiched between two copper foils (placed under a high potential difference) and perforated with holes at high surface density [27]. The large potential gradient at each hole induces an avalanche effect for passing electrons. Triple-GEM cells (three GEM layers before anode) are used for LHCb, resulting in a gain of the order 10^5.

3.7.2 Performance

The muon detector is performing very well and has already allowed for a multitude of physics channels to be extracted. One such example is the decay of the $\Upsilon(1S)$, $\Upsilon(2S)$, $\Upsilon(3S)$ (bound states of the $b\bar{b}$ pair) to a dimuon pair. The

behaviour of this process is well known and has proven to be effective in testing detector performance. By measuring the momenta of the muon pair and applying conservation of energy and momentum, the invariant mass can be calculated as shown in Figure 3.18. The distribution corresponds to a 4 pb^{-1} sample of beam data, with each of the Υ mass regions fitted with a single gaussian. It is clear that the momentum resolution of the muon stations is sufficiently low to resolve the 3 Υ mass peaks.

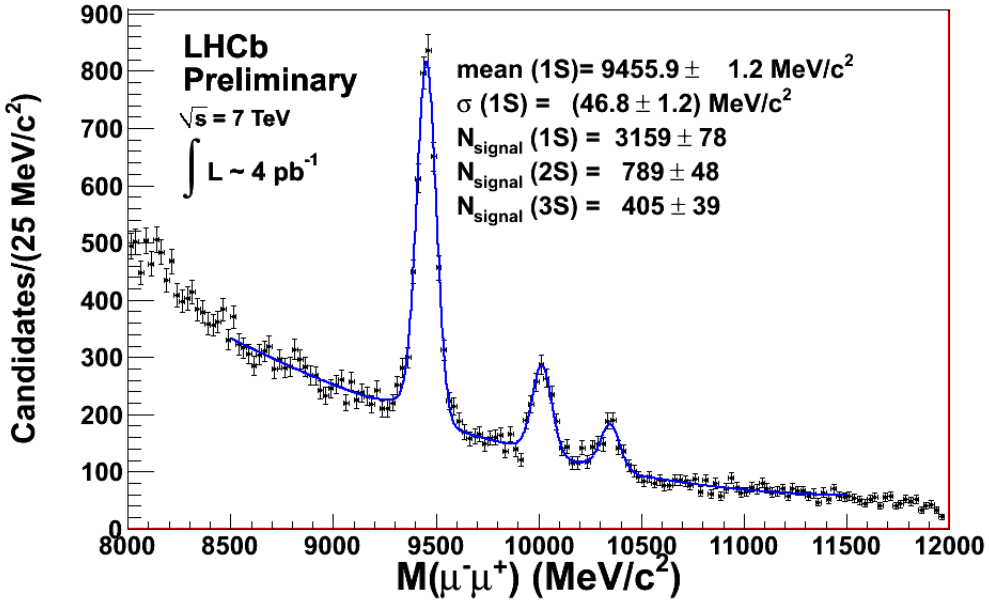

Figure 3.18: Invariant mass distribution of the $\Upsilon(1S)$, $\Upsilon(2S)$, $\Upsilon(3S)$ states, taken with the first 4 pb^{-1} of data.

A review of the ID performance of the muon detector as a function of transverse momentum and pseudo-rapidity y is described in chapter 6.

3.8 Ring Imaging Cherenkov (RICH) Detectors

The identification and separation of charged hadrons, in particular kaon-pion separation, is of great importance at LHCb. This cannot be achieved through the calorimeters alone, and so the RICH is employed that combines momentum information with photonic emission angles to infer the mass of the charged

particle. Two RICH detectors are used for particle identification at LHCb: RICH1, which covers the low-momentum range of charged particles (up to 65 GeV); and RICH2, which covers the high momentum range of charged particles (up to 100 GeV). Low momentum charged particles may be swept outside the LHCb acceptance by the magnet before reaching downstream detectors, and so RICH1 is located upstream of the magnet. The two detectors are similar in design, consisting of a pair of lightweight spherical mirrors, a pair of plane mirrors and a pair of photon detector arrays, all located on opposite sides of the beam pipe. While the layout of RICH2 is horizontal (to either side of the beam pipe), for RICH1 it is vertical (above and below the beam pipe) so that the photon detectors can be located in a region where soft iron magnetic shielding can be used, as shown in a schematic of the detector (Figure 3.19).

A detailed explanation on the design and operation of the photon detectors is given in chapter 4.

3.8.1 Operational Principle

A charged particle traverses through a dielectric medium that polarises the atoms in the medium. The atoms immediately turn back to their ground state, emitting radiation in the process. If the velocity of the particle in the medium is faster than the phase velocity of the speed of light in that medium, the photons will constructively interfere and intensify the radiation. A cone of light is created at an angle θ_{C} to the particle trajectory, dependent on the refractive index of the medium n and speed of the particle $\beta = v_{\mathrm{p}}/c$ in that medium:

$$\cos\theta_{\mathrm{C}} = \frac{1}{n\beta} \tag{3.2}$$

This is known as the Cherenkov effect and the angle θ_{C} is the Cherenkov angle. The spherical mirrors focus these light-cones into rings of light before they are directed onto the photodetector arrays. For the choice of radiators, RICH1 incorporates both aerogel tiles and C_4F_{10} gas, while RICH2 uses CF_4 gas exclusively. The Cherenkov angle θ_{C} as a function of particle momentum is shown

in Figure 3.20 for the three radiators. The expected Cherenkov angle θ_C depends both on the track momentum and the type of particle.

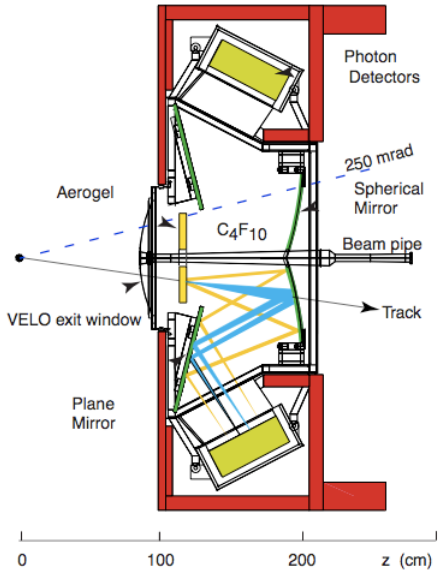

Figure 3.19: Side-view of RICH1 detector, including optical paths of Cherenkov light emitted from a charged particle track.

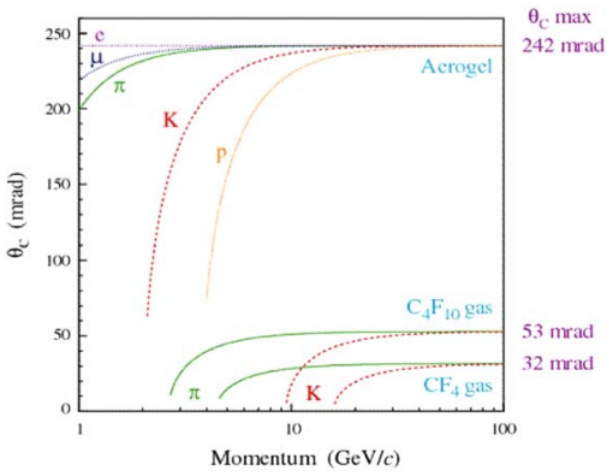

Figure 3.20: Momentum dependency of θ_C for a range of charged particles.

3.8.2 Particle Identification (PID)

PID can be performed in a number of ways with and without tracking information. The most effective technique relies on tracking information and involves calculating *likelihoods* of hypothesised particles. This can be performed on a per-track basis[1], and requires the momentum and trajectory of the track through the RICH detector, as well as the array of pixel hits in the photodetectors. Assuming the emission point to be the mid-point of the trajectory in the radiator, one can extrapolate back – via the optics of the RICH – to find the emission angle of each photon with respect to the reconstructed track. The likelihood matches the emission angle of all recorded photons with the expected Cherenkov angle for a

[1]This can be taken a step further and performed "globally" i.e. over all reconstructed tracks simultaneously. Such a method takes into account intersecting rings, which forms the dominant background when performing this likelihood calculation [28].

given particle hypothesis (itself calculated from 3.20). This is then maximised by systematically considering a different θ_c for each particle hypothesis (π, K, e, μ).

3.8.3 Performance

The PID performance is dominated by σ_θ the reconstructed Cherenkov angular resolution, and some contributions to this resolution are pre-determined: the uncertainty in the (estimated) *emission point* of Cherenkov photons introduces an uncertainty on the impact point on the HPD plane due to the tilt of the spherical mirrors; the HPD *pixel size* limits precision; the range in *chromaticity* of emitted Cherenkov photons introduces a spread in the refractive index and ultimately θ_{C}; and track resolution affects the calculation of θ_{C}. These factors contribute a total expected θ_{C} resolution of 1.6 mrad for RICH1 and 0.7 mrad for RICH2. In practice the initial measured resolutions were significantly worse than this, resulting mainly from magnetic field distortions and geometrical misalignments. A description of these contributions, as well as the steps taken to minimise their effect, is given below.

Mirror Alignment

Studies with a simulated detector have provided an understanding of how misalignments can effect measurement of collision data. By analysis of collision data to find these effects, we can choose which components to align and by what magnitudes.

Deviations in θ_{C} (from the average) of every photon is calculated and plotted against the azimuthal angle ϕ on the ring. Misalignments are observed relative to tracking, and manifest as a sinusoidal dependency with respect to ϕ. It has been found that the magnitude of the sinusoidal dependency varies significantly between mirror segments. Figure 3.21 contains a distribution of $\Delta\theta_{\mathrm{C}}$ plotted against ϕ for a particular mirror segment in RICH1, showing a significant sinusoidal dependency. After making corrections at the reconstruction stage with respect to mirror rotations, the deviation vanishes (Figure 3.22). This can be performed in a similar way to other segments, yielding a total resolution of

2.2 (1.9) mrad for RICH1 (RICH2), a result that is much more consistent with expectations than before [29].

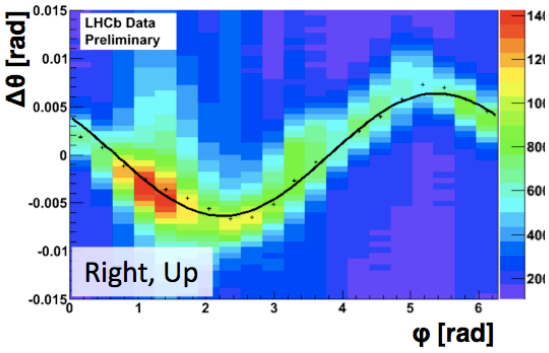

Figure 3.21: Photon $\Delta\theta_C$ w.r.t azimuthal angle ϕ, without corrections.

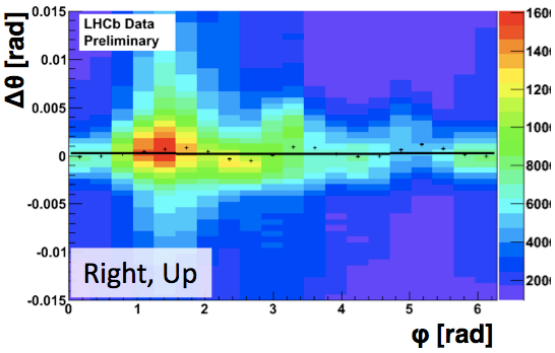

Figure 3.22: Distribution of photon $\Delta\theta_C$ w.r.t azimuthal angle ϕ, with corrections.

The kaon PID performance as a function of transverse momentum p_T and pseudo-rapidity y is described in chapter 6.

3.9 The Trigger System

Under nominal running conditions, the LHC collides bunches at a rate of 40 MHz. The low luminosity and bunch structure will provide 10 MHz of interactions visible[1] to LHCb, which will contain $b\bar{b}$ pairs at a rate of the order 100 kHz. However, only 15% of these events will contain a B-meson with all decay particle inside the LHCb acceptance. In addition, the branching ratios of interesting B-decays (e.g. for CP-violation or rare decay studies) are typically less than 10^{-3} [30]. The need for a trigger arises in order to reduce the event rate to a level that can be stored for offline analysis, whilst achieving the highest efficiencies of interesting B-decays. The LHCb trigger is separated into 2 stages: the Level-0 (L0) trigger reduces the rate from 10 MHz to 1 MHz and is made from custom electronics; the High Level Trigger (HLT) further reduces the rate to 2 kHz and is executed on a farm of processors.

[1] Visible means that at least two charged particles produce enough hits in the tracking system to be reconstructed

3.9.1 Level-0 Trigger

The Level-0 (L0) trigger comprises the first stage of triggering in the detector. It is designed to deliver a "yes or no" decision to the next stage of the trigger every 25 ns, with an accept rate limited to 1 MHz. It is purely a hardware trigger, fed with information from the Calorimetery system, Muon system and VELO pile-up veto. The latency of L0 i.e. the time elapsed between a pp interaction and the arrival of the L0 trigger decision at the front-end electronics, is fixed to 4 μs. This time which includes the time-of-flight of the particles, cable delays and all delays in the front-end electronics, leaves 2 μs for the processing of the data in the L0 trigger to derive a decision [21].

The trigger configuration has evolved from earlier configurations that required only a minimal amount of activity in the detector. Events with large pile-up multiplicity (> 3) or SPD multiplicity (> 2) would be indicative of a non-diffractive collision, and thus accepted by the trigger. Over time though, the focus has shifted towards a core physics program and a trigger line that is optimised for B-decays. The large mass of B-mesons provides a significant amount of kinetic energy to the decay particles. The L0 selections take advantage of this by searching for the highest p_{T} and E_{T} candidates and applying minimum thresholds, thus narrowing the selection on these decay particles. Table 3.1 shows the main L0 lines used in the 2010 physics program [31]. Dimuon pairs – common in many interesting physics channels – are selected by searching the muon stations for the two highest p_{T} candidates. Most L0 triggers are selected due to one L0 trigger type, with about $\sim 15\%$ of the L0 events selected by multiple triggers.

Particle	Threshold
μ	$p_{\mathrm{T}} > 320$ MeV
di-μ	$\Sigma p_{\mathrm{T}} > 400$ MeV
e	$E_{\mathrm{T}} > 750$ MeV
γ	$E_{\mathrm{T}} > 2700$ GeV
h	$E_{\mathrm{T}} > 1220$ MeV

Table 3.1: L0 trigger lines of the core physics program, with corresponding thresholds.

3.9.2 High-Level Trigger

The High Level Trigger (HLT) forms the final stage of triggering in the detector, running on events that pass the L0 trigger. The HLT is implemented through a set of C++ algorithms executed on a CPU farm containing about 1800 nodes [30]. All of the data from the detector, apart from the RICH detectors, is made available for the HLT to refine and enrich the B-content of triggered events. The HLT is further split up into two parts, referred to as HLT1 and HLT2. HLT1 aims at limiting the L0 output rate from a MHz to a few kHz. It applies different sequences of algorithms (called alleys) according to the type of candidate on which the L0 decision was taken. In general, several different alleys are executed for each L0 trigger type—if any of the alleys are accepted the event is passed to HLT2.

HLT2 aims at reducing the output rate to $\sim$ 2 kHz before the data is sent offline. The combined output rate of events accepted by the HLT1 alleys ($\sim$ 10 kHz) is sufficiently low to allow a reconstruction of all the tracks in the event. Resonances are created from tracks with loose cuts applied on their momentum and impact parameter. These tracks are used to form composite particles, like $K^* \to K^+\pi^-$ and $J/\psi \to \mu\mu$, which are subsequently used for all selections to avoid duplication in the creation of final states. The choice in HLT2 trigger lines is driven primarily by the need for interesting beauty and charm physics, but there also exists separate lines that are used for calibration purposes. Figure 3.23 shows the architecture of the LHCb trigger containing the L0 and HLT alleys. Cells on the same row represent the same "family" of HLT selections that are performed on the corresponding L0 candidate.

Each HLT1 alley and HLT2 selection produces summary information which is written to storage for the accepted events. This summary contains the information of all tracks and vertexes which triggered the event. The summary information is used to check if an event would have triggered, even if the B decay of interest would not have participated in the trigger. It therefore allows for studying of the trigger performance.

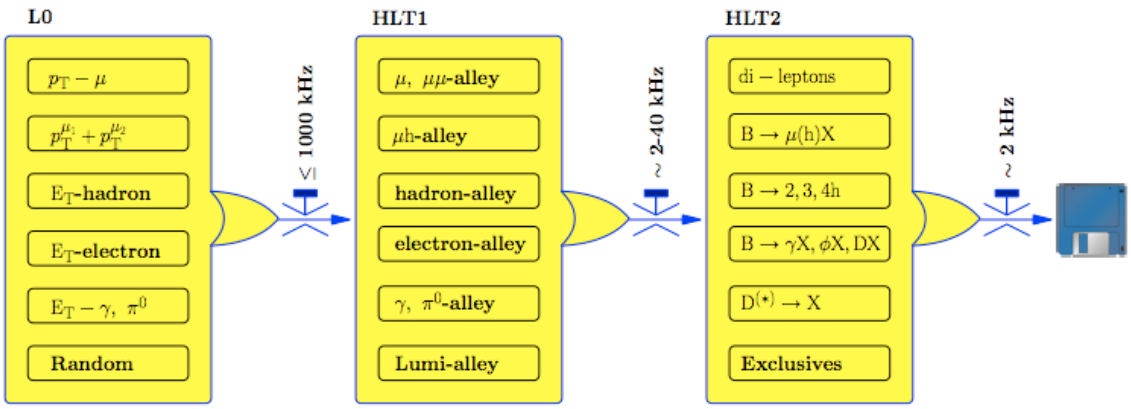

Figure 3.23: Architecture of the L0, HLT1 and HLT2, with desired output rates.

3.10 LHCb software

For data processing at LHCb, consistency is essential in the running of the many software modules. The GAUDI [32] framework is used for exactly this purpose, providing the skeletal structure upon which each and every algorithm is initialised, executed (event-by-event), then finalised. The consistency extends to the type of data, where physical data and simulated data can be treated in a similar way. There are four main applications which are built upon the Gaudi framework, each assigned to handle a different stage of the event processing:

- *Gauss* provides the interface with which to configure and run the event generation phase (e.g. proton collisions) and a subsequent phase where the particles are propagated through the LHCb detector. The associated software Pythia [33] and GEANT4 [34] are described in more detail in Chapter 5.
- *Boole* digitises the detector elements.
- *Brunel* reconstructs the detector hits into tracks and assigns particle identification likelihoods based on the relevant information e.g. Cherenkov angle.
- *DaVinci* provides customised algorithms for event filtering and re-processing, in addition to output data manipulation.

3.11 Luminosity measurements

Integrated luminosity measurements are necessary to determine the absolute cross-sections of reaction processes and are valuable to quantify the performance of the accelerator. The luminosity is proportional to the average number of visible proton-proton interactions in a beam-beam crossing. For a given period of data-taking, the integrated interaction rate can be used to determine the integrated luminosity if the cross-section for these visible interactions is known. The cross-section corresponding to these visible interactions is determined using independent data runs, as described in [35], which provides the necessary calibration factor.

These dedicated data runs evaluate the 'overlap integral', one of the necessary parameters of a luminosity calculation, over the transverse and longitudinal directions of the two beams. The beam position scanning method, invented by van der Meer, exploits the ability to move the beams in both transverse co-ordinates with high precision and to thus scan the colliding beams with respect to each other [36, 37]. Alternatively, the beam-gas imaging method uses the reconstructed distribution of vertices from beam-gas and beam-beam interactions to obtain an image of the transverse bunch profile along the beam trajectory [38]. Combined with a measurement of the bunch populations gives the luminosity, which can then be translated into the visible cross-section by counting the total number of visible interactions. The visible cross-sections were shown to be in good agreement between the two methods, yielding 58.4 mb for the van der Meer method and 59.9 mb for the beam-gas imaging method. The combined result has a relative uncertainty of 3.5%.

In the first LHC physics run that started in March 30, 2010, the centre-of-mass energy was $\sqrt{s} = 7$ TeV, reducing the expected $b\bar{b}$ and $c\bar{c}$ production rates as compared to the nominal energy of $\sqrt{s} = 14$ TeV, without any major impact on the physics reach. Whilst the nominal instantaneous luminosity has been reached only at the beginning of 2011, the lower luminosity at the start-up in 2010 allowed for lower trigger thresholds, and hence better efficiencies for hadronic B decays ($\sim 75\%$) [39]. Throughout 2011, gradual increases in the bunch intensity (protons per bunch) increased the average number of visible interactions per bunch crossing. By the end of 2011, the detector was operating with as many as

6 visible interactions per crossing, almost 4 times the rate observed in 2010.

3.12 Outlook

The LHC collides protons at an un-precedented energy and luminosity, producing B-hadrons at a rate that far exceeds that of any other collider. The copious amount of B-hadrons are used by the LHCb experiment to make precision measurements of CP violation in this quark sector. In chapter 4 I describe a characterisation of the Hybrid Photon Detectors of the RICH detectors. In chapter 5, 6 and 7 I present a measurement of $B^{\pm}$ hadron production asymmetry and cross-section using reconstructed $B^{\pm} \rightarrow J/\psi K^{\pm}$ decays.

Chapter 4

Hybrid Photon Detectors for the LHCb-RICH

Cherenkov photon detection in the LHCb-RICH detectors is accomplished through the use of hybrid photon detectors. This chapter reviews the performance of this technology, from the initial post-production tests at Edinburgh to the later data runs at the RICH detectors. The majority of the chapter discusses the ion feedback phenomenon, which is related to the quality of the vacuum in the tube body. Vacuum degradation limits the lifetime of an hybrid photon detector, which has otherwise displayed an excellent performance in the RICH detectors.

4.1 Design of a hybrid photon detector

A hybrid photon detector (HPD) is an amalgamation of two technologies - vacuum technology and solid-state technology - to produce a device that meets the required specifications for detection of Cherenkov photons. This includes:

- Single photon sensitivity
- High sensitivity in the range of the Cherenkov emission spectra (200–700 nm)
- High granularity (2.5 mm $\times$ 2.5 mm at the entrance window)

- Fast readout time (25 ns)

An HPD consists of a silicon detector anode assembly encapsulated in a vacuum envelope as illustrated in Figures 4.1 and 4.2. The vacuum tube has a 7 mm-thick quartz entrance window coated with an S20 multi-alkali photocathode. Photoelectrons emitted from the photocathode are accelerated (at a potential $\leq$ 20 kV) and focussed onto the pixellated silicon detector. The cross-focussing electrostatic field, with de-magnification factor $\sim$ 5, is shaped by electrodes at 3 intermediate potentials.

A custom-built binary readout chip, called LHCBPIX1, is bump-bonded to the silicon anode and the complete assembly is encapsulated within the vacuum of the photodetector. The chip pre-amplifies and shapes the analogue signals; hits are assigned by comparing these signals to a global minimum threshold at a rate of 40 MHz (equivalent to the bunch-crossing cycle of the LHC). The sensor chip is divided into 256 $\times$ 32 pixels each with size 62.5 μm $\times$ 500 μm. The chip operates in two modes: ALICE and PHYSICS mode. For the former mode, all 8192 pixels are read out and the data transmitted over the equivalent number of channels. For the latter mode, groups of 8 pixels are read out in logical OR-mode to give an effective 32 $\times$ 32 channel array; each of these grouped pixels measures 500 $\times$ 500 μm and is referred to as an LHCb pixel. This mode is chosen for data-taking as it reduces the output data-size while maintaining a suitable granularity (2.5 mm $\times$ 2.5 mm at the entrance window). Data packets from the LHCBPIX1 chip contain not only the pattern of hits but also information on the event, on the HPD and on the integrity of the data acquisition.

4.2 Post-production Testing

In order to ascertain the suitability of each HPD for use in the RICH detectors, a series of tests is carried out to characterise the performance of the HPD. These tests are performed at the Photon Detector Test Facilities (PDTF) in Edinburgh and Glasgow typically a month after HPD production. A comprehensive set of parameters are tested for in an HPD, including:

- Photocathode: Dark Count, Response to Photons, Quantum Efficiency.

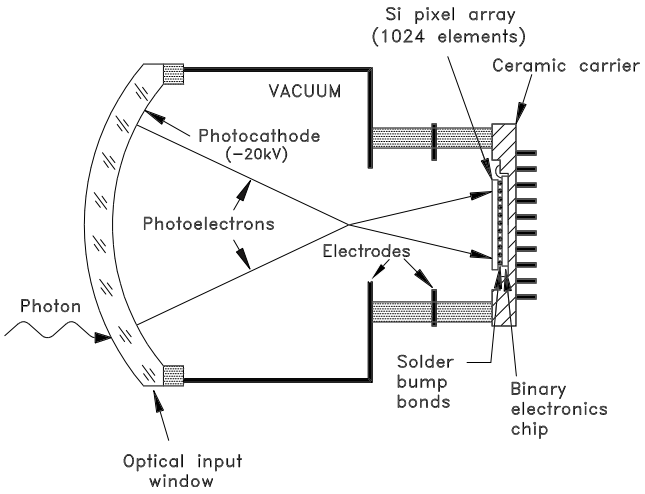

Figure 4.1: Schematic of an HPD. A photon, incident on the quartz window, is converted to a photo-electron and accelerated onto the silicon pixel sensor.

Figure 4.2: Photograph of an HPD, undergoing cleaning as part of the routine inspection procedure.

- Electron Optics/Tube Volume: Imaging, Demagnification, High Voltage Stability, Field Distortions, Ion Feedback, Vacuum Quality.
- HPD Body: Physical Dimensions, Quartz Window, Pin Grid Array, Sensor Position.
- Silicon Sensor: Characteristic IV Curve, Depletion, Bump Bonding, Efficiency.
- Readout Chip: Connections, Communications, DAC Linearity, Readout Modes, Dead Channels, Noisy Channels, Pixel Masking, Threshold, Noise.

A thorough visual inspection of the HPD body is crucial in identifying any imperfections in the component assembly. This includes a check of the cabling, quartz window, and indium seal. The HPD is mounted on a retractable jig to measure the vertical alignment of the body. Only 2 out of the 557 HPDs delivered to the PDTF's failed a visual inspection; these were subsequently returned to the manufactured and repaired.

For the operational aspect of testing, the HPD is mounted inside a light-tight dark box in a way that allows the external cables and pin array of the HPD to be connected to the test system. Data output from the HPD is analysed

in a PC, which also sets all input parameters for the test procedure. A series of electronic circuit boards act as a data translator between the HPD and PC, and also control the power supplied to the HPD. Two external supplies are used to power the HPD: the High Voltage (HV), which supplies the accelerating and focussing electrostatic field of the electrodes, and the Low Voltage (LV), which supplies the power to the readout chip and electronics. A blue LED (470 nm) located inside the dark box and incident on the entrance window is designed to emit pulses of light of width 15 ns and intensity 2-4 photons per pulse. The test procedure is carried out using the software LabView, which automates the majority of the procedure.

Communication tests between the pixel chip and the associated electronics are performed. A test on the optimum setting of the voltage threshold is also performed by directly injecting a charge pulse and scanning over a range of thresholds. The global optimum threshold is one which maximises the chip response to the test pulse while minimising chip response to electronic noise. Individual pixel thresholds can then be optimised by fixing the global optimum threshold and varying the size of the test pulse. In testing, the HPDs have achieved an excellent signal-to-noise ratio of 27[1], well exceeding the specification of > 12 [40]. The position of any dead pixels, which occur as a result of a degraded bump bond, are also recorded at this stage. A requirement of < 400 dead pixels is imposed on the HPD; all HPDs have passed these specifications. In addition, the number of noisy pixels has been found to be negligible for all tested HPDs.

The HV is ramped up slowly from 0 to –18 kV[2], and the response to photons during the process is measured by illuminating the photocathode with the LED. A similar procedure is performed while ramping the bias voltage applied to the silicon sensor chip from 0 to 90 V. The leakage current—the current in the chip in the absence of photoelectrons—is also measured as a function of applied bias voltage. Figure 4.3 shows the photoelectron response of a typical HPD as a function of HV. At HV higher than $\sim$ 5 kV an increasing response is observed as the photoelectons acquire the minimum energy required to fire on pixels. At

[1]Signal Over Noise S/N = (C - T)/N where C = 5000^e the average signal charge, T = 1065^e average threshold and N = 145^e.

[2]18 kV is considered a safe maximum for operation of the HPD; this applies not only to PDTF testing but to operation in the RICH as well.

HV higher than $\sim$ 10 kV a 'charge-sharing' effect occurs, where the incident photoelectron deposits its energy on two adjacent pixels. While a low energy electron may not have sufficient energy to fire on either pixel—causing a reduction in detection efficiency—a high energy ($>$ 13 kV) electron may fire on one or both pixels, causing the hit-rate to diverge from the cluster-rate. A second, and more predominant, mechanism is known as backscattering. When a photoelectron strikes the pixel sensor there is a chance it may rebound, thus depositing only a fraction of its energy. If this energy is insufficient to fire on the pixel, and if the rebounded electron also fails to fire on a pixel (e.g. HPD time window has closed), the signal remains undetected [41]. The backscattering process reduces the detection efficiency, causing the reduced slope at ($>$ 13 kV). All tested HPDs have passed the specifications for HV ramp-up and bias ramp-up.

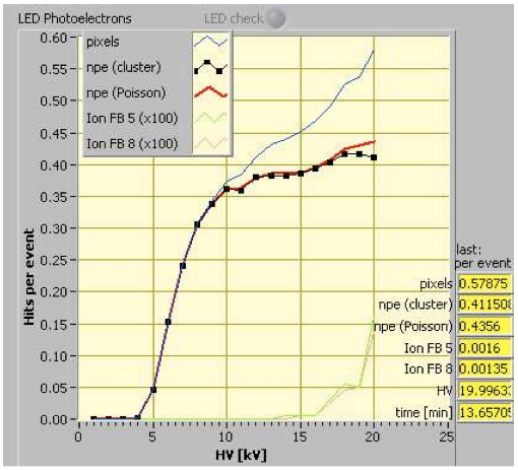

Figure 4.3: High Voltage ramp-up from 0 - 18 kV. Increase in detection efficiency is observed as a result of single pixel ($>$ 5 kV) and multiple pixel ($>$ 13 kV) turn-on.

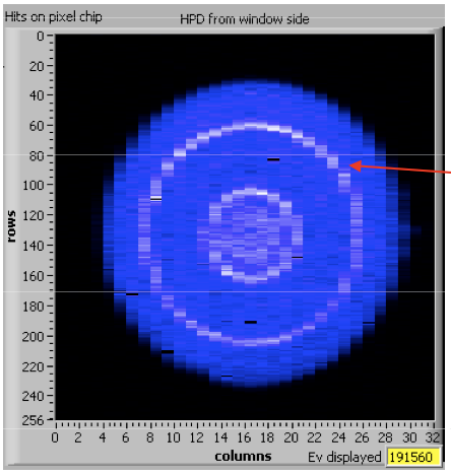

Figure 4.4: Photocathode image during a pulsed LED run. High intensity rings (red arrow) result from total internal reflection in the quartz window.

Accumulated data is then recorded while the HPD is fully ramped, both with and without illumination from the LED. The build-up of pixel hits creates a circular image on the chip as depicted in Figure 4.4. Light falling on the edge of the quartz window is reflected back onto the pixel chip by the aluminium coating, creating the characteristic ring of light inside the image. A relative displacement of the image centre greater than 1 mm may cause a signal loss when in a magnetic field. Improvements in the manufacturing process have seen the displacement

maintain at 0.6 LHCb pixels, well below the required specifications. Under no illumination, 90% of HPDs were found to have an excellent dark-count rate ($<$ 5 kHz/cm^2, corresponding to a 1% probability for 1 hit/HPD/event). Higher dark-count HPDs may still be suitable for use in the RICH—these elevated rates are due either to a high red sensitivity or an increased ion feedback probability. The occurrence and measurement of ion feedback is described in more detail in section 4.4.

Quantum efficiency is the probability of photoconversion, which calculates the ratio of the number of produced photoelectrons to the number of photons incident on the quartz window. This is tested for at the PDTF stations by shining a wavelength-filtered light source at the HPD and measuring the resulting photocurrent. The photocurrent drawn from a reference photodiode provides a measure of the photon intensity. One of the most significant improvements in the manufacturing performance is the increase in quantum efficiency in the UV-visible regions, as shown in Figure 4.5. Furthermore, a reduction in the red sensitivity ($\sim$ 800 nm) has been achieved, a region that causes a considerable amount of noise through thermal electron emission from the photocathode.

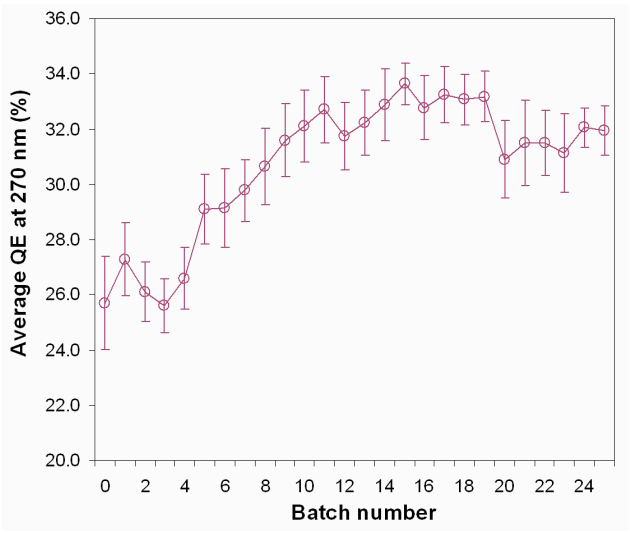

Figure 4.5: Evolution of the conversion efficiency of photons at 270 nm ($\sim$ equivalent to the Cherenkov wavelength) over time, quantified by batch number. A clear improvement is evident.

The first set of 557 tested HPDs showed an exceptionally high pass rate, with $\sim 98\%$ of HPDs eligible for use in the RICH detectors. To this day, batches of HPDs containing either new or repaired HPDs arrive at the PDTF for testing.

4.3 Operation in the RICH Detectors

My arrival at CERN in October 2008 coincided with the beginning of the operational phase of the RICH detectors. The majority of my time was therefore devoted to the testing of HPDs mounted within the RICH1 and RICH2 arrays. Tests were executed remotely from within the LHCb control room, with the recorded data sent to the CERN storage system for analysis. The results shown in this section are of my own work, with the exception of the time alignment study that is described in more detail in Ref. [42] and [25].

4.3.1 HPD Integration

Groups of HPDs are assembled into the four magnetic-shielding boxes of the RICH detector (two for RICH1 and two for RICH2). The HPDs are mounted onto adjacent columns that are staggered length-wise to give a hexagonal arrangement as shown in Figure 4.6. Each HPD is surrounded by a 1 mm–thick cylindrical magnetic shield that protects against stray external B-fields up to 5 mT (the maximum field value within the shielding in RICH1 has been measured to be 2.4 mT). There are 2×7 columns in RICH1 with 14 HPDs per column, and 2×9 columns in RICH2 with 16 HPDs per column, giving a total of 484 vacancies for the RICH detector. The columns also contains front-end electronics boards (one per pair of HPDs), LV and HV power supply distribution, cabling and active cooling. All front-end components have been designed and tested to be highly resistant to damage from radiation and from radiation-induced upsets in data transmission.

Connected to every pair of HPDs is a Level-0 (L0) electronics module; the module reads data from the chips of the two HPDs and provides interfacing for the Trigger Fast Control (TFC) system, Data Acquisition (DAQ) and Experimental Control System (ECS). The module also routes an external Low Voltage (LV) supply to

Figure 4.6: Photograph of close-packed hexagonal arrangement of HPDs in the RICH1 detector.

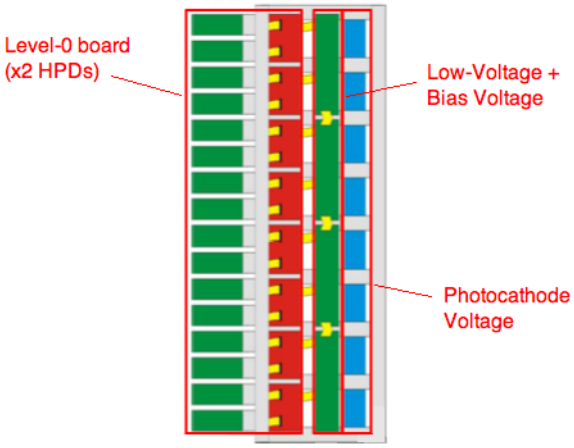

Figure 4.7: Front-end components of a single column, housed in a single mechanical module. The LV and HV distribution boards power the entire HPD and L0 system.

the LHCBPIX1 chip and a bias voltage to the silicon sensor of the HPD. At the heart of an L0 module is the Pixel Interface (PINT) field programmable array, whose main functionality is to control data formatting from the readout chip while decoding input signals from the Experimental Control System (described below). The data packets are 16 events deep, and allow the readout up to the corresponding number of consecutive bunches. Formatted data from the PINT is serialised and transferred to the off-detector DAQ system via a Vertically Cavity Surface Emitting Laser (VCSEL). Located behind the L0 modules are the LV and HV distribution boards; the LV boards power both L0 boards and HPD electronics, while the HV boards supply the 3 required potentials to the electrodes of every HPDs. A picture of a typical column, indicating the position of each component, is shown in Figure 4.7.

The RICH hardware is completely software-controlled and can operate either globally or locally. In local mode, full control is handed over to RICH shifters who have the opportunity to perform dedicated tests on the detector. When in global mode e.g. during periods of beam collisions, the RICH is operated as part of LHCb and can only be intervened by the shifters if a problem persists.

The Experimental Control System (ECS), composed primarily of a linked

collection of PVSS tools, oversees the entire operation of the RICH; the ECS provides an interface to the RICH sub-systems as well as centrally provided sub-systems e.g. LHC, cooling. The Detector Control System (DCS) controls the LV and bias supplies, and also provides some essential monitors including the HPD column temperature. The TFC system controls the readout of the HPDs, transmitting LHC clock and L0 trigger signals along optical fibres to the L0 modules. The TFC also selects the readout mode in which the LHCBPIX1 chip will operate.

4.3.2 Time Alignment

Each HPD has a 25 ns digital readout window over which the readout chip measures the integrated charge from every channel. The execution of this process must be synched to the arrival of Cherenkov (signal) photons for every HPD in the RICH system. Because of the differing timing characteristics of HPDs, their simultaneous execution will be non-optimal and individual time delays must be introduced. The TTCRx card, located inside each L0 module, allows a variable delay per HPD pair with respect to the global clock. While it is not possible to time-align individual HPDs, their positions in the RICH are chosen such that HPDs in an L0 pair have similar timing characteristics e.g. similar leakage current.

When illuminating the detector planes with pulsed laser light and applying a global scan in delay, a time-dependent response in efficiency is observed for each HPD pair. Characteristically this response shows an asymmetric plateau of approximate width 25 ns. The relative offsets were recorded and used as input to a time-corrected run. The final stage involved a confirmation and fine-tuning of the alignment using Cherenkov light from beam collisions. A periodic drift in profile was observed for HPDs at increasing distance from the beam pipe—this was corrected for. Figure 4.8 and 4.9 shows, respectively, a distribution of time profiles for the 98 L0 boards of RICH1 and the 144 L0 boards of RICH2 after making the correction. As of April 2010 the RICH1 (RICH2) HPDs were aligned with an rms of 1.1 ns (0.8 ns), well within the margins of optimum sensitivity.

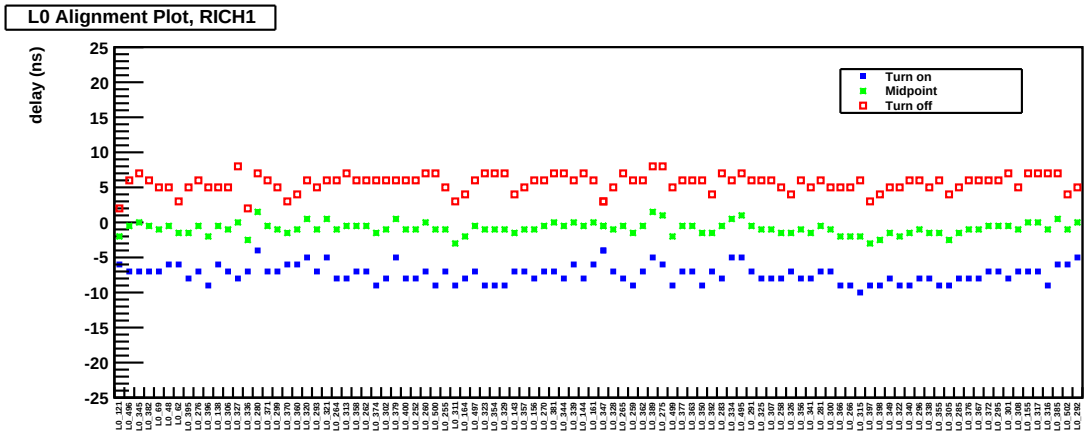

Figure 4.8: Plateau response of RICH1 L0 boards to Cherenkov light, with corrections applied. Average deviation of mid-point (green) of the order 1 ns.

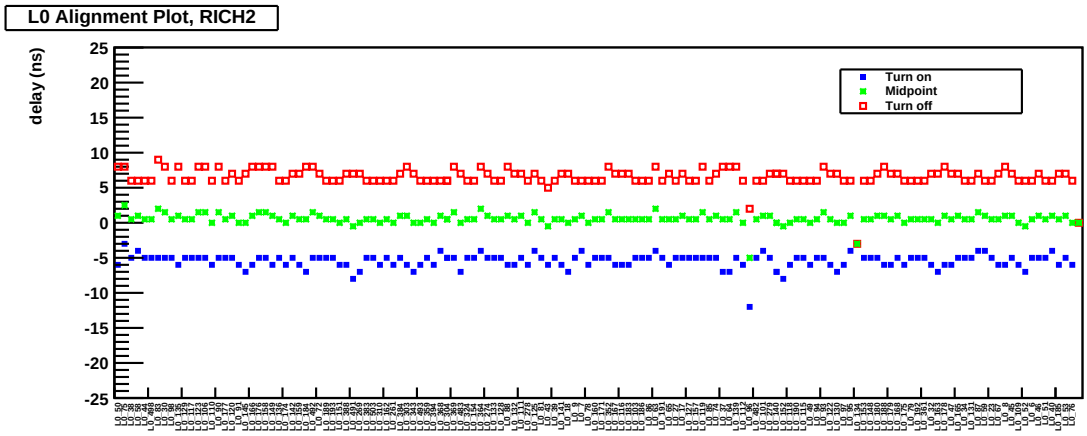

Figure 4.9: Plateau response of RICH2 L0 boards to Cherenkov light, with corrections applied. Average deviation of mid-point (green) of the order 1 ns.

4.3.3 Hit Multiplicities

At the time of start-up of the LHC, the RICH detectors were fully commissioned and ready to detect Cherenkov photons produced from charged particles emerging from pp interactions. Figure 4.10 and 4.11 show pixel hit-maps of the RICH1 and RICH2 HPD panels respectively, indicating the range in occupancies observed over the detector plane. Beam collisions at a centre-of-mass energy $\sqrt{s} = 7$ TeV have produced hit multiplicities of up to 8000 and 12000 per detector per event, while the typical multiplicity is 3000 and 4500 hits per detector per event, for RICH1 and RICH2 respectively.

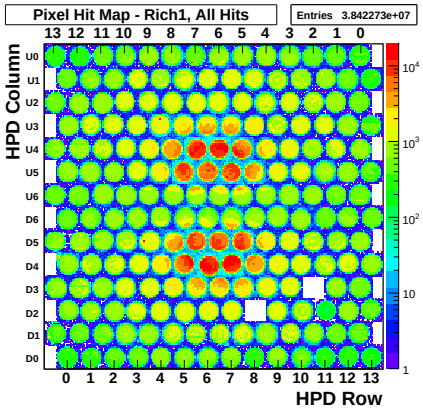

Figure 4.10: RICH1 pixel hit-map, under illumination from Cherenkov light. HPDs with no response (white squares) have damaged optical links.

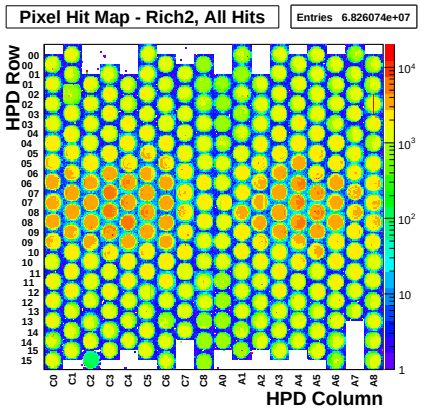

Figure 4.11: RICH2 pixel hit-map, under illumination from Cherenkov light. HPDs with no response (white squares) have degraded vacuums and have been removed.

4.4 Ion Feedback Studies

The development of vacuum degradation was first observed during routine testing of HPDs mounted on a test column. Though under no illumination, a highly elevated noise level was observed for three of the HPDs after ramp-up of the photocathode: at 3 kV the photocathode image was completely saturated; at 6 kV the entire silicon sensor was saturated. The proposed cause of this was ion feedback, a process involving gas ionisation in the tube body.

4.4.1 Ion Feedback

Ion feedback refers to the process where a photoelectron ionises a residual gas molecule in the body of the HPD. This positive ion is accelerated towards the photocathode, where it causes the emission of a shower of secondary electrons. The spread in electrons result in a large cluster of pixel hits generated on the silicon chip. Because of the slow drift time of the positive ion, the arrival of the secondary photoelectrons are delayed by typically 250–300 ns with respect to the original photoelectron. Due to the cross-focussing nature of the electrodes, the probability of gas ionisation is greatest at the centre of the vacuum tube, giving a cluster distribution that peaks in the centre of the photocathode image.

Ion feedback occurs in all HPDs to varying extent, though for the majority of HPDs an excellent vacuum quality is retained. The ion feedback probability of a healthy HPD is $< 1\%$, corresponding to the detection of less than 1 ion feedback signal per 100 photoelectrons. The process alone thus contributes only a negligible increase in noise, but will eventually present a problem when self-induced ionisation occurs. This can only happen for HPDs that have a significantly degraded vacuum, such that the gas concentration is high enough to continue the ionisation process without the need for incident photons. Noise levels in the chip reach saturation point and the HPD is no longer suitable for use in the RICH detectors. Self-induced ionisation is often called the "glow" effect, in relation to the faint blue light that is observed in the centre of the quartz window. This is thought to be due to the recombination of ions, which rapidly deteriorates the photocathode over time. As we shall see later, there is a systematic increase in observed ion feedback, which makes the possibility of eventual glowing a very likely scenario for every HPD.

4.4.2 Identifying Ion Feedback

Ion feedback measurements of HPDs are made both at the PDTFs and *in situ* in the RICH detectors. While each method differs based on the experimental constraints, both exploit the large spread in pixel hits generated from the electron shower. A pixel-clustering algorithm is used that scans over the entire chip, looping over the the array of pixel hits and converting into clusters—if a hit pixel

has any neighbouring hit pixels, these are absorbed into the cluster. The vast majority of clusters consist of 1-pixel clusters, corresponding to the detection of an incident photon. Through the charge-sharing effect described previously, assuming the photocathode is at a high negative potential ($\sim$ 18 kV) then 15 to 20% of incoming photoelectrons will create 2-pixel clusters [43].

Clusters from ion feedback events vary in size but are in general larger than for clusters produced from photoelectrons. A minimum threshold is defined that maximises the identification of true ion feedback electrons yet minimises dilution from fake clusters. The use of fine granularity ALICE-mode runs is ideal for separating the distributions, and a cut of ≥ 5 pixels has been the optimal choice for defining a large (ion feedback) cluster. The resulting ion feedback (IFB) rate takes the proportion of the total recorded clusters (n_{All}) that are defined to be large (n_{Large}):

$$\mathrm{IFB} = n_{Large}/n_{\mathrm{All}} \tag{4.1}$$

$$\delta\mathrm{IFB} = \sqrt{n_{Large}}/n_{\mathrm{All}} \tag{4.2}$$

The ion feedback uncertainty δIFB assumes a poisson distribution.

4.4.3 PDTF Monitoring

Ion feedback is measured as part of the standard test at the PDTF stations. 'Strobe scans' are taken by varying the delay of the LED pulse ($\sim$ 2.5 photons/event) with respect to the data-taking trigger. A 'strobe' refers to a control signal sent to the chip that defines the time-sensitive window of the HPD. While operating in the RICH detectors this window is 25 ns, but in the PDTF a 50 ns window is used so as to absorb signal tails. The strobe scan makes measurements in steps of 5 ns over a 150 ns window. In Figure 4.12, the peak of clusters located at small delay (right side of plot) represents the response to LED light. An ion feedback scan is then performed in steps of 25 ns over a range 0–400 ns. The peak at large delay (left side of plot) delayed in time by 250–300

ns with respect to the signal peak, consists primarily of large clusters (≥ 5 pixels) that have originated from ion feedback. The time delay of the window is tuned to record the maximum ion feedback response, yielding the number of large clusters.

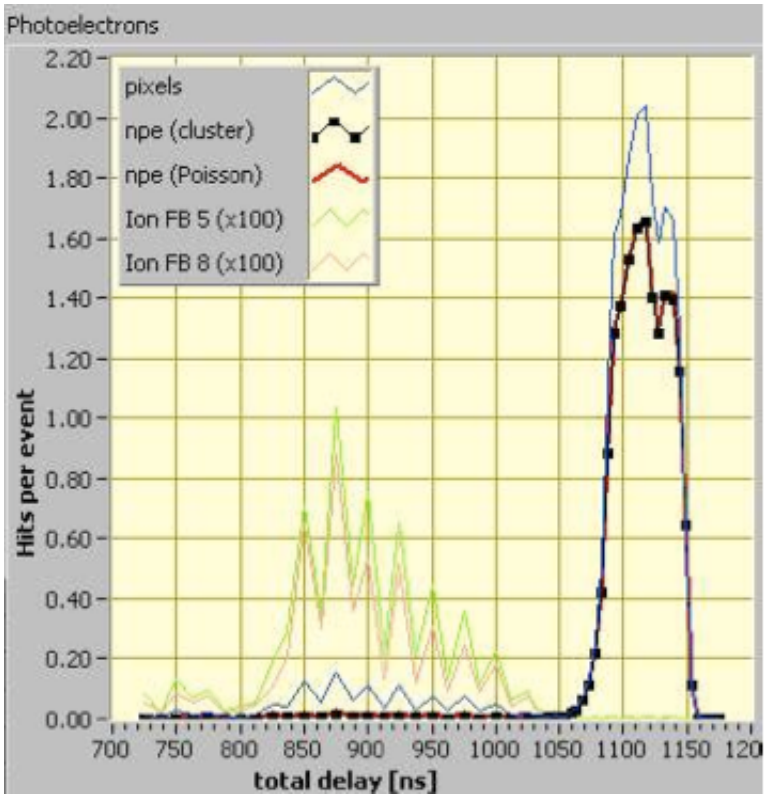

Figure 4.12: Time-dependent response to pulsed LED: "small-cluster" peak on the right due to light; "large-cluster" peak on the left due to ion feedback.

By applying Equations 4.1 and 4.2, an estimate of the absolute ion feedback and its error can be calculated. Newly manufactured HPDs are required to have a measured ion feedback $< 1\%$—all tested HPDs met and surpassed this requirement. The calculated error in ion feedback ranges from 5% to 10%.

4.4.4 RICH Monitoring

Since their inception into the RICH detectors, the HPD panels have been regularly monitored for ion feedback rates. This has required an experimental set-up that is located inside the gas enclosures but outside the LHCb acceptance. The panels are illuminated by light of wavelength 635 nm, generated from a 1 mW

continuous-wave (cw) laser diode located off-detector. The light is attenuated and split into different fibres of length ~ 100 m. At the end of each fibre is a lens that diverges the beam, creating a spread of illumination over the panels.

The laser light causes elevated photoelectron rates, with typically > 3 photoelectrons recorded per HPD trigger. Because of the position of the fibre heads, light is incident at an angle to the panels and the resulting image is partially shadowed by the mu-metal shield of the HPD. Ion feedback clusters cannot be isolated in time (with respect to the HPD trigger), owing to the nature of the laser light. The experiment relies on high statistics to provide an accurate measurement of ion feedback rate.

Ion feedback runs take place when the RICH is in stand-alone mode i.e. during service periods where control of the detector is handed over to the RICH collaboration. The TFC is configured to send triggers to the HPDs (at a rate of a few kHz) while the cw laser is fired. The clustering of pixel hits is performed by Brunel, a reconstruction project based on the "event-by-event" framework Gaudi. A standard ion feedback run is performed in ALICE mode and consists of 3M triggers (events).

The reconstruction stage performs pixel clustering in a way similar to that for the PDTF method. Imposing the standard ≥ 5 pixel cut yields the total number of ion feedback clusters. A significantly degraded vacuum can be observed by eye such as in Figure 4.13; the pixel hit-map contains only ion feedback clusters and shows clearly that electron showers from the ion feedback process are emitted from the centre of the photocathode.

Again, it is only after the ion feedback clusters are normalised with the total clusters (Equations 4.1 and 4.2) can the absolute ion feedback rate be calculated. The majority of HPDs in RICH1 and RICH2 retain an excellent vacuum quality as shown for a particular laser run in March 2010 (Figure 4.14), where 75% of HPDs had a calculated ion feedback of less than 1%.

This distribution though does not describe how the system evolves over time. Results dating back as early as March 2008 were already showing a systematic increase in ion feedback for RICH2 HPDs after comparing two laser runs that were taken ~ 4 months apart. 94 out of the 288 RICH2 HPDs showed an increase of

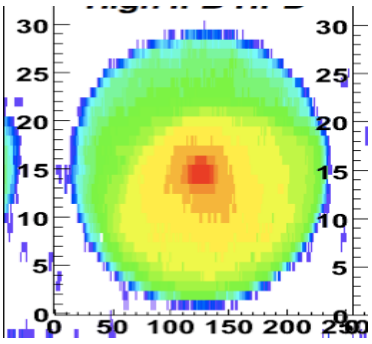

Figure 4.13: Pixel hitmap of HPD under illumination from laser light: clusters from ion feedback concentrate at the centre of the image.

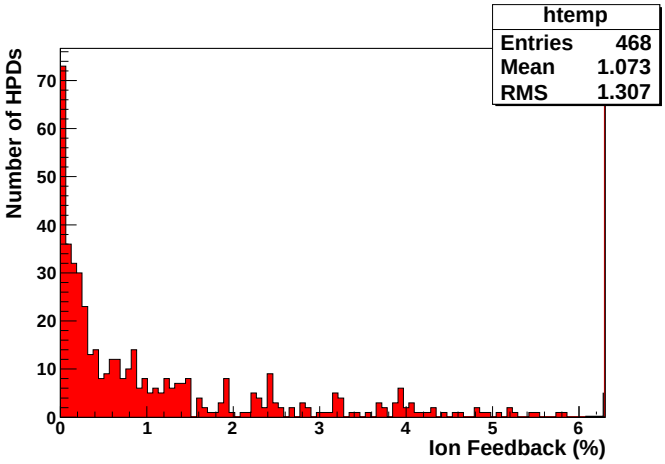

Figure 4.14: Ion feedback distribution for all RICH HPDs, recorded during laser run in March 2010.

nearly +0.15% per month [44]. This signified the importance of using timelines to track the long term development of ion feedback for every HPD in the RICH detectors.

Ion Feedback Timelines

Creating and fitting to timelines have become a powerful tool for predicting the lifetime of HPDs. Data from all ion feedback measurements is collated into one set, including the initial strobescan measurements (denoted IFB_{SS}) and the cw-laser measurements made thereafter (denoted IFB_{CW}). An earlier study has shown that for $IFB_{SS} < 0.3\%$ there is a constant correlation between the two measurements: $IFB_{CW} = 2.5 * IFB_{SS}$. The scaling factor accounts for the fact that during cw-light runs the entire time delay is integrated over when recording large clusters, compared to the strobescan method that triggers only at the peak of ion feedback response. The proportionality factor increases for larger values of IFB_{SS}, where secondary ionisation occurs and is integrated over in cw-light runs only. When combining data this scaling factor is used to convert IFB_{SS} to IFB_{CW}, providing good consistency between the methods.

The change in ion feedback over time is determined by two competing factors: the increase in gas concentration that is intrinsic to each HPD, and an annealing effect

from ionising photoelectrons. The magnitude of this annealing effect depends on how long the HPDs are in an 'active' state i.e. under high voltage ($\sim$ 18 kV) and illumination from the cw-laser. This duration is referred to as an HPD's duty cycle, and varies according to the schedule of each RICH detector. The annealing effect is small and has only been observed in very low ion feedback HPDs such as in Figure 4.15—the cluster of data-points represent a period of high duty cycle in the RICH1 detector; the decrease in ion feedback is thus most likely caused by the annealing effect. During 2008, the duty-cycle of most HPDs remained consistently high as cw-laser runs were performed with regularity (every $\sim$ 2 weeks).

HPDs with a more developed ion feedback retained a linear increase in ion feedback for the periods up to (and including) the end of 2008 as exemplified in Figure 4.16. Throughout 2009, preparations were made for the LHC turn-on, with the focus shifting to time alignment, cosmic runs and global commissioning. This reduced the duty cycle of the HPDs, and an increased linear gradient was observed for $\sim$ 20% of HPDs over this period (second stage of Figure 4.16).

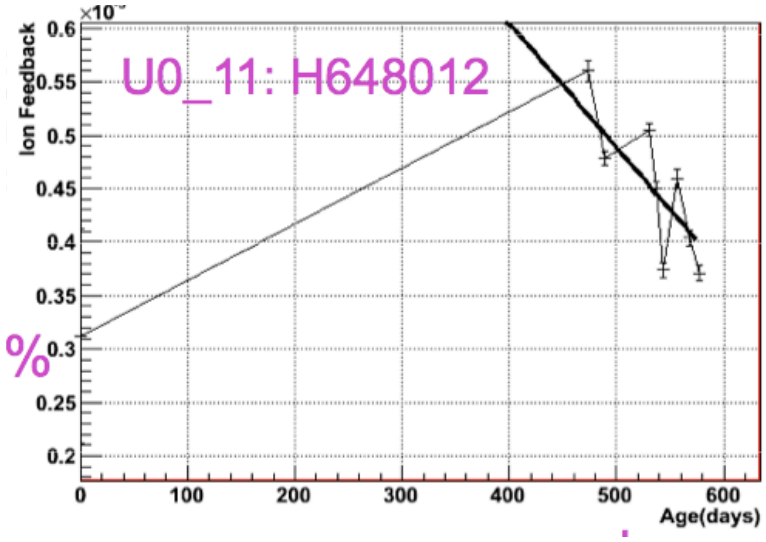

Figure 4.15: Timeline of low ion feedback HPD, displaying characteristics of ion annealing.

Eventually, the vacuum degrades to a point where secondary ionisation occurs, as in Figure 4.17. The initial stage of this process is indicated through elevated ion feedback rates as well as a slight increase in bias current. Finally, the occupancy on the pixel chip increases to a point where the bias current saturates. The

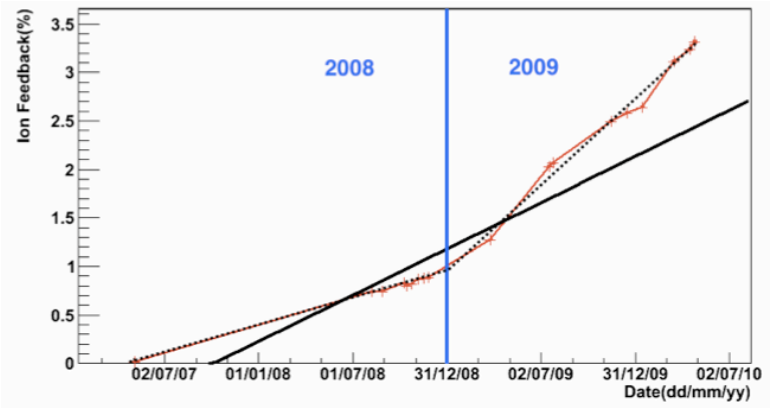

Figure 4.16: Timeline of HPD with developed ion feedback. Increase in vacuum degradation is evident from 2009.

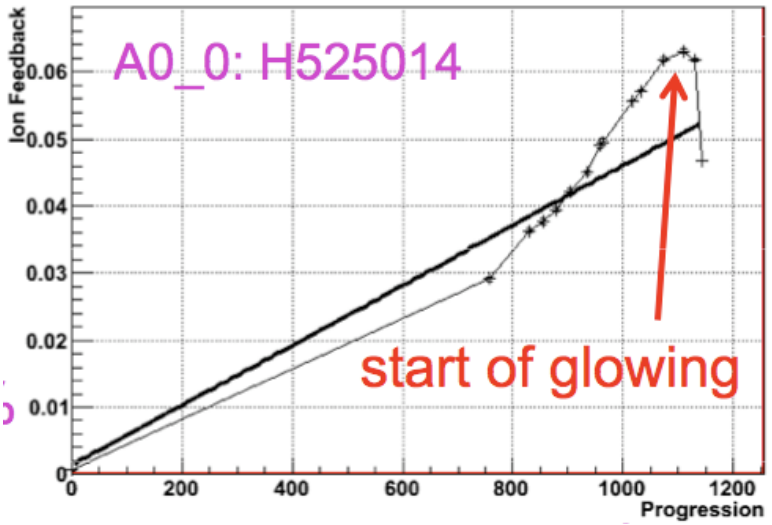

Figure 4.17: Timeline of HPD after entering glowing stage, coinciding with unstable ion feedback measurements.

measured ion feedback is then observed to drop steadily, as the gas concentration gradually diminishes through the annealing process.

There are some cases where the measurement of ion feedback is unreliable. For a minority of HPDs, such as those residing on the lower edge of columns in RICH2, their positions are such that they are outside the cw-light acceptance and receive almost no illumination. This causes an overestimate in the ion feedback rate, similar to that expected for a dark-count measurement. While no clear pattern can be observed in the timeline of these HPDs, the measurement does provide an upper limit of what would be expected if sufficient illumination were provided. Noisy pixels columns, which occur as a result of L0 board configuration errors, contribute "fake" ion feedback clusters that biases the calculated rate as well.

Predicting HPD Lifetime

Ion feedback is strongly related to the onset of glowing in an HPD, as was shown in the previous figure. Almost every HPDs has begun glowing less than 1 year after exceeding the threshold $\mathrm{IFB_{CW}} > 5\%$. By fitting to the timeline and projecting forward in time, a prediction can be made of when $\mathrm{IFB_{CW}}$ is expected to cross this 5% threshold. The decision to replace certain HPDs can be made many months in advance using this information. Despite the dependency of the $\mathrm{IFB_{CW}}$ gradient on the ever-changing duty cycle, on average the increase in ion feedback is best described by a linear fit. Including the PDTF measurement(s) in the fit extends the fit range significantly and makes the predictions more robust. On average, the ion feedback of HPDs increases by +0.5% per year, with larger gradients observed for early batch HPDs residing in RICH2. The fitting predicts that an average of 11 RICH HPDs per year will pass the 5% threshold and become candidates for glowing.

Treatment of bad HPDs

The occurence of glowing renders the HPD useless, and even a hinderance, to the operation of the RICH detectors. Such HPDs are removed as soon as possible and delivered back to the manufacturer for repair. Bake-outs are a common method of repair, whereby the HPD is placed in a vacuum-sealed box and heated to a

high temperature to accelerate the out-gassing from within the HPD body. There is though a limit to the number of times this can be performed on an HPD before damage occurs to certain components, and sometimes it is necessary to instead construct an entirely new HPD. As with the original batches, all new and repaired HPDs are first sent to Edinburgh for individual testing.

The imposing schedule of the LHC limits the access to the RICH detectors to, on average, every few months. Additionally, the demand for new HPDs often outweighed the supply, and it was during these times that I was responsible for prioritising replacements. The deciding factors lie not only in the glow-risk of an HPD but also its impact on physics data-taking. As shown previously in Figures 4.10 and 4.11, the Cherenkov photon occupancies are highest at the centre of the panels, and the presence of HPDs with a low glow risk here is crucial.

Extensive tests have been performed to locate the source of the leaked gas inside the HPD body. The bias current response to the photocathode voltage has been measured to have a dependency that is characteristic of light ions such as helium or hydrogen [45]. Spectroscopic studies of light emitted from within an HPD with severely degraded vacuum have revealed peaks also consistent with hydrogen ions [46]. The most popular explanation has been of water molecules deposited in one of the internal components during assembly of the HPD, resulting in the release of hydrogen ions.

4.4.5 Preparations for Physics Data-Taking

The LHC schedule will also dictate the opportunities to perform dedicated cw-laser runs. This has driven the necessity to monitor ion feedback while the LHC is in operation, by using Cherenkov photons from beam collisions. Key to this study is to maintain a consistency in results between this method and the laser runs. One of the main differences lies in the readout modes: while dedicated laser runs can afford to run in the high granularity ALICE mode, the processing of physics data with such a high number of channels (8192 per chip) is unfeasible, and is instead performed with 8-pixel grouping referred to as PHYSICS mode. This study made use of the vast number of ALICE and PHYSICS cw-laser runs to extract a correlation in measured ion feedback between the two modes. Results

are presented below.

Correlation in Re-Clustered ALICE Data

Re-clustering an ALICE run is an effective way to make a correlation, because it allows the comparison to be made over the exact same events. The reconstruction software is updated so that it manually performs the clustering on a PHYSICS (32×32 pixel) array, regardless of whether the run was configured in ALICE mode or not. The study accumulates data taken from 10 RICH2 laser runs that span approximately 1 year, in each case reconstructing the same 3M events in the normal ALICE mode and re-clustered PHYSICS mode. Figure 4.18 shows 4 ion feedback timelines, representing the re-clustered rates $\text{IFB}_{\text{PHYSICS}}$ with 3 different pixel thresholds applied (≥ 3, ≥ 4, ≥ 5) along with the ALICE-clustered rate $\text{IFB}_{\text{ALICE}}$ with the well known ≥ 5 threshold applied. This figure, as well as Figure 4.19 that shows a direct comparison of all analysed HPDs, clearly shows that a cut of ≥ 4 for $\text{IFB}_{\text{PHYSICS}}$ provides the best 1-to-1 correlation with $\text{IFB}_{\text{ALICE}}$.

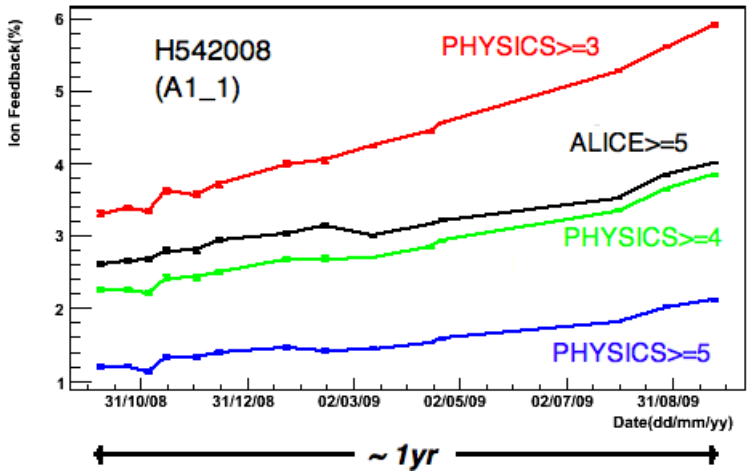

Figure 4.18: Example ion feedback timeline from 10 RICH2 data-runs, recorded in ALICE mode and also re-clustered in PHYSICS mode.

In general, $\text{IFB}_{\text{PHYSICS}}$ (≥ 4) slightly underestimates the corresponding $\text{IFB}_{\text{ALICE}}$ measurement, but also has a quadratic dependence as shown in the previous figure. This could be explained by an increase in fake ion feedback clusters at large $\text{IFB}_{\text{ALICE}}$ as a result of secondary ionisation.

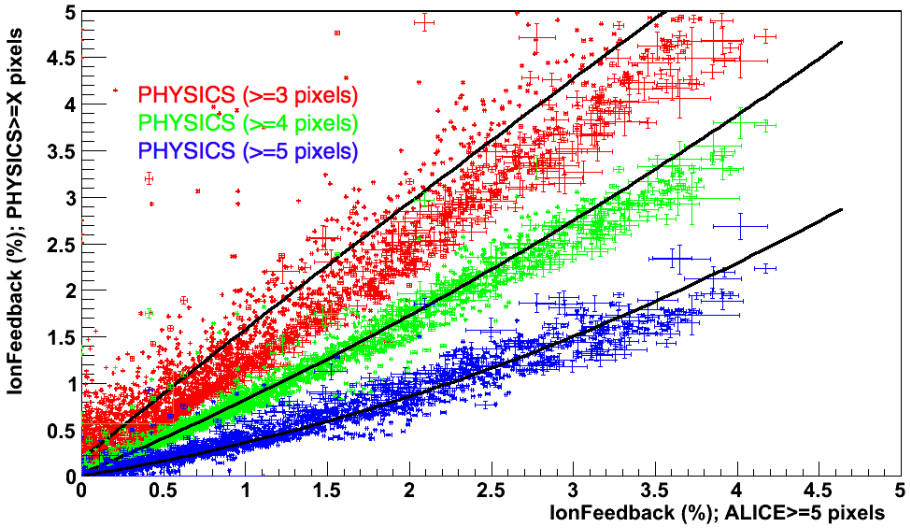

Figure 4.19: Accumulated data (all HPDs) from 10 RICH2 data-runs, recorded in ALICE mode and also re-clustered in PHYSICS mode.

Correlation in ALICE vs. PHYSICS Data

The previous results were then confirmed by analysing separate cw-laser runs—one ALICE and one PHYSICS run—and comparing ion feedback rates. The time lapse of each pair of runs was required to be less than a day, so as to minimise the effect of evolving conditions such as HV stability or vacuum degradation. Such run pairs were recording data for both RICH1 and RICH2 simultaneously, providing increased statistics. The results are presented in the same format as in the previous section, with $\mathrm{IFB}_{\mathrm{PHYSICS}}$ evaluated with thresholds (≥ 3, ≥ 4, ≥ 5 pixels) and compared against $\mathrm{IFB}_{\mathrm{ALICE}}$ with threshold ≥ 5 pixels. Again a cut of ≥ 4 pixels for $\mathrm{IFB}_{\mathrm{PHYSICS}}$ provides the best 1-to-1 correlation, giving a slightly underestimated yet quadratic dependence on $\mathrm{IFB}_{\mathrm{ALICE}}$ as exemplified in Figure 4.20.

In total, 4 pairs of runs were analysed. A number of HPDs (circled in Figure 4.20) consistently showed diverging ion feedback rates $\mathrm{IFB}_{\mathrm{PHYSICS}} >> \mathrm{IFB}_{\mathrm{ALICE}}$. This can be explained by high occupancy in areas of the photocathode, most likely as a result of reflection, which create fake ion feedback clusters in the chip. These high occupancy areas are depicted in a "large" cluster hit-map of RICH1 (Figure 4.21), with the same problem HPDs circled in black. For the purposes of this analysis these HPDs can be removed by applying an arbitrary limit of < 7

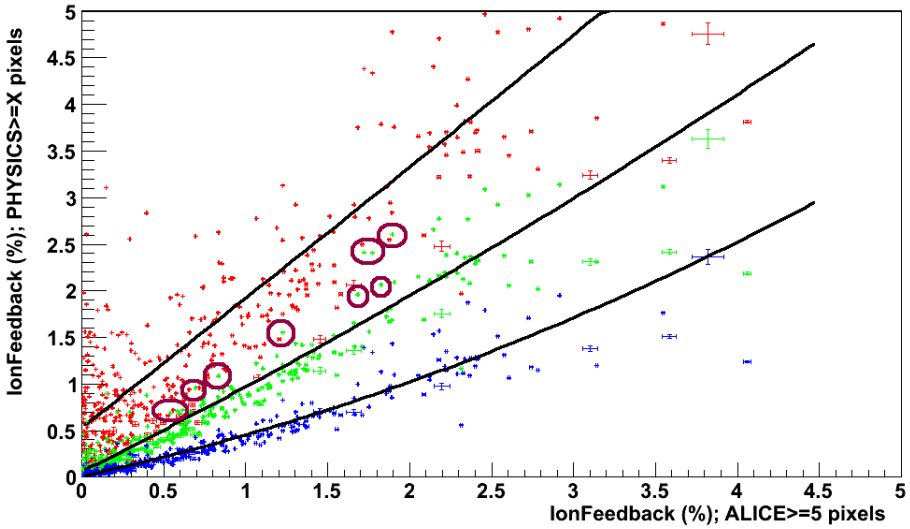

Figure 4.20: ALICE/PHYSICS run pairs: ion feedback comparison for one run. High $\mathrm{IFB}_{\mathrm{PHYSICS}}$ deviations are circled in red.

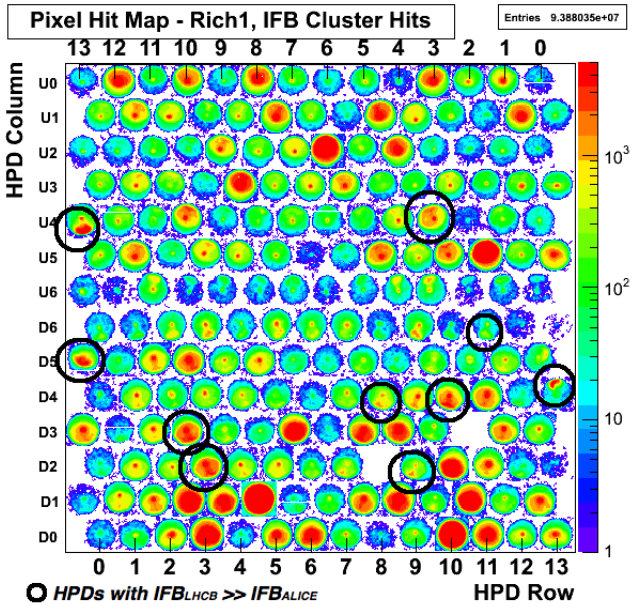

Figure 4.21: ALICE/PHYSICS run pairs: large cluster hit-map for one run. High $\mathrm{IFB}_{\mathrm{PHYSICS}}$ deviations are circled in black.

total clusters per event, which is equivalent to a limit on pixel occupancy. The removal of these outliers helps to improve the quadratic fit.

Summary table

The quadratic fit coefficients for $\mathrm{IFB_{PHYSICS}}$ (≥ 4 pixels) vs. $\mathrm{IFB_{ALICE}}$ (≥ 5 pixels) from all the mentioned data-sets are summarised in Table 4.1 below. The consistency in results is much better than expected. A deviation is present between datasets (1,2) and (3,4,5)—this was confirmed to be due to differing results for $\mathrm{IFB_{PHYSICS}}$ at large values of $\mathrm{IFB_{ALICE}}$[1]. This is an on-going investigation, and the analysis of more data-sets should provide more information on the coefficients that best describe the relationship between $\mathrm{IFB_{PHYSICS}}$ and $\mathrm{IFB_{ALICE}}$.

Dataset	Run-Type	x_0	x_1	x_2
1	RICH2 Re-Clustered	0.02	0.75	0.04
2	17th March (68243/68250)	0.03	0.74	0.08
3	16th April (70243/70250)	0.04	0.85	0.04
4	26th April (70743/70747)	0.04	0.86	0.02
5	20th May (72090/72075)	0.03	0.84	0.03

Table 4.1: Quadratic fit coefficients x_n, describing the relationship between $\mathrm{IFB_{PHYSICS}}$ at ≥ 4 pixels and $\mathrm{IFB_{ALICE}}$ at ≥ 5 pixels.

The next step in the preparation for physics data-taking involves an off-line analysis of the clustering code on beam collision data. The ability to detect ion feedback clusters, which would be delayed by 250–300 ns with respect to the Cherenkov photons, depends on the bunch structure of the LHC beam. Understanding the timing is essential before any measurement of ion feedback can be made. Once this has been fully tested the software can then be the integrated into the online reconstruction project and begin monitoring HPDs.

[1] After re-fitting with a constrained range of $0 < \mathrm{IFB_{ALICE}} < 1\%$, the fit parameters for all 5 data-sets converged.

4.5 Summary

The RICH detectors of LHCb require photon detection with high single-photon sensitivity in the Cherenkov spectrum and fast readout time. The hybrid photon detector (HPD) fulfils this criteria, and since their inception into the RICH detectors in 2007-2008 the HPDs have been performing well. Immediately after manufacture, HPDs are shipped to Edinburgh for extensive testing. All components of the HPD are tested thoroughly, with the majority of HPDs passing and even exceeding the design specifications.

After installation in the RICH detectors, HPDs are subject to further tests to ensure an optimal operation during pp collisions. Illumination with pulsed laser light allows the timing of HPDs to be tuned to achieve the maximum response.

The lifetime of an HPD is limited by vacuum degradation. Residual gas atoms in the HPD body are ionised by a high-energy photoelectron, resulting in the emission of multiple electrons from the photocathode. This process is known as ion feedback, and can be induced for any HPD under high voltage and illumination. Post-production tests at the Edinburgh facility showed that the majority of HPDs retained an excellent vacuum quality, with low measured ion feedback rates ($< 1\%$). However, further tests at the RICH detectors confirmed a systematic increase in ion feedback over time, albeit with varying gradients. The increase in ion feedback is generally linear, with an additional dependency on the frequency and duration of the laser runs themselves.

Vacuum degradation eventually reaches a critical point where ion feedback becomes self-sustaining, saturating the silicon chip and therefore rendering the HPD unfit for use in the RICH detectors. This consistently occurs for HPDs with high ion feedback ($> 5\%$), and decisions on the riskiest of HPDs can be made many months in advance. Work is on-going with the manufacturers to arrange for the regular repair of these HPDs.

Collision data can be used as an alternative to continuous-wave laser light, to induce and measure ion feedback in the RICH HPDs. A preliminary study has looked into the effect of changing the read-out granularity from ALICE mode (256×32) to PHYSICS (32×32) mode. Using a number of re-clustered ALICE runs, as well as ALICE/PHYSICS run pairs, a pixel threshold of ≥ 4 PHYSICS

pixels is most correlated with the current threshold of ≥ 5 ALICE pixels for laser runs.

Chapter 5

Mechanisms for $B^{\pm}$ production

The rest of this thesis describes an analysis of the $B^{\pm}$ cross-section and asymmetry at LHCb, using $B^{\pm} \to J/\psi K^{\pm}$ decays. Cross-section measurements are a powerful test of theoretical models, and are an integral part of many physics measurements at a high-energy collider. Production and detection asymmetries are a necessary factor to take into account when performing CP violation measurements of B-decays and D-decays at LHCb.

The chapter begins with the phenomenology of $B^{\pm}$ production at a hadronic collider, from the initial hard scattering of the protons constituents to the hadronisation of the b quarks. The strategy for a $B^{\pm}$ production measurement at LHCb is then detailed, including previous measurements performed at other detectors. Finally, the strategy for a $B^{\pm}$ asymmetry measurement is given, beginning with the various mechanisms that contribute to the measured value.

5.1 Phenomenology of $B^{\pm}$ production

5.1.1 B-Production at a Hadronic Collider

There are a number of ways in which a b-quark pair can be produced from a pp collision at the LHC. Gluon fusion is a hard scattering processes that can produce a $b\bar{b}$ pair directly, and is the dominant process is $b\bar{b}$ production. *Flavour excitation* refers to an alternative case where the b quark from the sea of one

proton can scatter through a hard interaction with a parton from the other proton - to preserve bottom quark number, a second b quark is generated as part of the additional activity in the event. *Gluon splitting* provides another indirect contribution where the $b\bar{b}$ pair is produced from a gluon after the hard scattering, as a part of the fragmentation process of the event. The Feynman diagrams for these contributions, at leading order, are shown in Figure 5.1.

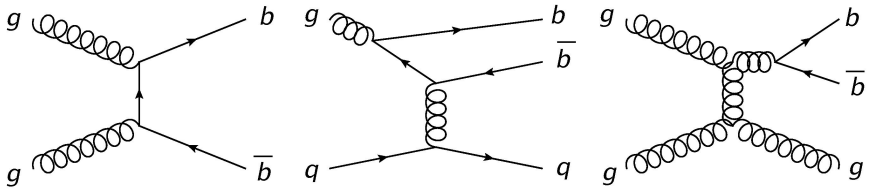

Figure 5.1: b-quark production mechanisms at leading order: (left) gluon fusion; (middle) flavour excitation; (right) gluon splitting.

Once the b and $\bar{b}$ quarks are produced, they radiate secondary gluons by strong interaction. This process is described by QCD and can be calculated perturbatively, due to the high energy scale, which implies $\alpha_s << 1$ [47]. this part of the process is the *perturbative QCD part of the fragmentation*. It is calculable either by theoretical QCD computations or using Monte Carlo generators, as will be described in this chapter.

When the b and $\bar{b}$ quarks separate, the energy scale diminishes and the color interaction between the two quarks becomes stronger. Through the self-interaction of gluons, a region of energy density builds between the quarks. At some point, the increasing potential energy is sufficient to create from the vacuum another $q\bar{q}$ pair despite the penalty of providing the extra $q\bar{q}$ mass, and the system then splits into two colour-singlets. The process repeats until clusters of quarks and gluons are formed, having zero net colour and internal momentum. Consequently, the colour coupling inside the clusters is very strong and turns them into hadrons, a process referred to as *hadronisation*. This part of the fragmentation process involves non-perturbative QCD, and brings difficulties when performing theoretical calculations. Various phenomenological models have been implemented to provide approximate solutions.

5.1.2 Perturbative QCD processes

Quantum Chromodynamics (QCD) is the theory of the strong interaction, the binding force that keeps elementary particles, called quarks, confined in hadrons. The strong interactions are invariant under transformations in an internal colour space, which gives rise to 3 conserved colour states. QCD has two important properties related to the energy-scale dependence of the coupling strength, called confinement and asymptotic freedom. Confinement is the property that no isolated coloured charge can exist as a free particle but only colour singlet particles can be isolated. All observed hadrons, which exist as a 3-quark state (baryon) or as a quark-anitquark pair (meson), are colourless in nature. Asymptotic freedom is the property that QCD coupling is weak at high energies, so that the theoretical predictions can be expressed as an expansion in powers of the coupling limited to the first few terms. This perturbative approach to QCD has proven to be very useful when applied to high-energy hadronic collisions, as is described below.

Perturbative QCD can be most simply applied to the calculation of hadronic cross-sections in electron-positron annihilation. The perturbative approach treats the high momentum scattering independent from the low-momentum hadronisation stage. The *total* hadronic cross-section (i.e. summed over all possible hadron final-states) can be factorised into a term describing the hard scattering cross-section, and a term describing the resulting hadronisation (that we are not interested in). At the lowest-order (LO) in the hard scattering:

$$\sigma(\mathrm{e^+e^-} \to \text{hadrons}) = \sigma_0(\mathrm{e^+e^-} \to \mathrm{q\bar{q}}) \tag{5.1}$$

Most common factors cancel in the ratio of the hadronic cross-section (summed over all possible final-states) to the cross-section for $\mu^+\mu^-$ production. At a certain energy scale Q, this ratio is measured to be $\propto N_c \sum_f q_f^2$, with $N_c = 3$ colours and q_f^2 the (conventional) charge of the quark flavour accessible at Q ($m_f < Q$). The factorisation theorem has important implications for the perturbative treatment of the hard scattering cross-section, which is required to be safe from long-distance (soft/collinear gluon) emission.

Deep inelastic scattering (DIS) refers to the more complicated process of high energy lepton-hadron collisions. DIS experiments have become a breakthrough for the establishment of Feynman's parton model, with the hadron no longer considered a fundamental particle but a composite consisting of quarks and gluons (collectively referred to as partons). In 1969 Bjorken proposed that for a DIS process with $Q^2 \to \infty$, the scattering cross-sections are dependent not on the squared momentum transfer q^2 but on the (Bjorken) scale factor $x = Q^2/2M\nu$, where M is the target nucleon mass and ν is the energy loss of the scattered lepton. This was experimentally verified by SLAC-MIT with electron-proton scattering, and had important implications in proving the point-like nature of the partons.

The scaling factor x is equivalent to the momentum fraction ($0 < x < 1$) carried by the parton, with respect to the proton. DIS cross-section measurements exploit this x-dependence to extract a probability function, or *Parton Distribution Function* (PDF), of x-distributions for different parton types. PDFs are an essential tool for cross-section calculations of partonic collisions. The H1 and ZEUS experiments have measured DIS at $Q^2 = 10$ GeV^2, using 100 pb^{-1} of e$^+$p data and $\sim$ 15 pb $^{-1}$ of e$^-$p data respectively [48]. The combined cross-section data have been used as the sole input for a QCD fit to to extract the PDFs of the proton, as shown in Figure 5.2. The figure shows a peak in the large-x region for u_v and d_v valence quark contributions, the partons most regularly associated with the proton sub-structure. In addition there is a large (scaled down) small-x contribution from gluons and from sea quark pairs. Sea quark pairs ($u\bar{u}, d\bar{d}, c\bar{c}, s\bar{s}, b\bar{b}$...) result from fluctuations in the proton, and an infinite number of pairs can be created as long as they have very low momentum, due to momentum conservation in the proton.

Hadronic (pp) collisions at the LHC can be factorised into a component describing the hard (perturbative) scattering process $\hat{\sigma}(x_1, x_2, s, \mu_f^2)$ and a low-energy (non-perturbative) component describing the PDFs $f(x, \mu_f^2)$ of the partons P_1 and P_2 in the proton, as shown below:

$$\sigma = \int dx_1 dx_2 f_1^{P_1}(x_1, \mu_f^2) f_2^{P_2}(x_2, \mu_f^2) \hat{\sigma}(x_1, x_2, s, \mu_f^2) \tag{5.2}$$

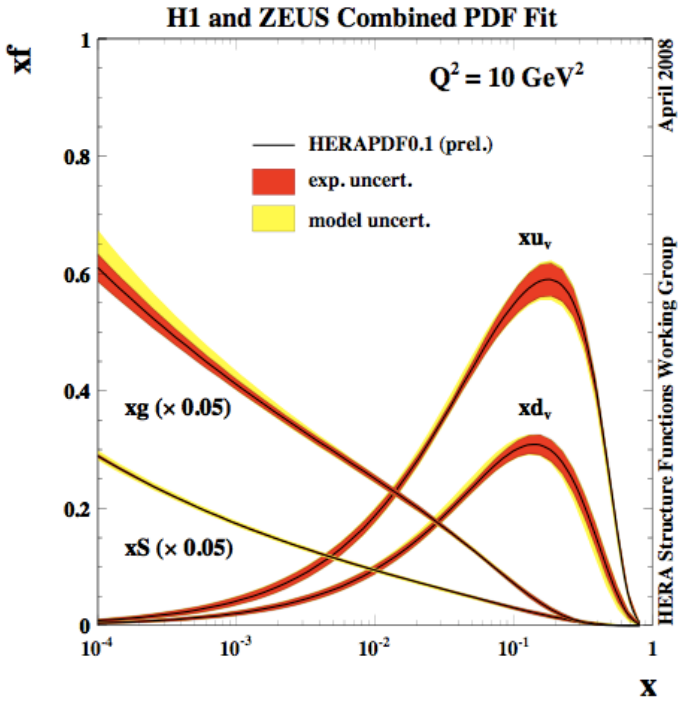

Figure 5.2: PDF fits to combined DIS data taken at HERA and ZEUS [48]: $x\mathrm{d}_v$ (down quark valence), $x\mathrm{u}_v$ (up quark valence), $x\mathrm{S}$ (total sea-quark contributions and $x\mathrm{g}$ (gluon).

Factorisation of the long and short distance terms absorbs all infrared divergences into the bare PDF, and both PDF and hard scattering terms acquire a factorisation scale dependence μ_f. Renormalisation of the bare strong coupling α_s is required to absorb all short-time physics (i.e. loop fluctuations), and the renormalised coupling acquires a scale dependence μ_r. At LO this dependence on theoretical conventions brings large uncertainties in the prediction of cross-sections. The application of next-to-leading order (NLO) corrections (at the order α_s^3) to the hard process has proven essential for minimising this scale dependence.

The $\mathrm{b\bar{b}}$ production cross section can be predicted using perturbative QCD. Theoretical QCD calculations exist at the next-to-leading-order (NLO) accuracy, and account for all terms at a fixed order (FO) to $\mathcal{O}(\alpha_s^3)$ [47]. For values of p_{T} much larger than the b-quark mass, large logarithms of the ratio $p_{\mathrm{T}}/m_{\mathrm{b}}$ arise in the coefficients of the perturbative expansion. Techniques are available to resum the leading and next-to-leading class of logarithms (NLL) to remove these divergences [49]. The total and differential $\mathrm{B}^{\pm}$ cross-section presented in Chapter 7 is performed at FO, with NLL summation of terms. These QCD predictions are affected by large theoretical uncertainties such as the dependence on the choice of the renormalization and factorization scales and the b-quark mass. The non-perturbative aspect is described by the Peterson Model [50], which relies on simple kinematical arguments to derive a fragmentation function in terms of the parameter $\epsilon = \frac{m_u}{m_b}$.

5.1.3 Monte Carlo methods

The use of matrix element calculations to describe the evolution of parton showers, though having the potential to provide an exact cross-section of final states, becomes increasingly complex at higher-orders of α_s, where loop corrections are required to absorb divergences [51].

The MC generator Pythia [51] uses a process that approximates the parton shower in order of dominant contributions. These dominant contributions are associated with collinear ($\theta \to 0$) parton splitting[1] and soft (low-energy) gluon emission[2].

[1] of type $\mathrm{g} \to \mathrm{q\bar{q}}$, $\mathrm{g} \to \mathrm{gg}$
[2] of type $\mathrm{q} \to \mathrm{qg}$

The process is governed by the DGLAP [52, 53, 54] equations that evolve the partons down to a cut-off energy of $\sim$ 1 GeV, where the non-perturbative regime is approached. From here the products are submitted to confinement and hadronisation models.

At this stage in the process, perturbative calculations break down and the event generators employ their own models to describe the formation of hadrons. In the Lund string fragmentation model developed in Pythia, the colour confinement field between a quark and an anti-quark is squeezed into a tube-like region, corresponding to a linear confinement potential. A simplified diagram of this process is shown in Figure 5.3. Further fragmentation can occur only if the invariant mass of the string is large enough to break the string, producing a new $q\bar{q}$ pair in the process. If not then the string decays into either one or two hadrons, depending on the mass of the string [51]. The sensitivity of the Lund model to predict production asymmetries of the $B^{\pm}$ will be revisited in Sec. 6.2.1.

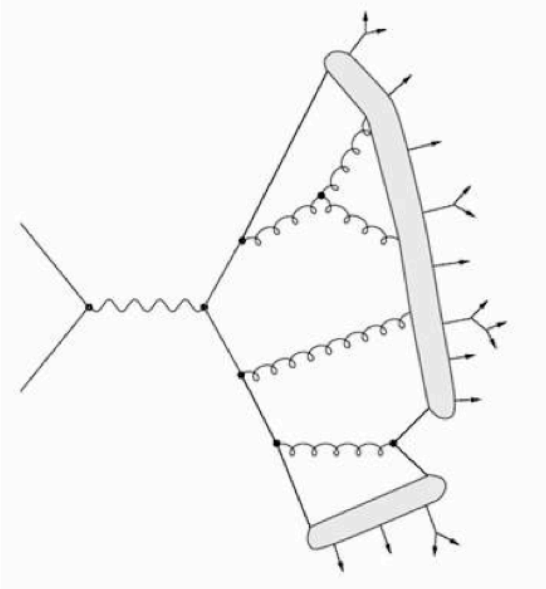

Figure 5.3: The Lund string model applies a colour-confinement string, which stretches between a quark/anti-quark pair. Gluons appear as kinks in the string.

5.2 Measurements of B-hadron cross-sections

5.2.1 CDF and D0 experiments

The CDF [55] experiment at the Fermilab Tevatron have analysed $B^{\pm} \rightarrow J/\psi K^{\pm}$ decays using $p\bar{p}$ collisions at $\sqrt{s} = 1.8$ TeV and 1.96 TeV. The resulting $B^{\pm}$ cross-sections are in good agreement with the FONLL prediction, which uses a fragmentation fraction $f_u = 0.389$ and CTEQ6M fits to the PDFs [56]. The differential cross-section for $B^{\pm}$ are shown in Figure 5.4.

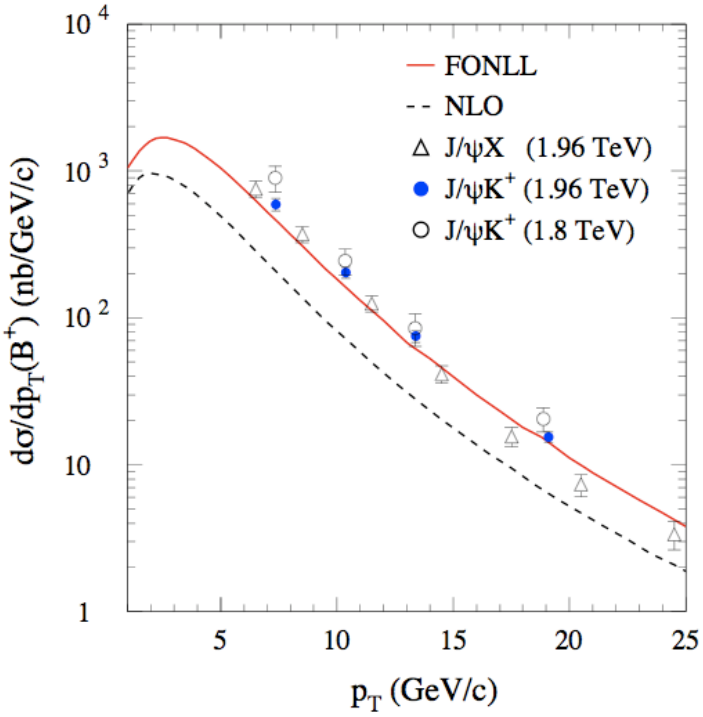

Figure 5.4: Measurements of the $B^{\pm}$ differential cross section ($|y^{B^{\pm}}| \neq 1$) at the Tevatron are compared to the NLO and FONNL theoretical predictions.

5.2.2 The CMS experiment

The CMS experiment operating at the LHC measured the total and differential cross-sections for $B^{\pm}$ hadrons produced in pp collisions at $\sqrt{s} = 7$ TeV [57] using $B^{\pm} \rightarrow J/\psi K^{\pm}$ decays. The total cross section for $p_T^{B^{\pm}} > 5$ GeV and $|y^{B^{\pm}}| < 2.4$

was measured to be 28.1 ± 2.4 ± 2.0 ± 3.1 μb, a factor of 1.5 greater than the Monte Carlo prediction at Next-To-Leading Order (NLO) [57]. The $d\sigma/dp_{\mathrm{T}}$ differential cross section is shown in Figure 5.5.

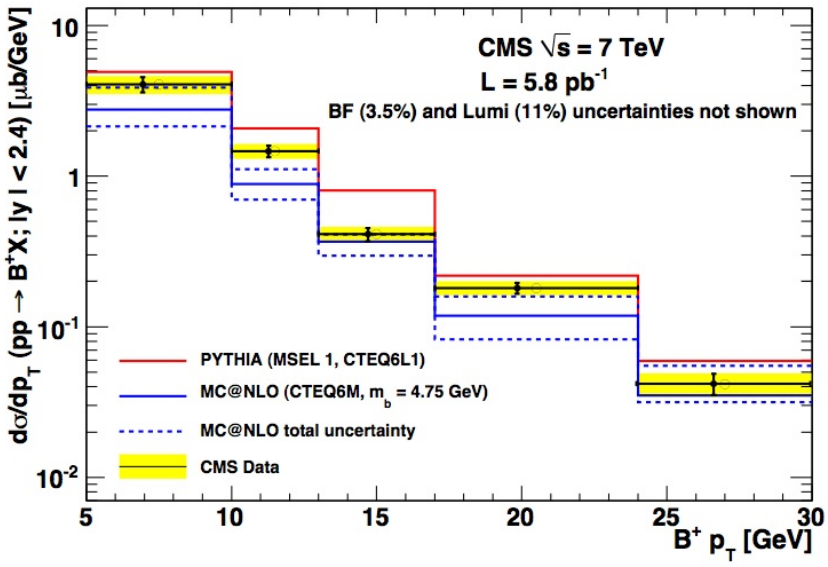

Figure 5.5: Measured differential $B^{\pm}$ cross section $d\sigma/dp_{\mathrm{T}}$ with theory included as a comparison. The error bars are the statistical uncertainties, while the yellow band represents the sum in quadrature of statistical and systematic uncertainties, excluding the common branching fraction and luminosity uncertainties. The solid and dashed blue lines are the MC@NLO prediciton and its uncertainty, respectively. The solid red line is the PYTHIA prediction.

5.2.3 The LHCb experiment

A measurement of the $b\bar{b}$ production cross-section has been performed [58] at LHCb using the first data collected in 2010, at a centre-of-mass energy 7 TeV. Two independent data samples were analysed, recorded at different times and with different trigger thresholds. Events are selected containing the decay chain $b \rightarrow D^0 X \mu^- \nu$, where $D^0 \rightarrow K^- \pi^+$. The selection exploits the finite lifetime of the B hadron to isolate D^0 (from B-hadron) candidates from prompt D^0 candidates. Particle identification of the $D^0 \rightarrow K^- \pi^+$ products is achieved with the RICH system. The data give good agreement to an FONLL prediction of the cross-section, which uses the CTEQ 6.5 [59] fit to the PDF, and to the MCFM [60]

Monte Carlo prediction. The cross-section to produce b-flavoured hadrons was measured in the pseudorapidity interval $2 < \eta < 6$ over the entire range of p_{T}, giving an integrated cross-section:

$$\sigma(\mathrm{pp} \to \mathrm{H_b X}) = (75.3 \pm 5.4(stat.) \pm 13.0(sys.))\mu\mathrm{b} \tag{5.3}$$

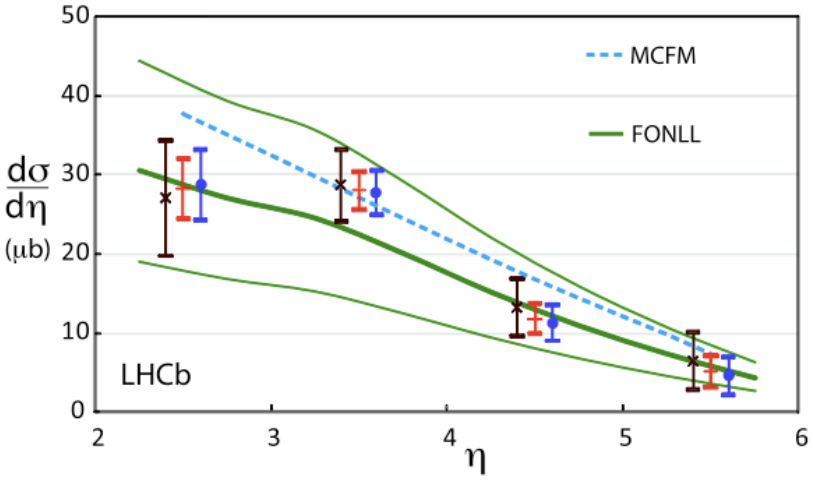

Figure 5.6: $\sigma(\mathrm{pp} \to \mathrm{H_b X})$ as a function of η for the microbias ($\times$) and triggered ($\bullet$) samples, shown displaced from the centre and the average ($+$). The data are shown as points with error bars, the MCFM prediction as a dashed line, and the FONLL prediction as a thick solid line, with associated uncertainty band.

Precise knowledge of the B-hadron fragmentation fractions is vital for absolute branching fraction measurements. This measurement has been performed using collision data at LHCb, which looks for partially reconstructed $\mathrm{B} \to \mathrm{DX}\mu\nu$ decays. The B-hadrons (B_s, B_d, B_u and Λ_b) all decay into mixtures of D-hadron states (D_s, D_d, D_u and Λ_c), and an extraction of the corrected yields is performed using a knowledge of the B-decay and D-decay branching fractions. The relative abundance of strange B_s to light neutral B_d mesons, $f_{\mathrm{s}}/f_{\mathrm{d}}$, is measured to be:

$$f_{\mathrm{s}}/f_{\mathrm{d}} = 0.253 \pm 0.017 \pm 0.017 \pm 0.020 \tag{5.4}$$

The uncertainties associated to the measurement are statistical, systematic and theoretical respectively. The result is in good agreement with the values determined at LEP and Tevatron [61]. The relative abundance of Λ_b baryons to the sum of light (B_d + B_u) mesons, $f_{\lambda_b}/(f_u + f_d)$, shows a p_T^B-dependence:

$$f_{\lambda_b}/(f_u + f_d) = (0.404 \pm 0.017(\text{stat}) \pm 0.027(\text{syst}) \pm 0.105(\text{Br})) \times[1 - (0.031 \pm 0.004(\text{stat}) \pm 0.003(\text{syst})) \times p_T(GeV)] \quad (5.5)$$

This may reconcile the differing results obtained at CDF and LEP, which obtain a ratio of $f_{\lambda_b}/(f_u+f_d) = 0.112 \pm 0.031$ ($<p_T> \approx 40$ GeV/c) and $0.281 \pm 0.012^{+0.129}_{-0.103}$ ($<p_T> \approx 14$ GeV/c) respectively.

5.2.4 $B^{\pm}$ cross-section analysis strategy

This thesis presents a measurement of the $B^{\pm}$ cross-section using $B^{\pm} \rightarrow J/\psi K^{\pm}$ decays, where $J/\psi \rightarrow \mu\mu$. The cross-section is analysed using pp collisions recorded in October 2010, at a centre-of-mass energy of $\sqrt{s} = 7$ TeV. Differential and integrated cross-sections are presented, spanning the fiducial region $2 < y^B < 4.5$ and $0 < p_T^B < 20$ GeV where p_T^B and y^B are the transverse momentum and rapidity ($y = \frac{1}{2}\ln\frac{E+p_z}{E-p_z}$) of the $B^{\pm}$ respectively. The study uses some of the techniques employed in Ref. [62], which performs a measurement of the ratio $\sigma_{B_u}/\sigma_{B_c}$ using $B^{\pm} \rightarrow J/\psi K^{\pm}$ and $B_c \rightarrow J/\psi\pi^{\pm}$ decays.

$B^{\pm} \rightarrow J/\psi K^{\pm}$ is a flavour-specific decay, mediated by a charged $W^{\pm}$ boson. The decay is dominated by the tree-level amplitude, with smaller annihilation and penguin amplitudes contributing to give a small CP-asymmetry (0.009 ± 0.008 from [5]). Feynman diagrams for these 3 processes are shown in Figure 5.7. $B^{\pm} \rightarrow J/\psi K^{\pm}$ is an ideal channel for a cross-section measurement, given the dominant branching fraction ([1.014 ± 0.034]% from [5]). In addition, the J/ψ mass, (3096.916 ± 0.011) MeV/c^2 [5], is an effective parameter for rejection of combinatorial background.

The $B^{\pm}$ differential cross-section is extracted as defined below:

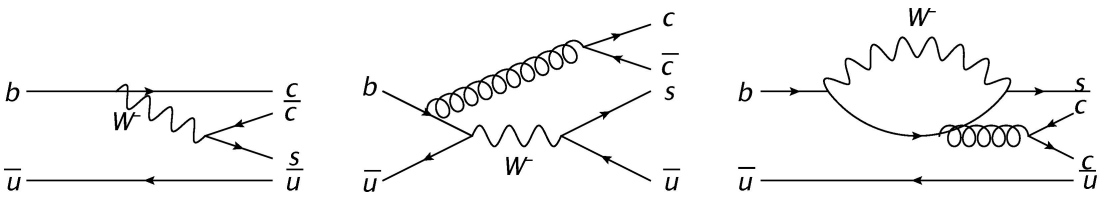

Figure 5.7: Tree-level (left), annihilation (middle) and penguin (right) decay processes for $\mathrm{B}^{\pm} \to \mathrm{J}/\psi\mathrm{K}^{\pm}$.

$$\frac{d\sigma}{dp_{\mathrm{T}}^{\mathrm{B}}} = \frac{N_{B^{\pm}}(p_{\mathrm{T}}^{\mathrm{B}})}{\mathcal{L} \cdot \epsilon_{tot}(p_{\mathrm{T}}^{\mathrm{B}}) \cdot \mathcal{B}(\mathrm{B}^{\pm} \to \mathrm{J}/\psi\mathrm{K}^{\pm}) \cdot \mathcal{B}(\mathrm{J}/\psi \to \mu^{+}\mu^{-}) \cdot \Delta(p_{\mathrm{T}}^{\mathrm{B}})} \tag{5.6}$$

The parameter $\epsilon_{tot}(p_{\mathrm{T}}^{\mathrm{B}}, y^{\mathrm{B}})$ is the total efficiency of $\mathrm{B}^{\pm} \to \mathrm{J}/\psi\mathrm{K}^{\pm}$ including acceptance, reconstruction, selection and trigger effects. Chapter 6 details the extraction of $\epsilon_{tot}(p_{\mathrm{T}}^{\mathrm{B}}, y^{\mathrm{B}})$ using MC data. The parameter $N_{\mathrm{B}^{\pm}}$ is the signal yield extracted from $\mathcal{L}$ of data, where $\mathcal{L}$ is the integrated luminosity. The method used to extract a signal yield from the 2010 data sample will be described in Chapter 7. The branching fractions are $\mathcal{B}(\mathrm{B}^{\pm} \to \mathrm{J}/\psi\mathrm{K}^{\pm}) = (1.013 \pm 0.034) \times 10^{-3}$ and $\mathcal{B}(\mathrm{J}/\psi \to \mu^{+}\mu^{-}) = (5.93 \pm 0.06)\%$ [5].

5.3 Charge Asymmetry Measurement of $\mathrm{B}^{\pm}$

A main category of systematic uncertainty of CP violation measurements involves the presence of asymmetries induced by the detector and event reconstruction, as well as of B meson production asymmetries arising from primary proton-proton collisions. These possible sources of asymmetry are discussed in more detail in the remainder of this chapter, concluding with a strategy for measuring the production asymmetry of $\mathrm{B}^{\pm}$ mesons at LHCb.

5.3.1 Production Asymmetry

Beam remnants refer to the parts of the proton that are not involved in the hard scattering or initial state radiation emission. Colour confinement demands colour

connection between all constituent partons in the colliding protons. This opens up the possibility of multiple interactions, such as multiple hard scattering, beam remnant interactions with scattered partons and remnant interactions with other remnants.

At the parton level, the generation of b and $\bar{\mathrm{b}}$ quarks is symmetric with the production mechanisms limited to $\mathrm{b\bar{b}}$ pair production (e.g. $\mathrm{g} \rightarrow \mathrm{b\bar{b}}$, $\mathrm{gg} \rightarrow \mathrm{b\bar{b}}$). The LHC is unique in the respect that both colliding beams have 100% charge asymmetry in the valence quarks. In certain regions of phase space it is therefore possible that the $\mathrm{b\bar{b}}$ symmetry is broken by interactions with the remnant valence quarks. LHCb probes processes at high rapidity ($2 < y < 5$) and is expected to be sensitive to this redistribution of b and $\bar{\mathrm{b}}$ content. We call this feature a production asymmetry, a phase space dependent observable in B-hadron production.

As explained in Ref. [63] it is possible to identify three mechanisms that may contribute to a production asymmetry. They are described in the context of possible $\mathrm{B}^{\pm}$ asymmetries:

- Beam drag—The beam remnants, with a high particle content of u and d quarks in particular, are present at the kinematic limit of pseudo-rapidity and at a very low transverse momentum. Therefore whenever a hard-scattered parton is color-connected to an element of the beam remnant, there may be a momentum transfer between the two which can only result in drawing the hard-scattered product towards the beam. Products (B^{+}) with low transverse momentum and high pseudo-rapidity are particularly sensitive to this rapidity shift. This would for example produce an excess of B^{-} compared to B^{+} at high rapidity.

- A more direct mechanism results from the hard scattering of a quark by valence quarks, producing an excess of high p_{T}, high energy B^{+} jets.

- Cluster collapse—this final mechanism is a more extreme example of beam drag, where the hard scattered quarks directly hadronise with the beam remnants or with scattered quarks, providing that the energy of the resultant hadron is too low to decay immediately. This mechanism tends to enhance the production of leading particle types. This may for

example produce an excess of B^+ particles compared to B^- particles, slowly increasing with rapidity.

These competing mechanisms can be experimentally very difficult to disentangle, particularly when attempting a study on entire spectrum of B hadrons. We limit ourselves to the study of production asymmetries in the $B^{\pm}$ particle, as a function of the hadron transverse momentum p_T^B and rapidity y^B.

In the underlying event the unified model adopted by Pythia allows for multiple interactions between the partons in the beam hadrons [64]. The Pythia manual [33] states that: *Each incoming beam particle may leave behind a beam remnant, which does not take active part in the initial-state radiation or hard-scattering process. If nothing else, these remnants need to be put together and colour connected to the rest of the event.* Pythia does not intervene in the color-connection of hard-scattered products to the beam remnants and therefore the underlying event. This will have a large impact on the production asymmetries simulated by the software, particularly in the kinematic regions of LHCb.

Relatively few studies exist on dedicated searches for production asymmetry mechanisms. Their importance manifests as uncertainties in CP asymmetry measurements, particularly at LHCb. In some CP-violation studies the production asymmetry (A_p) is made to cancel, avoiding the need for an explicit measurement. Two (A_p) measurements have so far been performed at LHCb, one for the $B^{\pm}$ meson and one for the B^0 meson, as summarised in Table 5.1. With the level of statistics provided, it is inconclusive whether there is a significant difference in A_p between the B^+ and B^0 mesons.

Particle	A_p	Channel	Year	$\mathcal{L}$ (pb^{-1})
B^+	–0.024 ± 0.013 [65]	$B^{\pm} \to J/\psi K^{\pm}$	2010	37
B^0	0.010 ± 0.013 [66]	$B^0 \to J/\psi K^*$	2011	320

Table 5.1: Existing measurements of B-hadron production asymmetry at LHCb, including the channel and dataset used for the study.

5.3.2 CP asymmetry

The $B^{\pm} \to J/\psi K^{\pm}$ decay has a negligibly small CP asymmetry (0.009 ± 0.008 [5]). The Belle experiment performed a measurement of $A_{CP}(B^{\pm} \to J/\psi K^{\pm})$ [67] using 772×10^6 $b\bar{b}$ pairs produced from the KEKB asymmetric-energy e^+e^- collider at $\sqrt{s} = 10.58$ GeV. A measurement of the kaon detection asymmetry is performed with the decays $D_s^+ \to \phi\pi^+$ ($\phi \to K^+K^-$) and $D^0 \to K^-\pi^+$ decay modes [68]. The measured asymmetries of the above modes can be written as:

$$A_{rec}^{D_s^+} = A_{\varepsilon}^{\pi^{\pm}} \tag{5.7}$$

$$A_{rec}^{D^0} = A_{\varepsilon}^{\pi^{\pm}} + A_{\varepsilon}^{K^{\pm}} \tag{5.8}$$

The $A_{\varepsilon}^{K^{\pm}}$ value is extracted as the difference in the reconstruction asymmetries $A_{rec}^{D_s^+}$ and $A_{rec}^{D^0}$. This is found to be $A_{\varepsilon}^{K^{\pm}} = (-0.43 \pm 0.07 \pm 0.17)\%$, weight-averaged over the region $1.1 < p^K < 2.6$ GeV/c. The first and second uncertainties are statistical uncertainties of the $D^0 \to K^-\pi^+$ signal yield and $A_{rec}^{D_s^+}$ respectively.

5.3.3 Detector Asymmetry

The main material interactions can be classified as either electromagnetic or hadronic, and the effects can range from scattering to complete absorption

The $B^{\pm} \to J/\psi K^{\pm}$ decay is charge-specific, and asymmetries may arise in the detection of the charged kaon.

Geometric asymmetries in the detector efficiency, misalignments or asymmetries in the K^+/K^- kinematics can all contribute to an asymmetry in the detected signal efficiency. To eliminate the geometric part of this asymmetry the polarity of the magnet should be reversed. MagUp data and MagDown data is provided in approximately equal proportions, allowing for the cancellation of geometric asymmetries. This is explained further in Chapter 7.

Given that the LHCb detector is made up matter, it is also therefore possible for asymmetries to arise between the interaction of CP-conjugate final states.

[63]. When traversing the material in the detector, hadrons (e.g. pions, kaons and protons) are subject to hadronic interactions with the nuclei in the material. Additional production processes are possible in K^--nucleon reactions, which are absent for their K^+-nucleon analogues [5]. Since the interaction probability of K^+ mesons is smaller, they travel further than K^- in the detector material.

The interaction probability of kaons on targets of different materials and thicknesses has been studied with simulated data [69]. Table 5.2 shows the total interaction probabilities of kaons on Aluminium of thickness 1 mm. Over the low-momentum range, the probability of K^- hadronic interactions were found to increase significantly over K^+ interactions. This difference is dominated by inelastic interactions. Good agreement was found between the measured values and those extracted from the LHEP fits (the Physics list implemented in the current LHCb simulation).

Particle	p^K (GeV/c)	P_{int}	ratio P_{int} (K^+/K^-)
K^+	1.	0.0026 ± 0.0002	1.92 ± 0.17
K^-	1.	0.0050 ± 0.0002	
K^+	5.	0.0018 ± 0.0001	1.33 ± 0.13
K^-	5.	0.0024 ± 0.0002	
K^+	10.	0.0019 ± 0.0001	1.21 ± 0.12
K^-	10.	0.0023 ± 0.0002	
K^+	100.	0.0021 ± 0.0001	1.00 ± 0.06
K^-	100.	0.0021 ± 0.0001	

Table 5.2: Summary of the total interaction probabilities P_{int} for K^+/K^- on Aluminium of 1 mm thickness. In the right column the ratio P_{int} (K^+/K^-) is reported.

The probability of interaction is larger at the kinematic extremities of the LHCb detector, where the amount of material through which a particle traverses is larger. Figure 5.8 illustrates the effect that the beam pipe has on the material budget [30].

5.3.4 Strategy for $B^{\pm}$ production asymmetry

This analysis will also make use of the $B^{\pm} \to J/\psi K^{\pm}$ decay, for the same reasons described earlier. In addition, the di-μ final states are charge symmetric and any

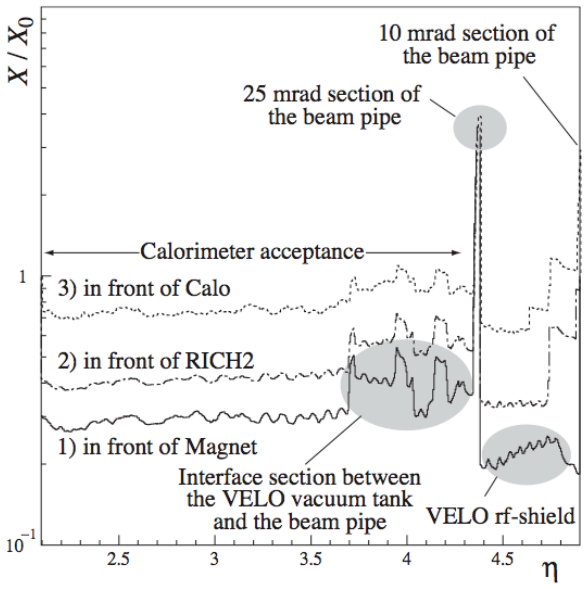

Figure 5.8: Material seen by a neutral particle originating from the nominal position of the primary vertex ($x = 0$; $y = 0$) as a function of the pseudo-rapidity at different z positions: in front of the magnet, in front of RICH2 and in front of the ECAL.

detection asymmetry will manifest only in the charged kaon. The current world average for $A_{\rm CP}(\mathrm{B}^{\pm} \to \mathrm{J}/\psi\mathrm{K}^{\pm})$ is $(+0.9 \pm 0.8)\%$ [5], which is dominated by the DØ result $(0.75 \pm 0.61 \pm 0.30)\%$ [70].

The measured (raw) asymmetry of $\mathrm{B}^{\pm} \to \mathrm{J}/\psi\mathrm{K}^{\pm}$ decays is defined as:

$$A_{raw} = \frac{n_{\mathrm{J}/\psi\mathrm{K}^-} - n_{\mathrm{J}/\psi\mathrm{K}^+}}{n_{\mathrm{J}/\psi\mathrm{K}^-} + n_{\mathrm{J}/\psi\mathrm{K}^+}} \tag{5.9}$$

where $n_{\mathrm{J}/\psi\mathrm{K}^-}$ and $n_{\mathrm{J}/\psi\mathrm{K}^+}$ are the measured yields for the two final states. Assuming a complete cancellation of geometric asymmetries, the possible sources contributing to the raw asymmetry relate to $A_{\rm p}$, $A_{\varepsilon}^{\mathrm{K}^{\pm}}$ and direct CP violation of the decay $A_{\rm CP}(\mathrm{B}^{\pm} \to \mathrm{J}/\psi\mathrm{K}^{\pm})$:

$$A_{\rm raw} = A_{\rm p} + A_{\varepsilon}^{\mathrm{K}^{\pm}} + A_{\rm CP} \tag{5.10}$$

A prediction for the kaon detection asymmetry $A_{\varepsilon}^{\mathrm{K}^{\pm}}$ using simulated $\mathrm{B}^{\pm} \to \mathrm{J}/\psi\mathrm{K}^{\pm}$ decays is given in Chapter 6. The measured asymmetry of A_{raw} of $\mathrm{B}^{\pm} \to \mathrm{J}/\psi\mathrm{K}^{\pm}$ decays, extracted using collision data collected in 2010 and 2011, is given in Chapter 7. The resulting production asymmetry A_{p} for the $\mathrm{B}^{\pm}$ meson can then be obtained, as described at the end of the chapter.

5.4 Summary

Measurements of hadron production are essential to further our understanding of the underlying quark models. Much progress has been made in the theoretical interpretation of high-energy (perturbative) QCD, where solutions exist via the use of matrix element calculations and Monte Carlo generators. The predictive power breaks down at low energy, where more approximate solutions are offered in the form of hadronisation models.

An analysis of the total and differential production cross-section of the $\mathrm{B}^{\pm}$ meson will be carried out. The heavy b-quark mass regulates certain divergences in perturbative QCD calculations, but some regions of phase space still remain unconfirmed. The decay $\mathrm{B}^{\pm} \to \mathrm{J}/\psi\mathrm{K}^{\pm}$ is one of the dominant $\mathrm{B}^{\pm}$ channels, and historically has been often used for a $\mathrm{B}^{\pm}$ cross-section measurement. The signal selection described in Chapter 6 will provide detection efficiencies from Monte Carlo data. The efficiencies will then be used to correct for the raw yields extracted from collision data, as described in Chapter 7.

An analysis of the production asymmetry of $\mathrm{B}^{\pm}$ mesons will also be carried out. Secondary interactions of the valence quarks of colliding protons with scattered particles, such as a b-quark, could give rise to a asymmetry in the production of B^{+} to B^{-} particles. This effect will be pre-dominant in the forward regions with respect to the beam axis, where the LHCb detector acceptance is sensitive. Using the decay $\mathrm{B}^{\pm} \to \mathrm{J}/\psi\mathrm{K}^{\pm}$ proves useful in cancelling some systematics, including the almost negligible CP-asymmetry in the decay. Interaction asymmetries of the kaon must still be accounted for, which is measured using Monte Carlo data in Chapter 6. Raw asymmetries are measured using collision data and used to yield a production asymmetry of $\mathrm{B}^{\pm}$, as described in Chapter 7.

Chapter 6

Simulating $B^{\pm}$ Production at LHCb

The use of Monte Carlo (MC) data is necessary to model the physics involved in an event at LHCb, and covers all aspects from the initial pp collision to the reconstruction of the decay. The main Gaudi applications have been briefly covered in Chapter 3. Of particular mention in this chapter is the Gauss application, which uses a combination of Pythia and EvtGen to handle event generation and Geant4 to simulate the detector response. This chapter will introduce the basic concepts of Pythia, EvtGen and Geant4 and explain their relevance to the production and detection of $B^{\pm} \to J/\psi K^{\pm}$ decays.

Cross-section and asymmetry predictions of the $B^{\pm}$ are available over the full solid angle. The angular coverage of LHCb limits the proportion of $B^{\pm} \to J/\psi K^{\pm}$ decays that are visible to the detector, which must be taken into account for these measurements.

Reconstructed data is filtered through sets of stripping alleys, which rejects a large proportion of unwanted data. The optimisation procedure for $B^{\pm} \to J/\psi K^{\pm}$ selection is described, taking into account the resulting detection efficiency and charge asymmetry. A particular set of trigger sequences, which use information from the muon system, provide high retention rates for selected $B^{\pm} \to J/\psi K^{\pm}$ decays.

6.1 Event Generation at LHCb

The event simulation is handled by the simulation software Gauss [71], which utilises external event generators — Pythia and EvtGen [72] — and Geant4 [34] for detector simulation.

Each event that survives the Pythia-level requirements—discussed in Section 5.1.3—is passed to the EvtGen [72] for simulation of the decay. EvtGen also handles radiative decays of charged particles through the PHOTOS package [73]. The distinguishing feature of EvtGen lies in the ability to implement the detailed decay dynamics from theoretical models. Models may handle many different decays, such as the "SVS" (scalar $\rightarrow$ vector + scalar) model that governs the $B^{\pm} \rightarrow J/\psi K^{\pm}$ decay. Specialised models also exist to simulate the many $\mathcal{CP}$ processes and rare decays that are being probed by LHCb.

Simulation of the detector response is handled by the GEANT4 package, which provides the most up-to-date detector description. Primarily this means an accurate representation of the sub-detector geometry. Of equal importance though is to provide an accurate model of particle interactions with the various materials inside the detector acceptance. LHCb uses EmOpt1 to handle electromagnetic interactions and LHEP (Low/High Energy Parameterised) to handle hadronic interactions.

6.1.1 MC10 Data Samples

The latest large-scale Monte Carlo data production is referred to as MC10. Events in MC10 samples have been passed through the entire process chain, from generation to reconstruction, providing an abundance of specific decays that reflect the needs of the various physics workgroups. The beam parameters were configured to the last few proton fills in 2010, equivalent to a centre-of-mass energy of $\sqrt{s} = 7$ TeV and an average number of visible interactions per crossing of 1.75.

There are two types of MC10 samples chosen for this analysis, defined hereafter as a signal sample and a J/ψ-inclusive sample. Each of the events in the signal sample contains a $B^{\pm} \rightarrow J/\psi K^{\pm}$ decay, with a further decay $J/\psi \rightarrow \mu^{+}\mu^{-}$.

Similarly, the J/ψ-inclusive sample contains at least one J/$\psi \to \mu\mu$ decay per event. PHOTOS is implemented to simulate radiative emission from the charged particles.

6.2 Generator-level study of $B^{\pm}$ cross-sections

We want to probe the production mechanisms of $B^{\pm}$ particles over the full solid angle (4π). This requires an MC10 signal sample with no constraint on the trajectory of the decay particles. In total, 1M events were generated, of which 500k simulated the LHCb magnet in the 'Down' polarity and 500k simulated the inverse 'Up' polarity.

6.2.1 Cross-section and asymmetry predictions

The integrated $b\bar{b}$ cross-section at $\sqrt{s} = 7$ TeV over the full solid angle (4π) is predicted by MC10 to be:

$$\sigma_{b\bar{b}}^{MC10} = 457 \pm 48 \mu\text{b} \tag{6.1}$$

The FONLL method that was performed in the previous chapter produces a $b\bar{b}$ cross-section of significantly smaller magnitude, with uncertainties from scales, masses, PDFs, combined quadratically:

$$\sigma_{b\bar{b}}^{FONLL} = 255^{+120}_{-95} \mu\text{b} \tag{6.2}$$

The discrepancy in size between Pythia (MC10) and FONLL/2010 cannot yet be explained, and may have to be taken into account for future Pythia tunings. Figure 6.1 shows the differential cross-section, $d\sigma/dp_{\text{T}}^{\text{B}}$, of $B^{\pm}$ events in a rapidity $y^{\text{B}} \in [2;4.5]$. The red band shows the central value predicted by the FONLL method, with the associated range of uncertainty. The black data-points are

obtained from the signal sample described in the previous section. The Pythia bin weights have been normalised by $\frac{1}{1.79}$ to the integrated weight of the FONLL distribution so the shapes can be compared. The $B^{\pm}$ spectra predicted by Pythia are slighter harder than that predicted by FONLL, but generally the shapes are consistent with each other.

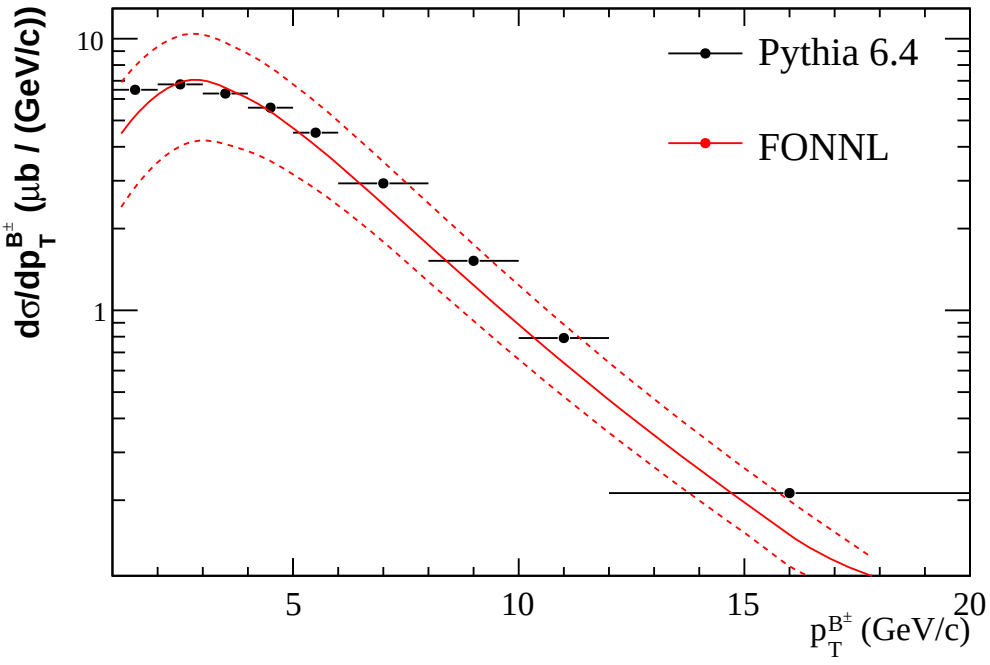

Figure 6.1: Differential cross-section $d\sigma/dp_{\mathrm{T}}^{\mathrm{B}}$ of $B^{\pm}$ events of rapidity y $\in$ [2;4.5] and $p_{\mathrm{T}}^{\mathrm{B}} > 0$ GeV/c. Shown in red is FONLL prediction (red solid line) with associated uncertainties (dashed lines). In black are $B^{\pm} \to J/\psi K^{\pm}$ decays taken from the MC sample generated independently from MC10 (i.e. no constraint on visibility of final-state particles to the LHCb detector).

The sample was also analysed for charge asymmetries. As expected at the generation-level, the measured asymmetries are independent of magnet polarity. Therefore the two 500k data-sets could be merged for this purpose. The production asymmetry, is defined here as:

$$A_{\mathrm{gen}}(4\pi) = \frac{N^{\mathrm{B}^-} - N^{\mathrm{B}^+}}{N^{\mathrm{B}^-} + N^{\mathrm{B}^+}} \tag{6.3}$$

where $N^{\mathrm{B}^{\pm}}$ represents the conjugate yields. Figures 6.2 and 6.3 show A_{gen} distributions as a function of rapidity y^{B} and transverse momentum p_T^B. The observed trend in y^{B} and, to a lesser extent, in $p_{\mathrm{T}}^{\mathrm{B}}$ are consistent with beam drag/cluster collapse. The bin-averaged production asymmetry A_{gen} over the full solid angle and in the forward region ($y^{\mathrm{B}} \in [2;\ 4.5]$) are both negative, at $(-0.79 \pm 0.1)\%$ and $(-0.90 \pm 0.11)\%$ respectively. An excess of B^+ particles are being produced, particularly at high rapidity and low momentum, providing convincing evidence that the colour interactions involving u-quark beam remnants are being allowed in the Pythia generator.

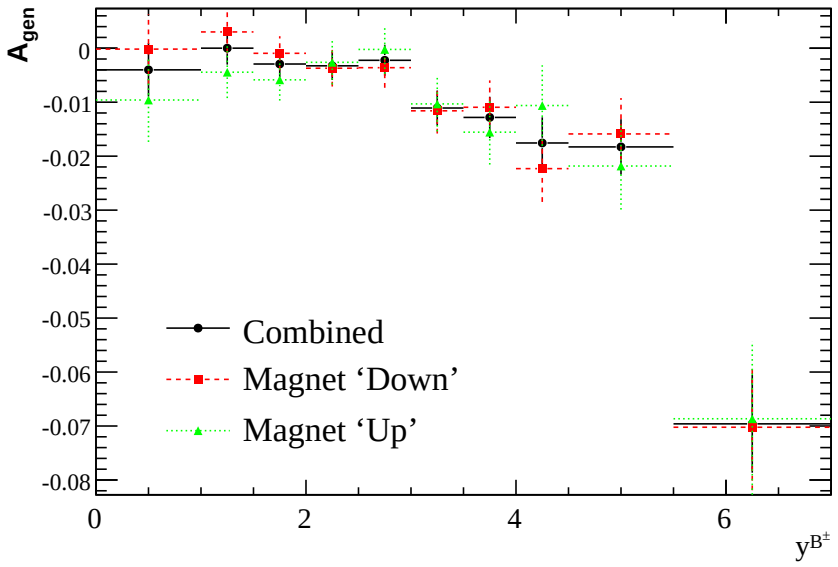

Figure 6.2: A_{gen} as a function of rapidity y^{B}, over the range $p_{\mathrm{T}}^{\mathrm{B}} \in [0;\ 20]$ GeV/c. In both polarities, the asymmetry drops significantly below zero (excess B^+ production) approaching the high rapidity region. This is consistent with the beam drag/cluster collapse hypotheses.

6.2.2 Acceptance Efficiency

Not all $\mathrm{B}^{\pm}$ particles within the range $y^{\mathrm{B}} \in [2;\ 4.5]$ and $p_{\mathrm{T}}^{\mathrm{B}} \in [0;\ 20$ GeV/c] have their final-state particles visible to the detector. This includes low-momentum B-decays that are swept outside the acceptance by the magnet. It also includes particles at the kinematic limits of the detector i.e. where $y^{\mathrm{B}} \to 1.9$ or $y^{\mathrm{B}} \to 4.9$. This retention rate is defined as the acceptance efficiency $\varepsilon_{\mathrm{acc/gen}}$.

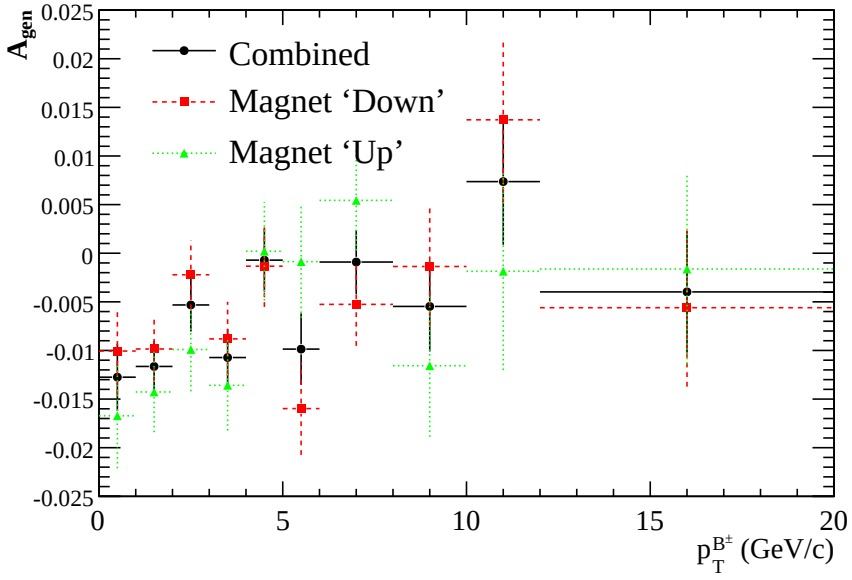

Figure 6.3: A_{gen} as a function of p_{T}^{B} over the rapidity range $y^{\text{B}} \in [0; 7]$. The dependence is less clear over this variable but there is an indication of a negative A_{gen} at low momentum. This is consistent with the beam drag hypothesis.

The MC10 signal sample was run through the event visualisation software Panoramix [74], which outputs data containing acceptance information on the decayed particles. Approximately 56% of the generated $\text{B}^{\pm}$ events were within the range $y^{\text{B}} \in [2; 4.5]$ and $p_{\text{T}}^{\text{B}} \in [0; 20\ \text{GeV/c}]$, and could therefore be used for this study. Figure 6.4 shows $\varepsilon_{\text{acc/gen}}$ as a simultaneous function of p_T^B and y^{B}. The results agree with our description of dependence on the momentum and rapidity of the B particle. A bin-averaged calculation of the efficiency is given below:

$$\varepsilon_{\text{acc/gen}} = 77.3 \pm 0.2\% \tag{6.4}$$

As shown in Figures 6.2 and 6.3 the B^+ and B^- kinematic distributions differ, with a higher proportion of B^+ particles in the high y^{B} region. The introduction of $\varepsilon_{\text{acc/gen}}$ may therefore produce a bias in the measured charge asymmetry and should be investigated. The asymmetry due to acceptance, defined as $A_{\text{acc/gen}}$, is a modified form of (6.5), taking into account the separate acceptance efficiencies for B^+ and B^- events.

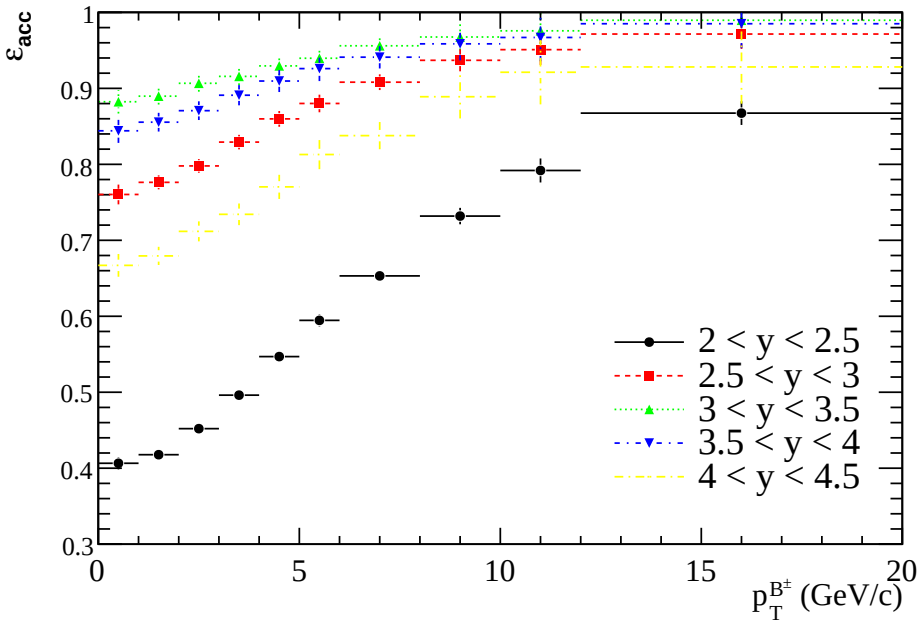

Figure 6.4: $\varepsilon_{\mathrm{acc/gen}}$ as a function of $p_{\mathrm{T}}^{\mathrm{B}}$ and per 0.5 unit rapidity in the range $y^{\mathrm{B}} \in [2; 4.5]$. High acceptance favours the mid-rapidity range ($3 < y^{\mathrm{B}} < 3.5$) and falls off as the extremities of the detector are reached. Daughters of low momentum $\mathrm{B}^{\pm}$ particles are also less likely to remain in the acceptance.

$$A_{\mathrm{acc/gen}} = \frac{\varepsilon^{\mathrm{B}^-}_{\mathrm{acc/gen}} - \varepsilon^{\mathrm{B}^+}_{\mathrm{acc/gen}}}{\varepsilon^{\mathrm{B}^-}_{\mathrm{acc/gen}} + \varepsilon^{\mathrm{B}^+}_{\mathrm{acc/gen}}} = +(0.01 \pm 0.20)\% \tag{6.5}$$

The calculation is performed separately for the opposing polarities, then combined to yield an average. Figure 6.5 shows $A_{\mathrm{acc/gen}}$ as a function y^{B} for the separate, then combined, polarities. The result is indicative of a a negligible effect of the LHCb acceptance on the asymmetry.

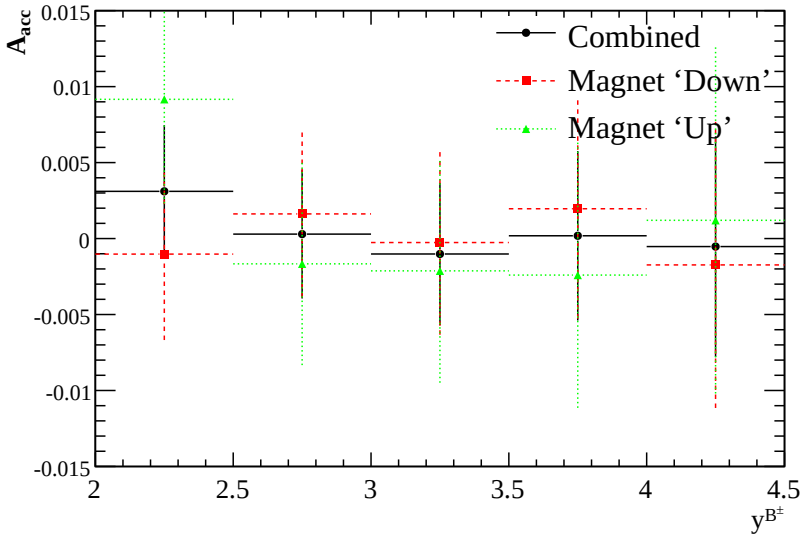

Figure 6.5: $A_{\mathrm{acc/gen}}$ as a function of rapidity y^{B}. The distribution for both polarities is observed to be consistent with zero.

6.3 Selection study using MC10

The remainder of this study will make use of an MC10 signal and J/ψ-inclusive sample. For these samples, all decay particles are required to be inside a polar angle of [10; 400 mrad] with respect to the beam axis. This is slightly looser than the LHCb acceptance — [15; 300 mrad] — so as to to avoid the loss of events due to the magnetic field. In total, 1M events were made available in the

signal sample and 1.05M for the J/ψ-inclusive sample, both with magnet 'down' polarity.

The events have already been generated (Gauss), digitised (Boole), reconstructed (Brunel), and ready for event selection via the DaVinci software.

6.3.1 Stripping pre-selection

The *stripping* pre-selection is the last stage of 'online' event filtering after the HLT. The main aim of the stripping is to reduce the number of background candidates to a manageable level while keeping the signal retention rate high. A large number of stripping alleys are executed simultaneously per event, each one optimised towards a certain decay or type of decay. The event selection in this analysis makes use of the *StrippingBu2JpsiH* alley (where 'H' represent any hadron). Many of the cuts are relatively loose and come from shared selections for common particles.

Muon candidates that form the J/ψ selection are filtered using the StdLooseMuons selection that filters on the following:

- Given a reconstructed track in the LHCb tracking system, hits in the muon stations are searched around the track extrapolation in some Field of Interest (FOI). Single muon candidates are assigned to tracks that satisfy the requirement to have a minimum number of hits in the FOI in a number of stations, depending on the momentum of the track [75].
- J/ψ candidates are formed from pairs of opposite sign muon tracks reconstructed in the full tracking system (long tracks). The following requirements must be met:
  - Good quality of the track fit (χ^2/nDoF < 5), providing effective rejection of ghost tracks that are created from disparate detector hits.
  - Using combined information from all sub-detectors the difference in the particle identification log likelihoods for the muon and pion hypotheses, $\Delta\ln\mathcal{L}_{\mu\pi}$, is greater than 0.
  - The two muons are required to originate from a common vertex, and

only candidates with a χ^2/nDoF of the vertex fit less than 16 are kept.

– Mass difference of the reconstructed J/ψ from the nominal J/ψ mass less than 80 MeV/c^2. This provides high background power to di-muon background and also to candidates with cloned tracks.

Kaon candidates are selected using the StdNoPIDKaons selection framework, which applies the following cuts:

- Long Tracks only, meaning the reconstructed track used for the kaon candidate must have hits in all of the LHCb tracking detectors (Velo, TT and downstream T stations).
- Good quality of the track fit (χ^2/nDoF < 5), again providing effective rejection of ghost tracks.

The J/ψ and kaon candidates are combined to form a B$^\pm$ candidate based on the following requirements:

- Minimum transverse momentum p_T of 500 MeV/c for the kaon candidate, effective in the removal of prompt kaons.
- Good quality of the J/ψ and K vertex fit (χ^2/nDoF < 20).
- B$^\pm$ lifetime greater than 0.15 ps, exploiting the relatively long lifetime of B mesons compared to particles and resonances.
- Mass difference of the reconstructed B$^\pm$ candidate from the nominal B$^\pm$ mass less than 500 MeV/c^2.

The *StrippingBu2JpsiH* alley was emulated on the J/ψ-inclusive sample using DaVinci v26r3p2, the same software version that was used for stripping during the 2010 LHC data-taking period.

There are enough true signal decays in the J/ψ sample to give a reasonable estimate of background-to-signal ratio (B/S). Applying the pre-selection defined above to the sample of 1.05M events yields 87032 candidates in the B$^+$ mass window [5.20; 5.45 GeV/c^2] window, of which 7008 (8.05%) are true MC signal decays. The signal is swamped in background, with a ratio $B/S = 11.4$, and the signal mass peak will not be identified from collision data with the stripping alley alone. The B$^\pm$ reconstructed mass distribution of pre-selected events in the J/ψ

sample is shown in Figure 6.6. The small (5%) peaking distribution, categorised as "low-mass" background according to the truth-matching algorithm, is confirmed to be signal decays with additional particle interactions. This contribution can therefore be absorbed into the total signal yield.

The majority of background in the J/ψ-inclusive sample is combinatoric. Prompt particles such as prompt J/ψ contribute the largest share of background, where at least one (45%) or all (8%) final-state particles used to form the candidates come directly from the primary vertex. For 28% of background candidates the final-state particles are matched to true particles from at least two different collisions (pileup). For 10% of background candidates, at least one of the final state particles is a ghost. For 8% of candidates at least one final-state particle is matched to a true decay product of a (non-signal) B-hadron. These contributions are shown in Figure 6.6.

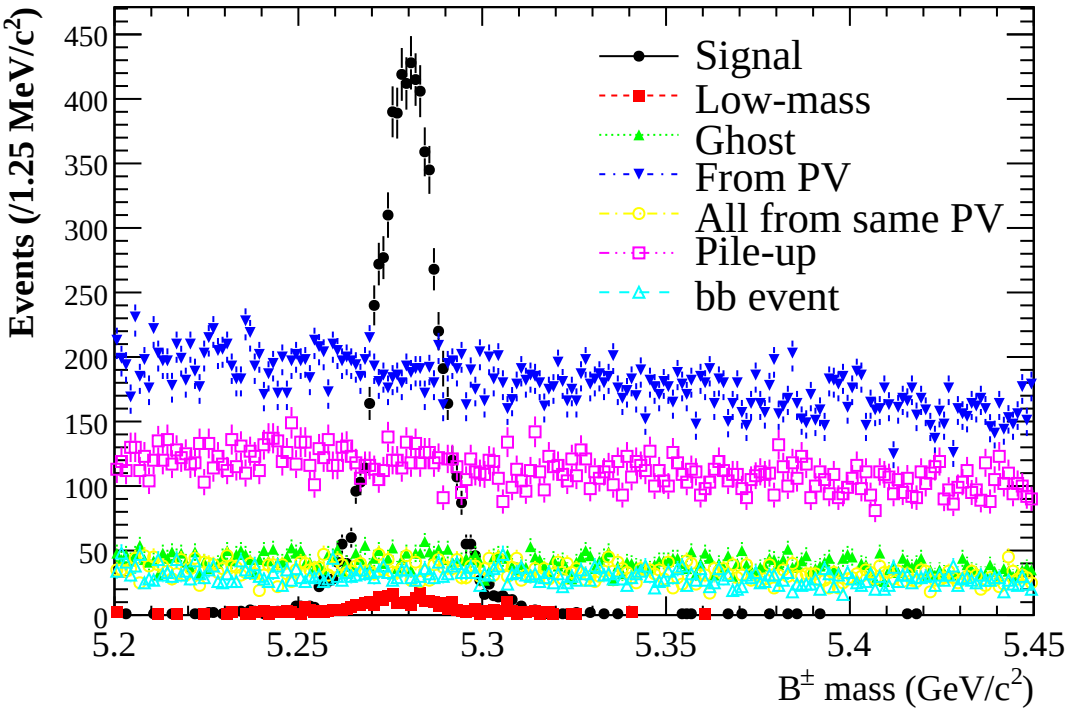

Figure 6.6: Invariant mass of pre-selected $B^\pm$ candidates from J/ψ-inclusive sample. MC truth information has been used to determine the existence and type of background.

6.3.2 Optimisation of offline selection

Events passing the pre-selection were used for the tuning of the final offline event selection. This is most effectively performed through a maximisation of the statistical significance $S/\sqrt{(S+Bx)}$, where the S and B terms are the statistical yields of signal (from the signal sample) and background (from the J/ψ-inclusive sample) that pass final selection. The x term represents the weighting that must be applied, based on the different integrated luminosities that the samples represent. This can be easily extracted from the J/ψ-inclusive sample, which in the total number of stripped candidates contains 5.10% truth-matched signal decays ($x = 19.6$). The procedure is carried out by the cut recursive optimiser (CROP) tool, developed in Ref. [76], which performs an optimisation $S/\sqrt{S+19.6B}$ based on an ensemble of user-specified cuts and file inputs.

Due to the relatively narrow width of the J/ψ mass peak, this stripping cut can be tightened, and a mass window of 50 MeV either side of the nominal J/ψ mass was applied pre-optimisation. To maximise the availability of background statistics, the full $B^{\pm}$ mass window of [5.2; 5.45] GeV/c^2 was retained.

The contribution from prompt particles is the largest contamination of background. Cuts on the χ^2 of the J/ψ and $B^{\pm}$ vertex fits are a powerful discriminator against combinatorial background, and will be included in the optimisation procedure. Also included is the lifetime cuts on the $B^{\pm}$, which exploits the relatively long life-time of B particles ($\tau_B = 1.638$ ps [5]). The signal and background distributions for the $B^{\pm}$ and J/ψ vertex fit χ^2, and also the $B^{\pm}$ lifetime, are shown in Figures 6.7, 6.8, and 6.9 respectively.

The muons from the signal decay are expected to have a larger momentum than muons from prompt J/ψ particles. This can be exploited by cutting on the lowest μ transverse momentum. The signal and background distributions of this variable are shown in Figure 6.10. Tighter cuts on the muon p_{T} will reduce the sensitivity of a $B^{\pm}$ cross-section and asymmetry measurement in the low-momentum range.

True signal $B^{\pm}$ particles should originate from the primary vertex. This can be quantified by a cut on the impact parameter (distance of closest approach) χ^2 of the $B^{\pm}$ to the primary vertex. For events containing multiple primary vertices (pile-up), the primary vertex that returns the minimum impact parameter χ^2 is

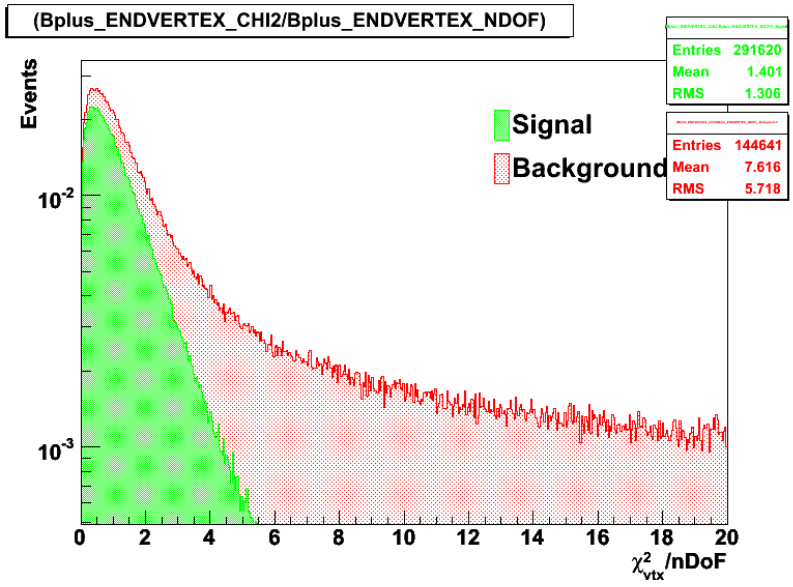

Figure 6.7: $B^{\pm}$ vertex χ^2 distributions for signal (green) events and J/ψ-inclusive (red) events, weighted to the expected signal to background ratio.

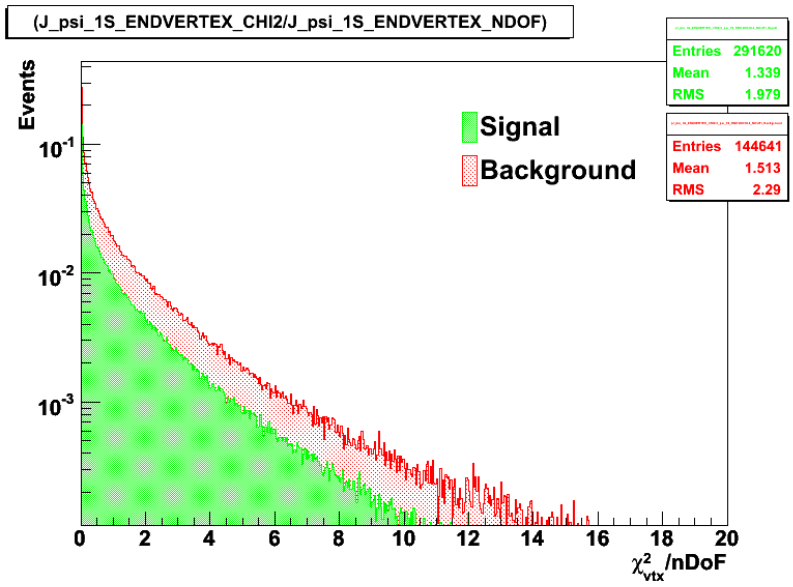

Figure 6.8: J/ψ vertex χ^2 distributions for signal (green) events and J/ψ-inclusive (red) events, weighted to the expected signal to background ratio.

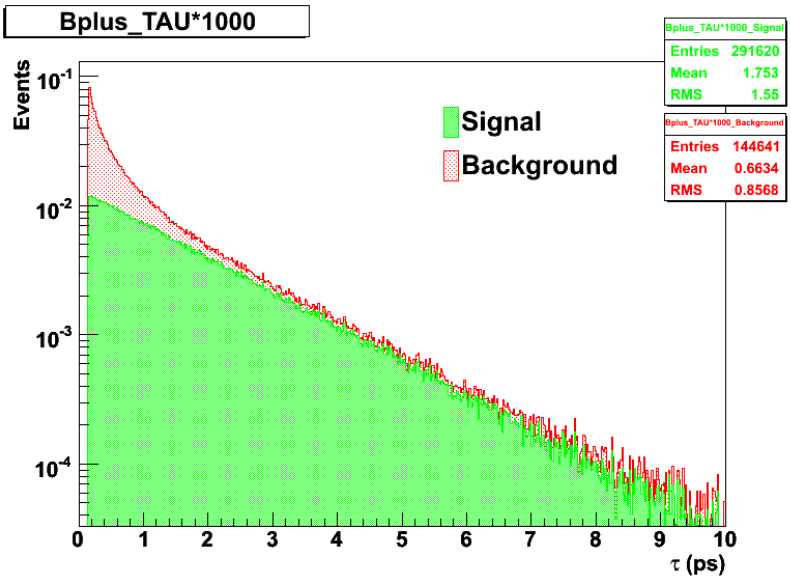

Figure 6.9: $B^{\pm}$ lifetime distributions for signal (green) events and J/ψ-inclusive (red) events, weighted to the expected signal to background ratio.

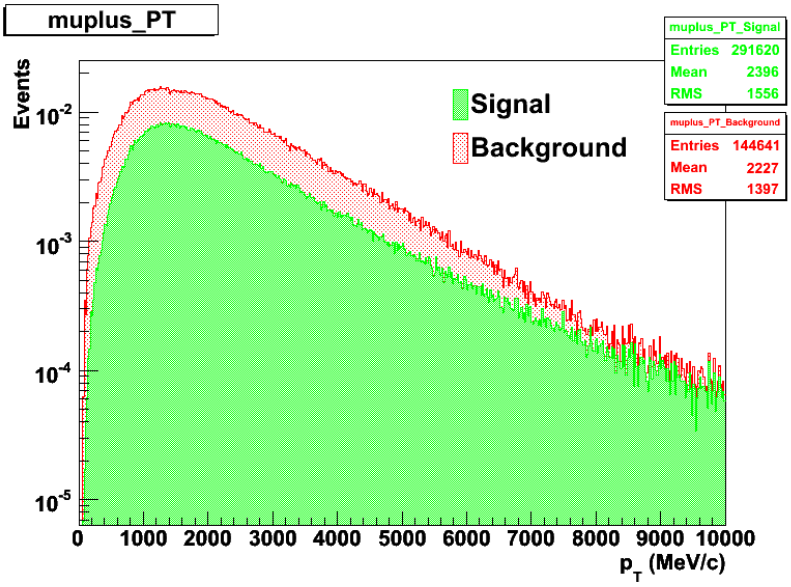

Figure 6.10: Muon p_{T} distributions for signal (green) events and J/ψ-inclusive (red) events, weighted to the expected signal to background ratio. The optimisation cuts on the muon that takes the minimum p_{T}.

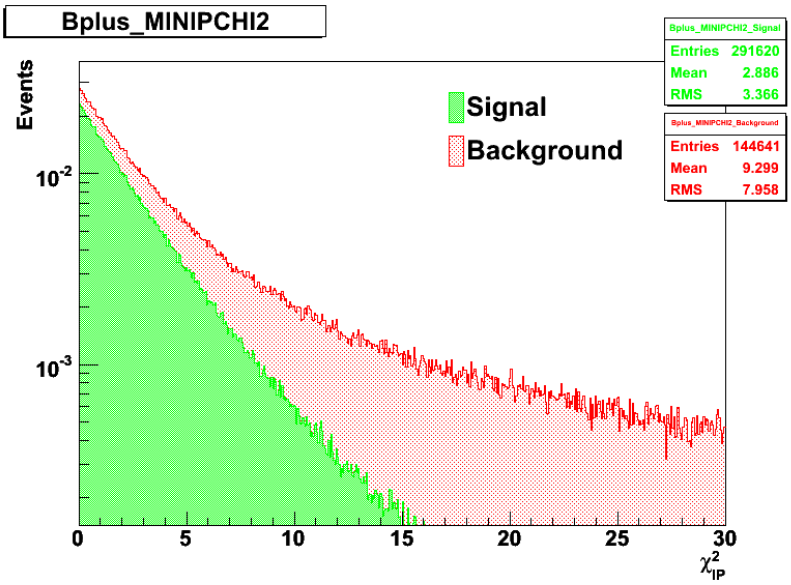

Figure 6.11: $B^{\pm}$ impact parameter χ^2 (with respect to the primary vertrex) distributions for signal (green) events and J/ψ-inclusive (red) events, weighted to the expected signal to background ratio. For multiple primary vertices, the optimisation cuts on the primary vertex that returns the minimum impact parameter χ^2.

analysed. The signal and background distributions in this parameter are shown in Figure 6.11.

The optimisation has improved the B/S dramatically, from 11.4 at the pre-selection level to 1.7 after selection. Table 6.1 summarises the selection efficiencies of true MC signal and background decays. The $\Delta M(\mathrm{J}/\psi)$ cut was applied before optimisation and so is included at the top of the table; thereafter the cuts are ordered in terms of ascending exclusive efficiency of signal[1]. Cuts on the $B^{\pm}$ lifetime and impact parameter χ^2 provide the greatest separation power, at the cost of a greater reduction in signal efficiency.

6.3.3 Selection efficiencies

We define the selection efficiency as the fraction of true $B^{\pm}$ particles (and low-mass background) within LHCb acceptance that also pass the offline selection cuts. This merges the effects from reconstruction, stripping and selection into

[1]The optimisation of the cuts were also ordered in this way.

Cut	Signal		Background	
	Excl. Eff. (%)	Total eff. (%)	Excl. Eff. (%)	Total Eff. (%)
ΔM(J/ψ) < 50 MeV/c^2	99.426 ± 0.014	99.426 ± 0.014	97.342 ± 0.042	97.342 ± 0.042
τ (B$^\pm$) > 0.3 ps	91.299 ± 0.052	90.780 ± 0.054	62.261 ± 0.127	60.706 ± 0.128
min. χ^2_{IP} (B$^\pm$) < 10	94.955 ± 0.041	86.369 ± 0.064	42.521 ± 0.130	20.142 ± 0.105
χ^2_{vtx}/nDoF (J/ψ) < 9	98.706 ± 0.021	85.306 ± 0.066	97.743 ± 0.039	19.806 ± 0.105
χ^2_{vtx}/nDoF (B$^\pm$) < 9	99.612 ± 0.012	85.099 ± 0.066	58.294 ± 0.130	12.703 ± 0.088
p_{T} (μ) > 150 MeV/c	99.962 ± 0.004	85.068 ± 0.066	99.711 ± 0.014	12.689 ± 0.088

Table 6.1: Signal and background efficiencies for optimised selection. 'Exclusive' refers to the efficiency of a cut in the absense of all other cuts; the total efficiency includes all cuts up to that point.

one. Figure 6.12 shows $\varepsilon_{\mathrm{sel/acc}}$ as a function of y^{B} and $p_{\mathrm{T}}^{\mathrm{B}}$. The $p_{\mathrm{T}}^{\mathrm{B}}$- and y^{B}-dependencies of the selection efficiency are related to efficiencies of charged track reconstruction. Low-mass background still contributes an excess of 5% to the total yield under the mass peak, and it must be absorbed into the calculation of the selection efficiency.

A bin-averaged calculation of the selection efficiency is given below:

$$\varepsilon_{\mathrm{sel/acc}} = 27.9 \pm 0.1\% \tag{6.6}$$

The difference in selection efficiency of B$^+$ decays ($\varepsilon^{\mathrm{B}^+}_{\mathrm{sel/acc}}$) and B$^-$ decays ($\varepsilon^{\mathrm{B}^-}_{\mathrm{sel/acc}}$) can be calculated as an asymmetry :

$$\begin{aligned} A_{\mathrm{sel/acc}} &= \frac{\varepsilon^{\mathrm{B}^-}_{\mathrm{sel/acc}} - \varepsilon^{\mathrm{B}^+}_{\mathrm{sel/acc}}}{\varepsilon^{\mathrm{B}^-}_{\mathrm{sel/acc}} + \varepsilon^{\mathrm{B}^+}_{\mathrm{sel/acc}}} \\ &= (-0.35 \pm 0.24)\% \end{aligned} \tag{6.7}$$

This asymmetry includes track reconstruction and is therefore an indirect measurement of the kaon detection asymmetry. The result indicates a higher reconstruction efficiency of K$^+$ particles compared to K$^-$ particles, though on a much smaller scale than the measured detection asymmetries of kaons in Aluminium (Table 5.2). The result from (6.7) will be used to calculate the B$^\pm$

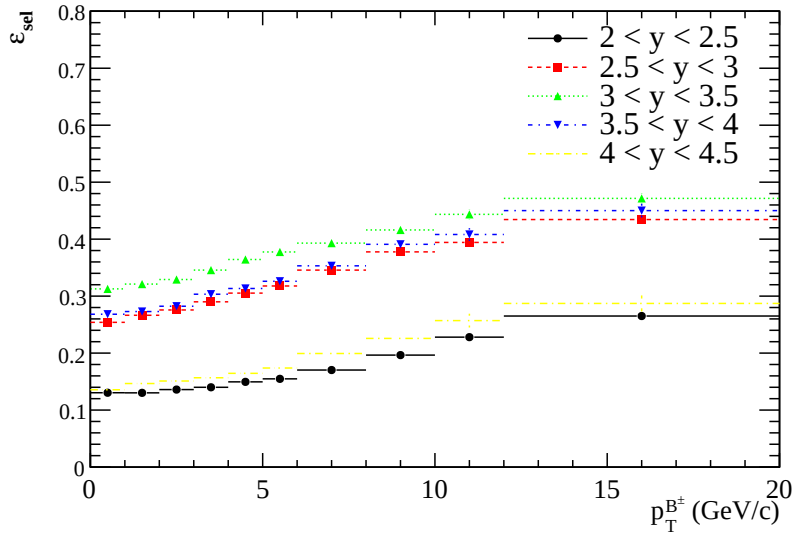

Figure 6.12: $\varepsilon_{\text{sel/acc}}$ as a function of p_{T}^{B} and per 0.5 unit rapidity in the range $y^{\text{B}} \in [2; 4.5]$. High tracking efficiency favours high momentum particles and this manifests in the p_{T}^{B}-dependence of the selection efficiency. High hit multiplicities are experienced in the tracking stations at high rapidity ($y^{\text{B}} \to 4.5$) and this has an adverse effect on the tracking efficiency.

production asymmetry in Chapter 7.

6.3.4 Application of the muon trigger

Events in the MC10 signal sample are flagged with trigger decisions, which are based on the same trigger configuration as used in October 2010 for $\sqrt{s} = 7$ TeV collisions. The sequences defined in the muon trigger are well understood, and are expected to provide a high retention rate for J/ψ muons. The series of trigger cuts used in this analysis are given in Table 6.2. The following calculations apply to offline-selected candidates that are matched to true MC signal decays.

The L0SingleMuon trigger requires the presence of an L0 muon candidate with a $p_{\text{T}} > 1.4$ GeV/c. The L0DiMuon trigger requires the presence of two L0 muon candidates with $p_{\text{T}}^1 + p_{\text{T}}^2 > 1.5$ GeV/c. Out of the 258423 selected candidates in the MC10 signal sample, 228803 pass either the L0SingleMuon trigger or L0DiMuon trigger. Trigger efficiencies as a function p_{T}^{B} and y^{B} for L0SingleMuon candidates, L0DiMuon candidates and all muon L0 candidates are shown in

Trigger line	Main cuts
L0SingleMuon	$p_{\mathrm{T}} > 1.4$ GeV/c
L0DiMuon	$p_{\mathrm{T},1} > 0.56$ GeV/c, $p_{\mathrm{T},2} > 0.48$ GeV/c
HLT1SingleMuonNoIP	L0SingleMuon and $p_{\mathrm{T}} > 1.8$ GeV/c
HLT1DiMuonNoIPL0Di	L0DiMuon and $M_{\mu\mu} > 2.5$ GeV/c
HLT1DiMuonNoIP2L0	$2 \times$ L0SingleMuon and $M_{\mu\mu} > 2.5$ GeV/c
HLT2DiMuonUnbiasedJPsi	$M_{\mu\mu} \in [M_{\mathrm{J}/\psi}$ - 120 MeV/c^2; $M_{\mathrm{J}/\psi}$ + 120 MeV/c^2]

Table 6.2: Summary of trigger algorithms and associated cuts.

Figure 6.13.

The purpose of the HLT1 Muon Alley is to confirm the presence of high p_{T} muons in events that have been triggered by L0SingleMuon or L0DiMuon. The HLT1SingleMuonNoIP algorithm confirms the muon candidate found by the L0SingleMuon, and applies a harder cut on the p_{T} at > 1.8 GeV/c. The HLT1DiMuonNoIPL0Di algorithm confirms the di-muon candidate found by the L0DiMuon and requires their combined mass to be greater than 2.5 GeV/c^2. The HLT1MuonDiMuon2L0NoIP algorithm confirms two L0SingleMuon candidates found by the L0 muon system and requires their combined mass to be greater than 2.5 GeV/c^2. This algorithm has proven to be effective in recovering di-muons that fail the L0DiMuon trigger but pass the L0SingleMuon trigger. A complete description of these trigger lines can be found in [77]. Out of the 228803 L0 muon candidates, 167737 pass at least one of the 3 HLT1 triggers mentioned here. Trigger efficiencies for L0×HLT1 candidates as a function of $p_{\mathrm{T}}^{\mathrm{B}}$ and y^{B} is shown in Figure 6.14.

The "NoIP" term indicates that no cut is made on the impact parameter of the final-state particle tracks with respect to the primary vertex. This parameter is highly correlated with B momentum, and a standard HLT IP cut may reject a significant amount of low $p_{\mathrm{T}}^{\mathrm{B}}$ signal. Cutting on the $\mathrm{B}^{\pm}$ lifetime is preferred as the calculation of the parameter takes into account the $\mathrm{B}^{\pm}$ momentum in addition to the position of the decay vertex.

Algorithms at the HLT2 level are designed for inclusive or exclusive selection of B-decays. This analysis makes use of the HLT2DiMuonUnbiasedJPsi algorithm, which accepts muon candidates within an invariant mass window of ± 120 MeV/c^2

around the nominal J/ψ mass. The retention rate is high with 150927 out of 167737 L0×HLT1 candidates passing the HLT2 trigger. Trigger efficiencies of L0×HLT1×HLT2 candidates as a function of $p_{\mathrm{T}}^{\mathrm{B}}$ are shown in Figure 6.15.

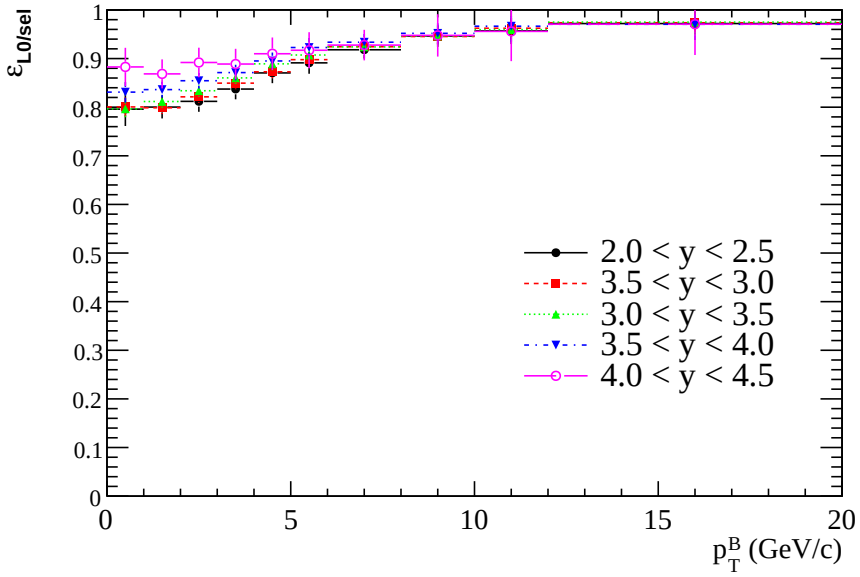

Figure 6.13: L0 trigger efficiencies of selected signal events as a function of $p_{\mathrm{T}}^{\mathrm{B}}$ and per 0.5 unit rapidity in the range $y^{\mathrm{B}} \in [2; 4.5]$. Candidates are required to have passed at least one of two algorithms: L0SingleMuon or L0DiMuon.

6.4 Summary

An analysis of Monte Carlo data has been described in this chapter, with the aim in determining some parameters that are essential to a cross-section and charge asymmetry measurement of $\mathrm{B}^{\pm}$ particles at LHCb. Simulation of the $\mathrm{B}^{\pm}$ production is handled in Pythia, which passes the relevant parameters to EvtGen for simulation of the decay and GEANT4 for simulation of the detector response. Stripping algorithms carry out the first stage of event filtering, applying selection cuts that are common to many decays. The final selection cuts have been optimised to maximise selected signal events while minimising selected background events. Muon triggers provide the highest retention rates for selected signal decays and have been chosen for this analysis.

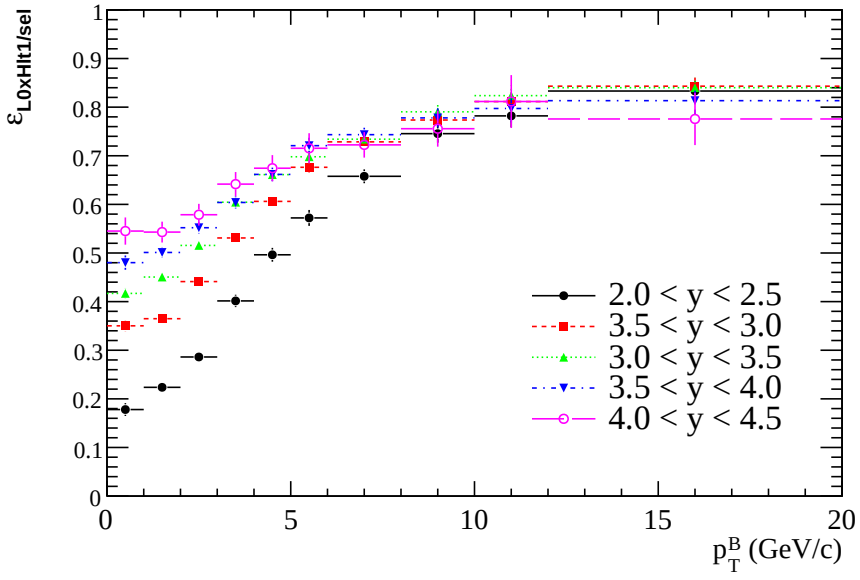

Figure 6.14: HLT1 trigger efficiencies of L0-triggered signal events as a function of $p_{\mathrm{T}}^{\mathrm{B}}$ and per 0.5 unit rapidity in the range $y^{\mathrm{B}} \in [2;\ 4.5]$. Candidates are required to have passed at least one of three algorithms: HLT1SingleMuonNoIP, HLT1DiMuonNoIPL0Di or HLT1MuonDiMuon2L0NoIP.

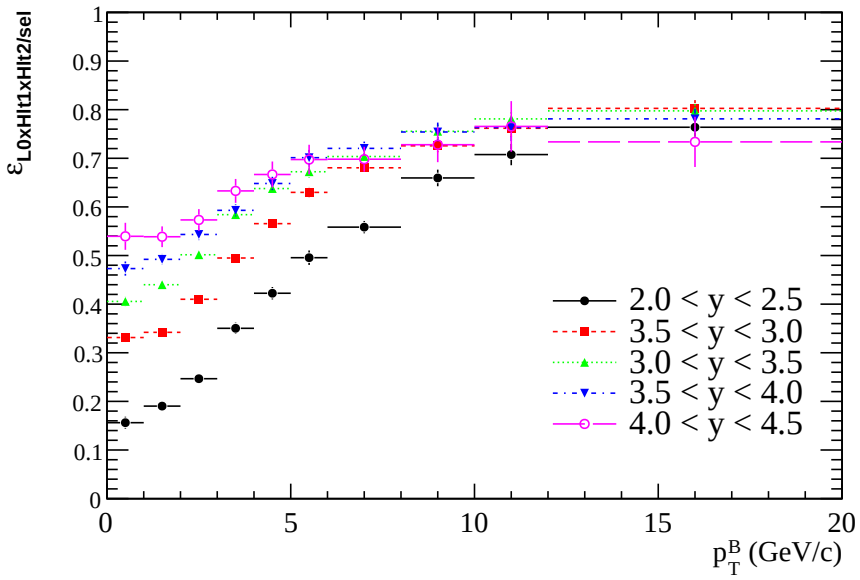

Figure 6.15: HLT1 trigger efficiencies of (L0+HLT1)-triggered signal events as a function of $p_{\mathrm{T}}^{\mathrm{B}}$ and per 0.5 unit rapidity in the range $y^{\mathrm{B}} \in [2;\ 4.5]$. Candidates are required to have passed the algorithm: HLT2DiMuonUnbiasedJPsi.

All efficiencies relating to the detection of $B^{\pm} \to J/\psi K^{\pm}$ (signal) decays have been determined using simulated data, and are summarised in Table 6.3. The $\varepsilon_{\mathrm{acc/gen}}$ term describes the proportion of signal decays within the LHCb acceptance. Poorly reconstructed signal decays are rejected by the stripping and selection algorithms, and events within the LHCb acceptance have an associated selection efficiency $\varepsilon_{\mathrm{sel/acc}}$. Muon trigger sequences have tight momentum requirements, resulting in further rejection of signa decays. The trigger efficiency of selected signal events is defined at the L0 level ($\varepsilon_{\mathrm{L0/sel}}$), HLT1 level ($\varepsilon_{\mathrm{L0xHLT1/sel}}$) and HLT2 level ($\varepsilon_{\mathrm{L0xHLT1xHLT2/sel}}$). A total efficiency of $(12.0 \pm 0.1)\%$ is obtained for generated events.

Sample	Parameter	Efficiency (%)
Generated	$\varepsilon_{\mathrm{acc/gen}}$	77.3 ± 0.2
MC10	$\varepsilon_{\mathrm{sel/acc}}$	26.5 ± 0.1
MC10	$\varepsilon_{\mathrm{L0/sel}}$	88.5 ± 0.3
MC10	$\varepsilon_{\mathrm{L0xHLT1/sel}}$	61.6 ± 0.2
MC10	$\varepsilon_{\mathrm{L0xHLT1xHLT2/sel}}$	58.4 ± 0.2
	ε_{tot}	12.0 ± 0.1

Table 6.3: Summary of $B^{\pm}$ efficiency parameters, in the fiducial region $2 < y^{\mathrm{B}} < 4.5$ and $0 < p_{\mathrm{T}} < 20$ GeV/c.

Charge asymmetries relating to the detection of signal decays take into account the efficiencies for B^+ particles and B^- particles separately, and are summarised in Table 6.4. The Monte Carlo event generator Pythia uses the Lund string fragmentation model for hadronisation, which allows for interactions between scattered particles and the beam remnant. The charge asymmetry of generated events A_{gen} (6.3) is found to be negative, indicative of a production excess of B^+ particles over B^- particles. The asymmetry of generated events that are within the LHCb acceptance $A_{\mathrm{acc/gen}}$ (6.6) is found to be negligible. The hadronic cross-section of K^- particles is known (Sec. 5.3.3) to be larger than K^+ particles, and this is expected to manifest in the reconstruction of signal decays at LHCb. The asymmetry of decays within the acceptance that are selected $A_{\mathrm{sel/acc}}$ (6.7) does indicate this asymmetry, though with an almost negligible magnitude. A resulting asymmetry, of $A_{\mathrm{tot}} = (-1.25 \pm 0.27)\%$ is found, incorporating all stages of the event from production to subsequent decay and selection.

Sample	Parameter	Asymmetry (%)
Generated	A_{gen}	$(-0.90 \pm 0.11)\%$
Generated	$A_{\text{acc/gen}}$	$(0.01 \pm 0.20)\%$
MC10	$A_{\text{sel/acc}}$	$(-0.35 \pm 0.24)\%$
	A_{tot}	$(-1.25 \pm 0.27)\%$

Table 6.4: Summary of asymmetries, in the fiducial region $2 < y^{\text{B}} < 4.5$ and $0 < p_{\text{T}} < 20$ GeV/c.

Chapter 7

Measuring $B^{\pm}$ Production at LHCb

An overview of $B^{\pm}$ cross-section and production asymmetry measurements was given in Chapter 5, with focus on how these measurements are performed at LHCb. This was followed up in Chapter 6 by an analysis of simulated data, yielding a set of offline and trigger cuts which are optimised to the selection of $B^{\pm} \to J/\psi K^{\pm}$ decays. In addition, estimates were made of efficiencies and asymmetries relating to the detection of the decay. This chapter will detail an analysis of selected $B^{\pm} \to J/\psi K^{\pm}$ events at LHCb, using pp collision data recorded in 2010 and 2011. The methodologies for the $B^{\pm}$ cross-section and asymmetry measurement will be described in Sec. 7.1 and 7.2 respectively.

7.1 Cross-Section Measurement

Reported here is a measurement of the $B^{\pm}$ production cross-section at a centre-of-mass energy of $\sqrt{s} = 7$ TeV with (27.6 ± 2.8) pb^{-1} data collected by the LHCb detector in 2010. The total cross-section and differential cross-section as a function of $B^{\pm}$ transverse momentum $p_{\mathrm{T}}^{\mathrm{B}}$, $d\sigma/dp_{\mathrm{T}}^{\mathrm{B}}$, for $y \in [2, 4.5]$ has been measured. Several of the techniques have been adopted from Ref. [62], in which a similar measurement of $B^{\pm}$ production is described.

Sec. 7.1.1 describes the extraction of raw $B^{\pm} \to J/\psi K^{\pm}$ yields. Muon trigger

efficiencies determined with MC in Chapter 6 are verified with collision data in Sec. 7.1.2.

The Global Event Cut (GEC) performs rejection of high multiplicity events, and its effect on the signal yield is quantified in Sec. 7.1.3. Comparisons with MC data are also included.

Sources of systematic uncertainty are investigated and quantified, as described in Sec. 7.1.4.

Taking into account all detector effects allows for a calculation of the $B^{\pm}$ cross-section. This is described in Sec. 7.1.5, with theoretical predictions included for comparison.

7.1.1 Extraction of signal yields

The $B^{\pm}$ signal yield is extracted from an extended unbinned maximum likelihood fit to the $B^{\pm}$ invariant mass distribution, using a single Gaussian to describe the signal peak and a first-order polynomial (linear function) to describe the flat background. Figure 7.1 shows the invariant mass distribution of signal candidates selected from 16.1 pb^{-1} of MagDown data.

The fitted mean of the Gaussian deviates slightly from the true $B^{\pm}$ mass of 5279.17 ± 0.29 MeV/c^2 [5]. This is believed to be caused by a mis-calibration in momentum measurements of decay particles, as described in [78], and has since been corrected. There is also a significant low-mass contribution that may be caused by radiative emission of the signal decay particles. This will be taken into account in a discussion on systematic uncertainties (Sec. 7.1.4).

A kinematic fit of the $B^{\pm}$ vertex is improved upon traditional fit models by constraining the J/ψ mass to its known value, as described in [79]. This results in a mass resolution ($\sigma = 10.01 \pm 0.19$ MeV/c^2) that is consistent with the average momentum resolution of LHCb ($\delta p/p = 0.35\%$).

From the fit we can extract a signal yield of 4570 ± 85 in the MagDown sample, and 2858 ± 65 in the MagUp sample. The fitted parameters of the mass distribution are used to weight each candidate with a probability of being signal or background, based on the reconstructed $B^{\pm}$ mass. The technique is known as

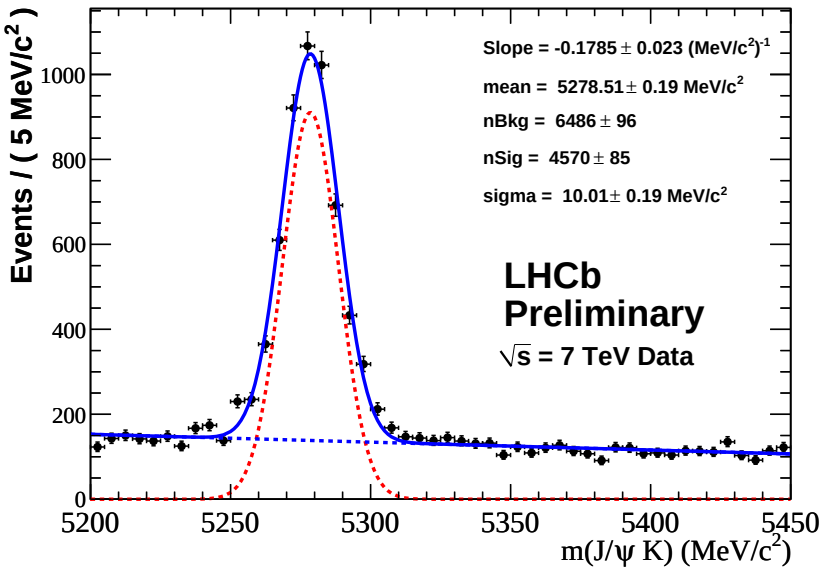

Figure 7.1: Invariant mass distribution of $B^{\pm}$ candidates selected from the 2010 collision sample, with Gaussian (red dashed), linear (blue dashed) and combined (blue solid) fit overlaid. Candidates are required to have triggered on sequence defined in Table 6.2.

sPlot (described in [80]), and for the purposes of this analysis has been useful for producing background-subtracted distributions in un-correlated variables e.g. y^{B}, $p_{\mathrm{T}}^{\mathrm{B}}$.

7.1.2 Calculation of muon trigger efficiency

A direct comparison of trigger efficiencies between 2010 non-pre-scaled data and MC10 (see Sec. 6.3.4) can be made as the trigger configuration is the same. The method requires candidates where triggers were fired independently from the signal J/ψ muons, which can be from any trigger line including those of hadronic, leptonic or photonic type. For simplicity, we define these candidates as type "trigger-independent-signal" (TIS), as opposed to "trigger-on-signal" (TOS) where the signal J/ψ muons are involved in the trigger. The trigger efficiency takes the ratio of TIS signal yields (N^{TIS}) to TIS+TOS signal yields $N^{TOS+TIS}$, as given below:

$$\varepsilon_{tri} = \frac{N_{TOS\&TIS}}{N_{TIS}} \tag{7.1}$$

These distributions are shown, alongside results for the 2010 pre-scaled data sample, as a function of $p_{\mathrm{T}}^{\mathrm{B}}$ in Figure 7.2. The calculation incorporates the entire L0×Hlt1×Hlt2 trigger sequence defined in Chapter 6. The distributions all show similarity in shape, with the pre-scaled sampled deviating only in magnitude from the non-pre-scaled samples. As the amount of collision data is insufficient to provide a precise determination of trigger efficiency, it was instead decided to use the MC10 data for the trigger efficiency determination in parallel with the non-pre-scaled 2010 sample for the raw yields.

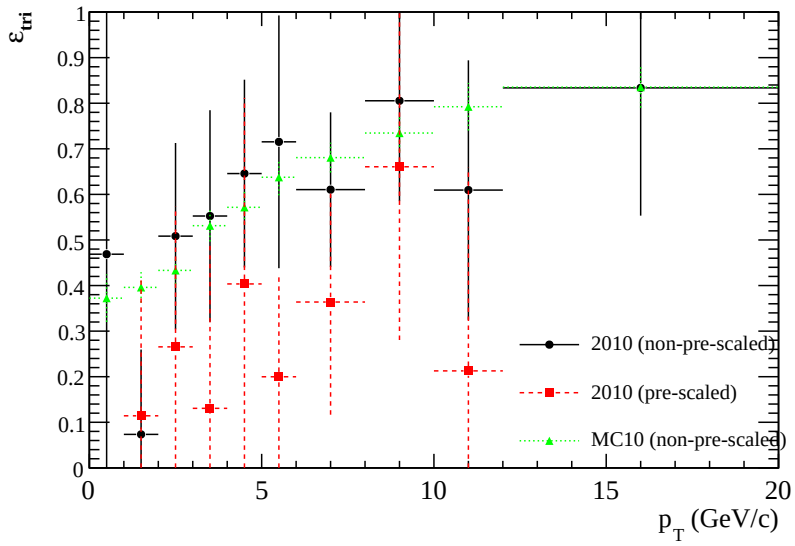

Figure 7.2: Trigger efficiencies ε_{tri} as a function of $p_{\mathrm{T}}^{\mathrm{B}}$ for the non-pre-scaled 2010 data sample (black), pre-scaled 2010 data sample (red) and MC10 data sample (green).

7.1.3 Global Event Cut

The increase in pile-up (average visible interactions per crossing) throughout 2010 stretched the CPU time spent per event of the HLT1 nodes to their limit.

In addition to an increase in trigger thresholds, a set of Global Event Cuts (GEC) were implemented for the VELO, IT, OT and SPD to reject these busy events.

VELO clusters are created in a similar way to HPD pixel clusters[1], and are an indication of the total activity generated by the charged tracks in the event. A GEC of < 3000 VELO clusters rejected a significant portion of signal in the 2010 data sample as shown in Figure 7.3. The distribution has been background-subtracted using sWeights. We want to extrapolate beyond the cut threshold to estimate the rejected signal yield. An extended un-binned maximum likelihood fit was performed on the cluster distributions, represented in the figure by a Gamma distribution. The fit returns a mean of 1610 clusters and an efficiency of 94.4 $\pm$ 0.3 %, where the uncertainty is associated to the uncertainties in the parameters of the Gamma fit and is assigned as a systematic.

A Gamma fit was also performed on the cluster distribution of the (background-subtracted) MC10 signal sample, as shown in Figure 7.4. No TOS requirement is imposed on selected events, which applies to both muon trigger and GEC, therefore the distribution extends beyond 3000 clusters. The Gamma fit returns a mean of 1521 and a GEC efficiency of 95.0 $\pm$ 0.2%. A direct extraction of the yields returns an efficiency of 94.9%, in reasonable agreement with the Gamma fit method.

As mentioned, the GEC is already incorporated into the MC10 events. We use the ratio of GEC efficiencies between the MC10 data sample and the 2010 data sample (= 1.01) as a correction factor to the final raw $B^{\pm}$ yields (see Sec. 7.1.5), and assign a corresponding systematic uncertainty of 0.3%.

7.1.4 Systematic Uncertainty

Uncertainties in our knowledge of the physics and of the detector give rise to systematic uncertainties in the calculated $B^{\pm}$ cross-section. Table 7.1 summarises the main contributions, each of which are described below.

The extrapolation of yields to a $B^{\pm}$ cross-section is dominated by uncertainties

[1] A VELO sensor strip is selected as a seeding strip if the signal passes a certain *seeding* threshold. Strips next to the seeding strips are included in the cluster if their signals are above a smaller *inclusion* threshold cut [21].

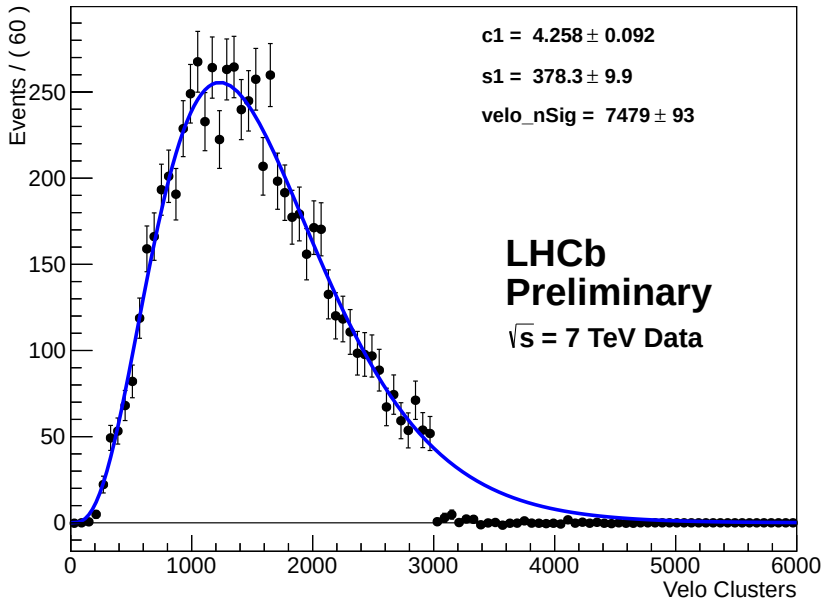

Figure 7.3: Distribution of reconstructed VELO clusters per event for 2010 collision data, with Gamma fit overlaid. Cut on the number of VELO clusters of < 3000 is applied.

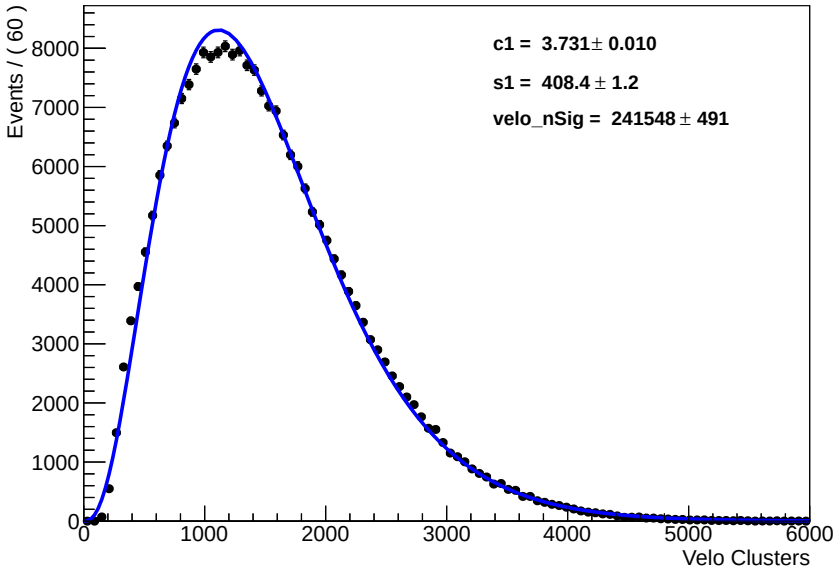

Figure 7.4: Distribution of reconstructed VELO clusters per event for MC10 data, with Gamma fit overlaid.

Quantity	Systematic uncertainty	Comment
Tracking efficiency	0.7% (per μ)	Correlated between bins
	1.7% (per $K^{\pm}$)	Correlated between bins
Muon identification	1.6% per muon	Correlated between bins
χ^2_{vtx} ($B^{\pm}$)	1.6%	No bin dependency
χ^2_{IP} ($B^{\pm}$)	1.7%	No bin dependency
τ ($B^{\pm}$)	1.5%	Correlated between bins
Trigger efficiency	0.7% - 12.8%	Bin dependent
	(5.0%)	(Bin-averaged)
Inter-bin cross-feed	0.3%	Bin dependent
GEC efficiency	0.3%	No bin dependency
Radiative tail	1%	No bin dependency
$\mathcal{B}(B^{\pm} \to J/\psi K^{\pm})$	3.4%	No bin dependency
$\mathcal{B}(J/\psi \to \mu\mu)$	1%	No bin dependency
$\mathcal{L}_{\text{int}}$	10%	No bin dependency
Total (syst.)	7.3%	Bin-averaged

Table 7.1: Systematic uncertainties of measured $B^{\pm}$ cross-section, expressed as a percentage. The uncertainties are un-correlated with each other and are added in quadrature to obtain the total systematic uncertainty, with uncertainty from inter-bin cross feed excluded as the contribution is negligible to the total cross-section. The uncertainty in luminosity can be easily improved upon and is kept separate.

in the luminosity $\mathcal{L}_{int}$, branching fraction $\mathcal{B}$ and trigger efficiency. A relative uncertainty of 10% is assigned to the integrated luminosity, which is significantly larger than the 3.5% uncertainty obtained in Sec. 3.11 owing to an older version of the reconstruction. The uncertainty in the branching fraction of $B^{\pm} \to J/\psi K^{\pm}$ decays (3.4%) is limited by existing experimental data. Uncertainties in the trigger arise from the fact that we are using Monte Carlo simulation, rather than results from the 2010 data sample, due to the lack of available muon TIS statistics. An independent study of $B^{\pm} \to J/\psi K^{\pm}$ decays described in Ref. [62] found uncertainties on trigger efficiencies range from 0.7%–12.8% depending on the p_T and y^B bin (though there is no bin correlation).

Uncertainties related to charged track-finding have been measured using 380 pb^{-1} of data taken in 2011, as described in [81]. A tag-and-probe technique is implemented on $J/\psi \to \mu^+\mu^-$ decays, where one of the muons (the 'tag' leg) is fully reconstructed, while the other particle (the 'probe' leg) is only partially reconstructed. The tracking efficiency is then obtained by trying to match the partially reconstructed probe leg to a reconstructed long track. Consistency tests are performed by varying the fit strategy and type of tag/probe leg. Discrepancies between results are then assigned as systematic uncertainties, which was found, on average, to be 0.7% per μ track. A larger uncertainty of 1.5% was assigned to kaon tracks, owing to hadronic interaction effects in the detector material [81].

Muon ID performance, determined using 2010 data, is described in [75]. Similar to the tracking efficiency determination, this study applies a tag-and-probe method on $J/\psi \to \mu^+\mu^-$ decays. The 'tag' muon has been fully reconstructed using information from the muon system, while the 'probe' muon is identified selecting a track depositing a minimum amount of energy in the calorimeters. With the application of a muon ID requirement there is reasonable agreement in efficiency between MC and data. The integrated efficiency over the full momentum spectrum is found to be $(97.3 \pm 1.3\%)$ for 2010 data. The statistical uncertainty (1.3%) is taken as the systematic uncertainty for this analysis due to the equivalence of muon ID cuts made in the *StrippingBu2JpsiH* alley.

Uncertainty in the B-lifetime (τ) can manifest in the selection efficiency, and is estimated in the data sample by changing the optimised cut value ($\tau(B^{\pm}) > 0.3$ ps) by $\pm\, 1\sigma$. Low momentum $B^{\pm}$ candidates that decay closer to the primary vertex

	1	2	3	4	5	6
1: χ^2_{IP} ($B^{\pm}$)	1.000	0.002	0.000	0.001	0.001	-0.000
2: p_T (μ)	0.002	1.000	0.006	0.154	0.007	0.000
3: χ^2_{vtx}/nDoF (J/ψ)	0.000	0.006	1.000	0.004	0.545	0.001
4: p_T ($K^{\pm}$)	0.001	0.154	0.004	1.000	0.011	-0.004
5: χ^2_{vtx}/nDoF ($B^{\pm}$)	0.001	0.007	0.545	0.011	1.000	-0.000
6: τ ($B^{\pm}$)	-0.000	0.000	0.001	-0.004	-0.000	1.000

Table 7.2: Correlation matrix of all cuts used for the optimised event selection.

are more susceptible to the uncertainty, as shown in Figure 7.5. The efficiency, averaged over the entire momentum spectrum, has an associated uncertainty of 1.5%.

Uncertainties relating to the vertex fit (χ^2_{vtx}) and impact parameter fit (χ^2_{IP}) of the $B^{\pm}$ are determined separately using a comparison of MC10 and 2010 data. Studying the efficiency of the cut requires the cut to be removed, which creates additional background in the $B^{\pm}$ mass distribution. To keep these background levels sufficiently low, the τ cut is tightened to 0.4 ps. As shown in the correlation matrix (Table 7.1.4), a change in the τ cut will not bias the χ^2_{vtx}/χ^2_{IP} spectrum and can therefore be used for this purpose. The efficiency is then calculated as the ratio of extracted signal yields with and without the χ^2_{vtx}/χ^2_{IP} cut.

The effect of the $\chi^2_{vtx} < 8$ cut is shown in Figure 7.6. There is good agreement over the entire p_T^B range, with bin-averaged efficiencies of $(99.8 \pm 0.4)\%$ for MC10 and $(99.3 \pm 1.7)\%$ for 2010 data. The corresponding distribution for the $\chi^2_{IP} < 10$ cut is shown in Figure 7.7. There is a systematic shift in efficiency between samples, with bin-averaged efficiencies of $(95.7 \pm 0.4)\%$ for MC10 and $(91.2 \pm 1.6)\%$ for 2010 data. We use the ratio between theses two results (~ 1.05) as a correction factor to the final raw $B^{\pm}$ yield (see Sec. 7.1.5), and assign a systematic uncertainty of 1.6% to the χ^2_{IP} cut. A scale factor of 1.06, combined with the GEC scale factor, will be applied to the $B^{\pm}$ cross-section.

Due to the finite p_T resolutions, $B^{\pm}$ candidates can be assigned to a wrong p_T bin. A comparison of true and reconstructed p_T of selected $B^{\pm}$ particles show this effect to be very small, with a variation of less than 0.3% between bins. This effect is negligible for the total cross-section calculation.

Signal decays with radiative emission may be the cause of the low-end tail

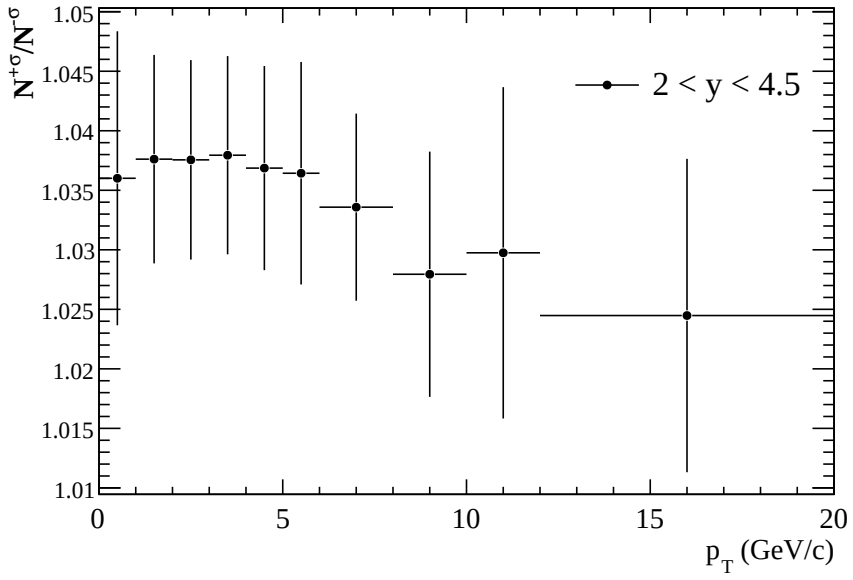

Figure 7.5: Ratio of fit-extracted signal yields with $B^{\pm}$-lifetime cut $(\tau + 1\sigma)$ to signal yields with $B^{\pm}$-lifetime cut $(\tau - 1\sigma)$ as a function of p_T^B.

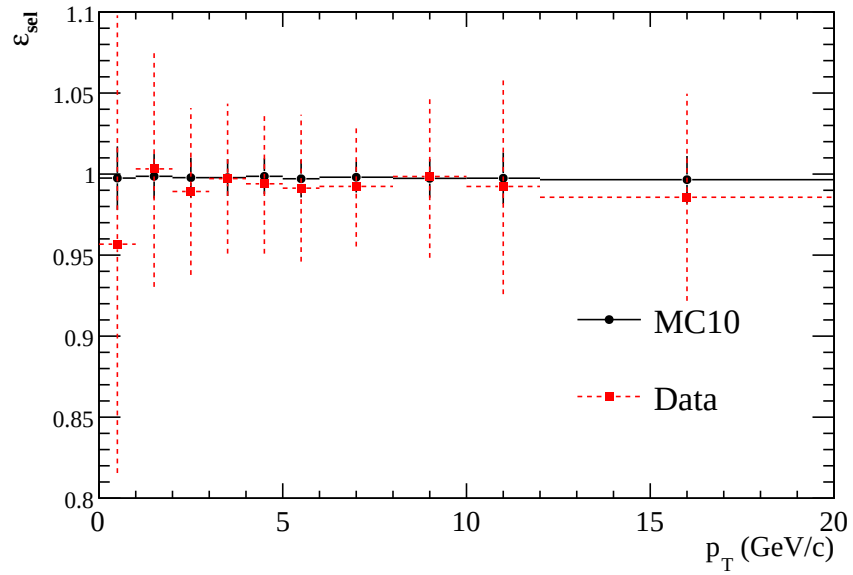

Figure 7.6: Ratio of fit-extracted signal yields with $\chi^2_{vtx} < 8$ to signal yields without $\chi^2_{vtx} < 8$ for 2010 data sample (red dashed) and MC10 (black solid). A tight cut is applied on the $B^{\pm}$ lifetime $\tau > 0.4$ ps to compensate for increased background levels when removing the $\chi^2_{vtx} < 8$ cut.

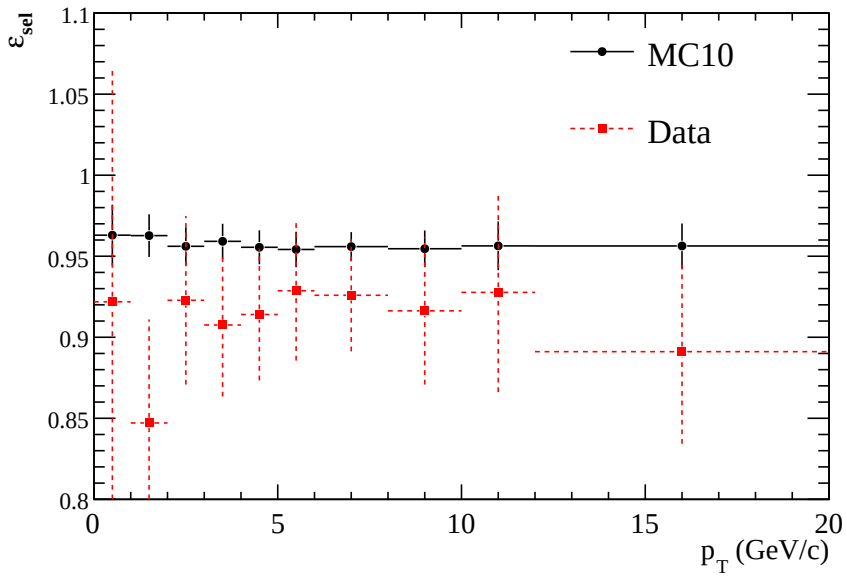

Figure 7.7: Ratio of fit-extracted signal yields with $\chi^2_{IP} < 10$ to signal yields without $\chi^2_{IP} < 10$ for 2010 data sample (red dashed) and MC10 (black solid). A tight cut is applied on the $B^{\pm}$ lifetime $\tau > 0.4$ ps to compensate for increased background levels when removing the $\chi^2_{IP} < 10$ cut.

observed in the $B^{\pm}$ mass distribution in Figure 7.1. A Crystal Ball function [82] consists of a Gaussian core portion and a power-law low-end tail below a certain threshold, and may be better suited to describe to describe the signal peak than a single Gaussian. The Crystal Ball function is given by:

$$f(x;\alpha,n,\bar{x},\sigma) = N \cdot \begin{cases} \exp(-\frac{(x-\bar{x})^2}{2\sigma^2}), & \text{for } \frac{(x-\bar{x})}{\sigma} > -\alpha \\ A \cdot (B - \frac{(x-\bar{x})}{\sigma})^{-n}, & \text{for } \frac{(x-\bar{x})}{\sigma} \leq -\alpha \end{cases} \tag{7.2}$$

where

$$A = \left(\frac{n}{|\alpha|}\right)^n \cdot \exp\left(-\frac{|\alpha|^2}{2}\right) \tag{7.3}$$

$$B = \frac{n}{|\alpha|} - |\alpha| \tag{7.4}$$

N is a normalisation factor and $\alpha, n, \bar{x}, \sigma$ are parameters that are fitted with the data. Re-fitting the 2010 data sample with a Crystal Ball does indeed produce a 2% increase in the extracted signal yield, though it is unclear whether or not radiative signal decays account for the increase. Re-fitting true signal decays in the MC10 sample with a Crystal Ball function produces only a 0.5% increase in extracted signal yield, of comparable order to the statistical uncertainty. The 2% discrepancy between fit methods is assigned as a systematic uncertainty to the final result.

7.1.5 Results

The required parameters for a measurement of the $\mathrm{B}^{\pm}$ cross-section—integrated over $p_{\mathrm{T}}^{\mathrm{B}} \in [0;\ 20\ \mathrm{GeV/c}]$ and $y^{\mathrm{B}} \in [2;\ 4.5]$—are summarised below, along with their associated statistical uncertainties:

- Raw signal yields $(N_{\mathrm{tot}}^{\mathrm{B}}) = (N_{\mathrm{MagDown}}^{\mathrm{B}} + N_{\mathrm{MagUp}}^{\mathrm{B}}) = 7811 \pm 102$
- Scale factors M $(\mathrm{GEC};\chi^2_{IP}) = 1.06$
- Integrated luminosity $(\mathcal{L}_{\mathrm{int}}) = 27.6\ \mathrm{pb}^{-1}$
- Detection efficiency $(\varepsilon_{\mathrm{tot}}) = (12.0 \pm 0.1)\%$
- Branching fraction $\mathcal{B}(\mathrm{B}^{\pm} \to \mathrm{J}/\psi\mathrm{K}^{\pm}) = 1.014 \times 10^{-3}$
- Branching fraction $\mathcal{B}(\mathrm{J}/\psi \to \mu\mu) = 5.93 \times 10^{-2}$

The cross-section σ_{tot}^{B} can then be calculated as follows:

$$\begin{aligned}\sigma_{tot}^{B} &= \frac{N_{\mathrm{tot}}^{B} \cdot M}{\mathcal{L}_{\mathrm{int}} \cdot \varepsilon_{tot} \cdot \mathcal{B}(\mathrm{B}^{\pm} \to \mathrm{J}/\psi\mathrm{K}^{\pm}) \cdot \mathcal{B}(\mathrm{J}/\psi \to \mu^{+}\mu^{-})} \\ &= [41.6 \pm 0.6\ (\mathrm{stat.})\ \pm 3.0\ (\mathrm{sys.})\ \pm 4.2\ (\mathrm{lumi.})]\ \mu\mathrm{b} \end{aligned} \tag{7.5}$$

where the uncertainties are stastical, systematic and from luminosity respectively.

These results are in good agreement with the $\mathrm{B}^{\pm} \to \mathrm{J}/\psi\mathrm{K}^{\pm}$ analysis described in Ref. [62], reporting a $\mathrm{B}^{\pm}$ cross-section integrated over the equivalent region ($p_{\mathrm{T}}^{\mathrm{B}} \in [0;\ 20\ \mathrm{GeV/c}]$ and $y^{\mathrm{B}} \in [2;\ 4.5]$):

$$\sigma^{B}_{tot} = 37.1 \pm 1.9 \text{ (stat.)} \ \pm 5.3 \text{ (sys.)} \ \mu\text{b} \tag{7.6}$$

The differential cross-section with respect to p_{T} is shown together with the results obtained with an FONLL calculation from Chapter 5. A hadronisation fraction $f_{\mathrm{B}^{\pm}}$ of 40.1% is assumed to fix the overall scale of FONLL. The uncertainty of the FONLL computation includes renormalisation/factorisation scales and the uncertainty of the PDF, CTEQ6.6. The two bands differ in the inclusion of a $\pm$ 0.5 GeV/c^2 uncertainty on the b-quark mass, which is now known to within 0.24 GeV/c^2[5]. The LHCb data-points are observed to lie within the bounds of the theoretical prediction.

Figure 7.9 shows the 2010 data distribution as a function of rapidity y^{B}. The distributions are similar in shape and differ only in magnitude, with the $\mathrm{B}^{\pm}$ cross-section peaking at $2 < p^{\mathrm{B}}_{\mathrm{T}} < 4$ GeV/c and $2 < y^{\mathrm{B}} < 4.5$.

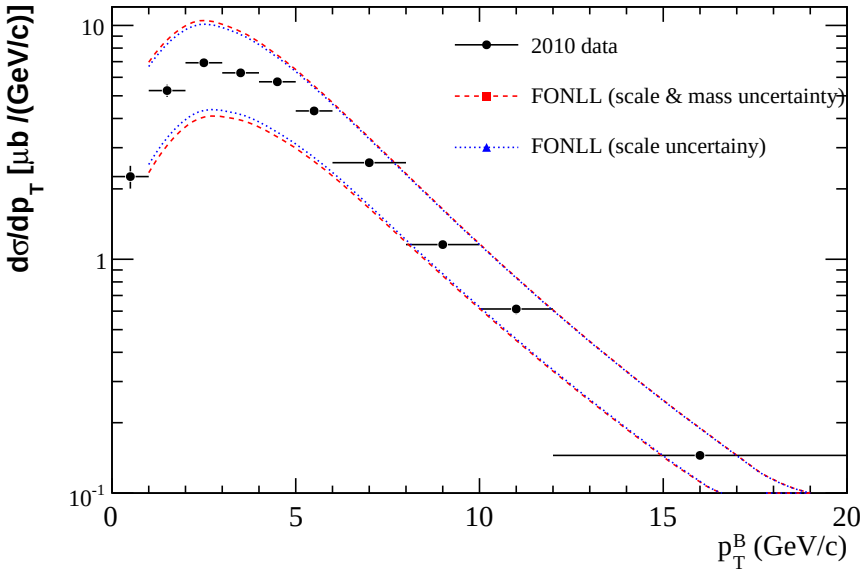

Figure 7.8: Differential $\mathrm{B}^{\pm}$ cross-section with respect to $B^{\pm}$ transverse momentum measured with 2010 data, integrated over $2 < y^{\mathrm{B}} < 4.5$, with FONLL upper and lower limits included as a comparison.

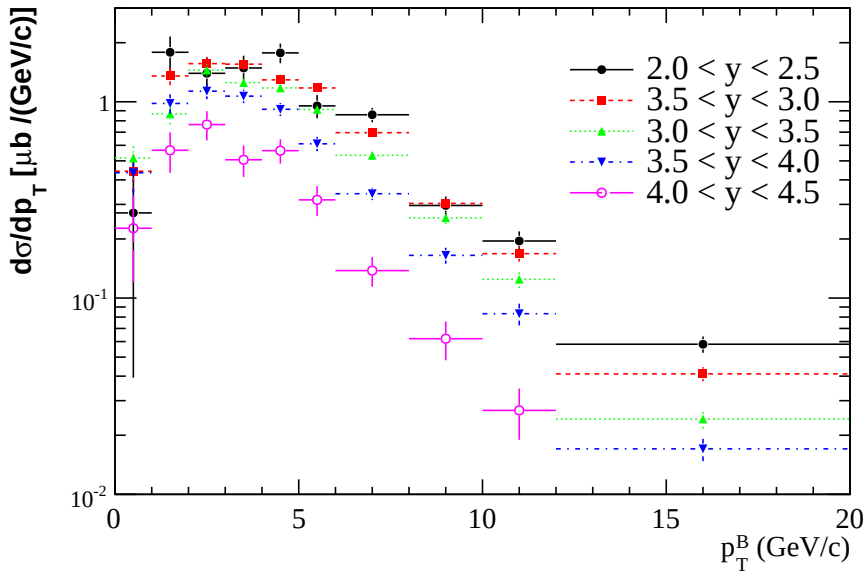

Figure 7.9: Differential $B^{\pm}$ cross-section with respect to $B^{\pm}$ transverse momentum measured with 2010 data, binned in 0.5 unit rapidity intervals.

7.2 Charge Asymmetry of the $B^{\pm}$

We present a measurement of the $B^{\pm}$ charge asymmetry A_{raw}, defined in terms of the extracted signal yields N^{+} and N^{-} as given below:

$$A_{\text{raw}} = \frac{N^{B^-} - N^{B^+}}{N^{B^-} + N^{B^+}} \tag{7.7}$$

The di-μ final states are charge symmetric and any efficiencies relating to muon trigger thresholds cancel between B^{+} and B^{-} decays, therefore we are no longer limited to one configuration of trigger thresholds. Consequently, this extends the 2010 data sample to the full 34.5 pb^{-1} that was recorded throughout the year. In addition, we can take advantage of the data-taking period running from January 2011 to June 2011 that delivered 372 pb^{-1} of pp collisions at $\sqrt{s} = 7$ TeV.

The MC10 data assumes an ideal detector performance, while in practice we expect various detector effects to contribute to a fake asymmetry through the emitted kaon. To compensate for this, we perform measurements of A_{raw} under

opposing magnet polarities as described in Sec. 7.2.1. This leads to a summary of the results for 2010 data and 2011 data, as described in Sec. 7.2.2. To reduce the statistical uncertainty the measurements for these two samples are combined.

Sources of systematic uncertainty are investigated, the largest of which is related to fit strategy. The size of these effects and the attempts to overcome them are described in Sec. 7.2.3.

7.2.1 Polarity-specific signal yields

The same selection and fitting procedure as used for the $B^{\pm}$ cross-section measurement is used to extract yields for the asymmetry A_{raw}. Selected signal candidates from the 2010 data sample are again required to have passed the trigger sequence defined in Chapter 6. The start of 2011 saw significant changes in the trigger strategy for di-μ events, with the majority (83.1%) of stripped signal candidates firing on the L0DiMuon $\rightarrow$ BplusHlt1DiMuonHighMassDecision $\rightarrow$ BplusHlt2DiMuonJPsiDecision trigger sequence. Single muon trigger lines are, in contrast, heavily pre-scaled and make little contribution to the raw data. The di-μ trigger candidates are retained for this analysis.

LHCb has taken collision data under both (MagUp and MagDown) polarities. Table 7.3 summarises the sizes, in integrated luminosity, of MagUp and MagDown samples collected over 2010 and 2011. Extracted signal and background yields, integrated over the fiducial region ($0 < p_{\text{T}}^{\text{B}} < 20$ GeV/c and $2 < y^{\text{B}} < 4.5$), are included in the table. The increase in signal (and background) yield between 2010 and 2011 is approximately consistent with the factor 10 increase in integrated luminosity. Results with the MC10 signal sample are also shown. All signal decays within the LHCb acceptance are included in the MC10(acc.) row, while decays passing the selection cuts (no trigger) are included in the MC10(sel.) row.

The table also appears to show, for the 2011 data sample, a consistency in fitted mean between the MagDown B^+ data and MagUp B^- data, and similarly for the MagDown B^- data and MagUp B^+ data, with a relative shift of ~ 1 MeV. It is clear this systematic shift originates from a geometric effect, which is either physical in nature or arises during reconstruction e.g. from the magnetic field mapping. The relative shift in mean is illustrated for the 2011 MagDown and

Sample	Polarity	Particle	$\int \mathcal{L}$ (pb^{-1})	Yield	Mean (MeV)
2010	MagDown	B^+	17.1 ± 1.7	2530 ± 58	5278.73 ± 0.26
2010	MagDown	B^-	17.1 ± 1.7	2536 ± 58	5278.44 ± 0.26
2010	MagUp	B^+	17.4 ± 1.7	2232 ± 54	5278.84 ± 0.26
2010	MagUp	B^-	17.4 ± 1.7	2122 ± 52	5278.72 ± 0.26
2011	MagDown	B^+	217.4 ± 7.6	25174 ± 173	5276.63 ± 0.072
2011	MagDown	B^-	217.4 ± 7.6	24393 ± 171	5277.54 ± 0.074
2011	MagUp	B^+	155.0 ± 5.4	20971 ± 157	5277.79 ± 0.079
2011	MagUp	B^-	155.0 ± 5.4	20353 ± 154	5276.75 ± 0.078
MC10(sel.)	MagDown	B^+	–	69112 ± 263	–
MC10(sel.)	MagDown	B^-	–	67406 ± 260	–
MC10(acc.)	MagDown	B^+	–	446154 ± 668	–
MC10(acc.)	MagDown	B^-	–	438161 ± 662	–

Table 7.3: $B^{\pm}$ signal yields with corresponding sample types, magnet polarity, integrated luminosity, and fitted (Gaussian) mean. The MC10 sample does not contain any luminosity information, and the raw signal yields are extracted using truth-matching instead of a Gaussian fit.

2011 MagUp samples in Figures 7.10 and 7.11 respectively.

The 2010 MagUp and MagDown data samples are roughly equal in integrated luminosity and signal yields. Combining the samples, in an attempt to cancel geometric asymmetries, therefore involves a simple summation of charge-specific signal yields over both polarities.

For the 2011 data sample, there is a 40% excess in luminosity of MagDown data compared with MagUp data. Applying the summation of charge-specific yields in a similar way to the 2010 data sample will not result in a complete cancellation of geometrical asymmetries. The MagUp N^+ and N^- signal yields are scaled up based on the ratio of signal ($N^+ + N^-$) in MagDown data to signal ($N^+ + N^-$) in MagUp data, which is calculated to be 1.20. The discrepancy between this calculated ratio and the ratio in luminosities (1.40) may be due to differing configurations of the trigger between MagUp and MagDown data-taking periods.

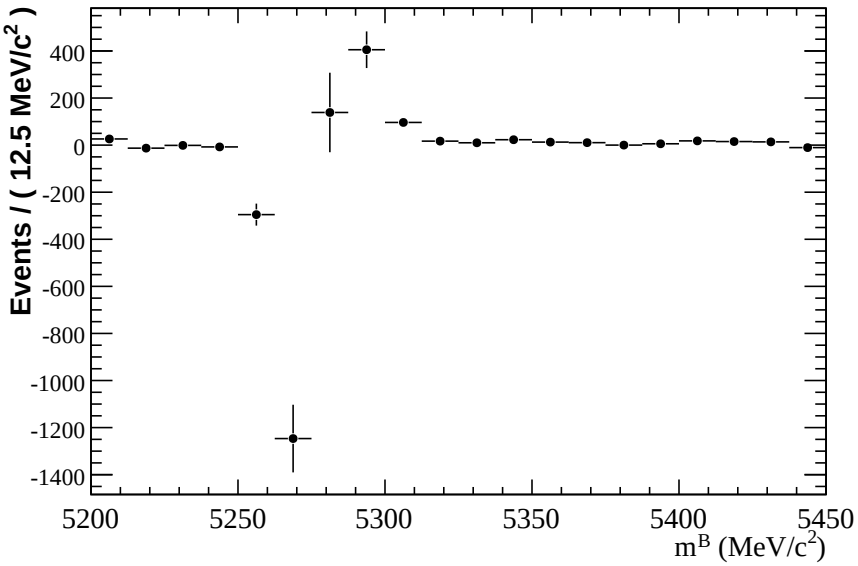

Figure 7.10: Difference in signal yields $B^- - B^+$, as function of $B^{\pm}$ invariant mass, for 2011 MagDown data sample.

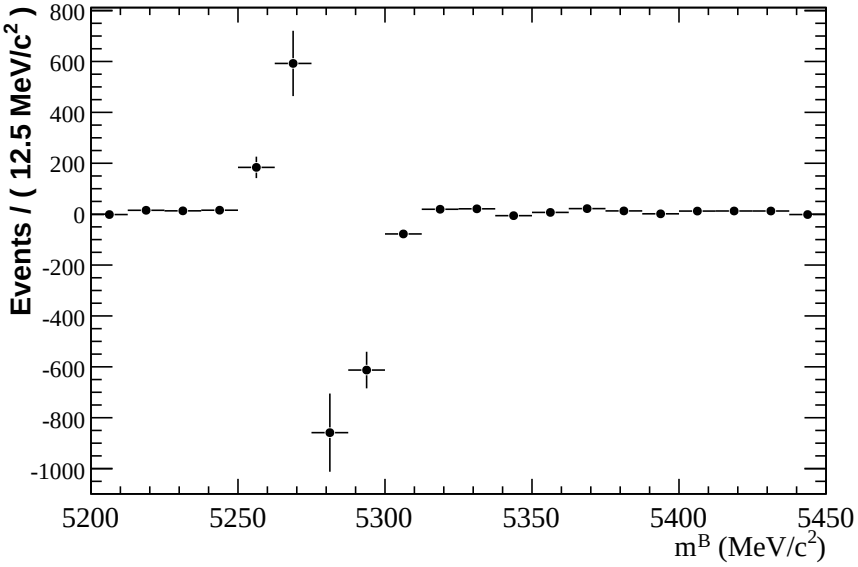

Figure 7.11: Difference in signal yields $B^- - B^+$, as function of $B^{\pm}$ invariant mass, for 2011 MagUp data sample.

7.2.2 Results

The raw asymmetries A_{raw} are calculated per magnet polarity and then combined as described in the previous section. Table 7.4 summarises the results for the 2010 and 2011 data samples and also for the MC10 sample.

The two data samples — 2010 and 2011 — separately show evidence of a negative A_{raw}, which is consistent with the hypothesis that one or more mechanisms are contributing to an excess of detected $\text{B}^+ \to \text{J}/\psi\text{K}^+$ decays. Asymmetries for 2011 data are particularly large in magnitude, exceeding the levels predicted by $A_{\text{sel/acc}}$ (MC10) and A_{gen} (MC10). Measurements of A_{raw} between MagUp and MagDown for 2011 data show good agreement within the statistical uncertainty, which indicates that any fake asymmetry related to geometric uncertainties may be limited. Combining the yields from 2010 and 2011 further improves on the statistical uncertainty, the results of which is shown as "2010+2011" in the table.

Sample	Polarity	A_{raw} (%)
2010	MagDown	$+0.13 \pm 1.63$
2010	MagUp	-2.54 ± 1.72
2010	Combined	-1.10 ± 1.18
2011	MagDown	-1.58 ± 0.49
2011	MagUp	-1.50 ± 0.53
2011	Combined	-1.54 ± 0.36
2010+2011	Combined	-1.50 ± 0.35
$A_{\text{sel/acc}}$ (MC10)	MagDown	-1.25 ± 0.27
A_{gen} (MC10)	MagDown	-0.90 ± 0.11

Table 7.4: Raw asymmetries obtained from 2010 and 2011 collision samples, split by magnet polarity. MC10 asymmetries at the generation (6.3) and selection (6.7) level are included as a comparison.

Distributions of A_{raw} with respect to p_{T}^{B}, y^{B}, E^{K} and p_{T}^{K} are shown for the 2011 sample in Figures 7.12, 7.13, 7.14 and 7.15 respectively. The bin sizes in each plot are chosen to give roughly equal yields over the entire range. In general the discrepancy in A_{raw} between magnet polarities is small but does increase at high ($y^{\text{B}} > 3.5$) rapidity. The cancellation of geometric asymmetries will be discussed in detail in the next section.

Comparisons between the (2010+2011) data and MC10 are shown as a function of

$p_{\mathrm{T}}^{\mathrm{B}}$, y^{B}, E^{K} and $p_{\mathrm{T}}^{\mathrm{K}}$ in Figures 7.16, 7.17, 7.18 and 7.19 respectively. At this level of statistical uncertainty, it is difficult to determine whether the data reproduces the $p_{\mathrm{T}}^{\mathrm{B}}$ and y^{B} dependence of A_{gen} that is identified with a production asymmetry (6.2 and 6.3), though there is an indication of an increased $-A_{\mathrm{raw}}$ at high $p_{\mathrm{T}}^{\mathrm{B}}$. Over the kaon kinematics, the (2010+2011) data dependence is approximately flat, which indicates an insensitivity of the kaons to an interaction asymmetry. The large statistical uncertainty in the first ($0 \rightarrow 1$ GeV/c) $p_{\mathrm{T}}^{\mathrm{K}}$ bin is due to a changed stripping configuration, resulting in an increase in the $p_{\mathrm{T}}^{\mathrm{K}}$ threshold from > 500 MeV/c in 2010 to > 1 GeV/c in 2011.

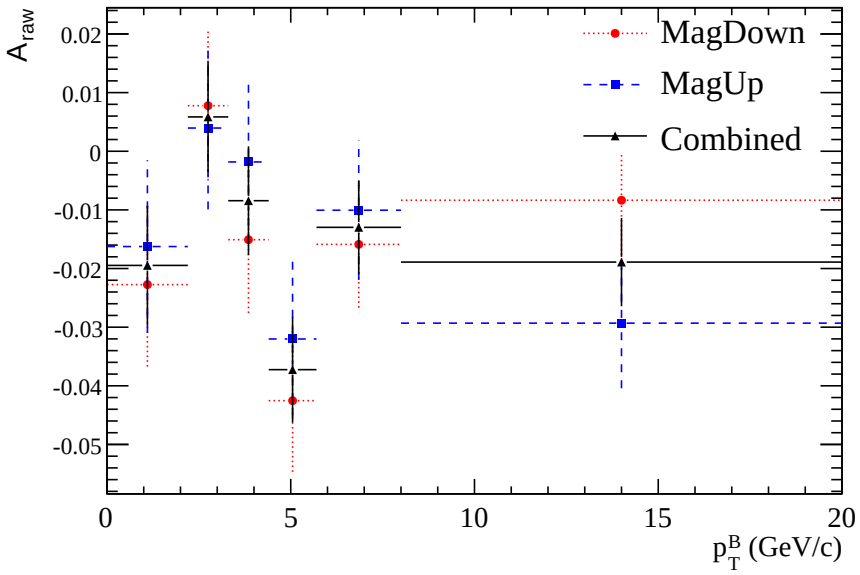

Figure 7.12: A_{raw} of 2011 data for MagUp (red dashed), MagDown (blue dashed) and combined (black solid), as a function of $p_{\mathrm{T}}^{\mathrm{B}}$.

7.2.3 Systematic uncertainties

The majority of systematic uncertainties associated to the $\mathrm{B}^{\pm}$ cross-section measurement cancel for the A_{raw} measurement. Non-cancellation of geometric asymmetries and mass fit instabilities are expected to distort the measurement of A_{raw}. An analysis of these contributions is discussed below.

In $\mathrm{B}^{\pm} \rightarrow \mathrm{J}/\psi\mathrm{K}^{\pm}$ decays, geometric asymmetries can manifest in the detection of the charged kaon. An asymmetry in, for example, the T-station efficiency

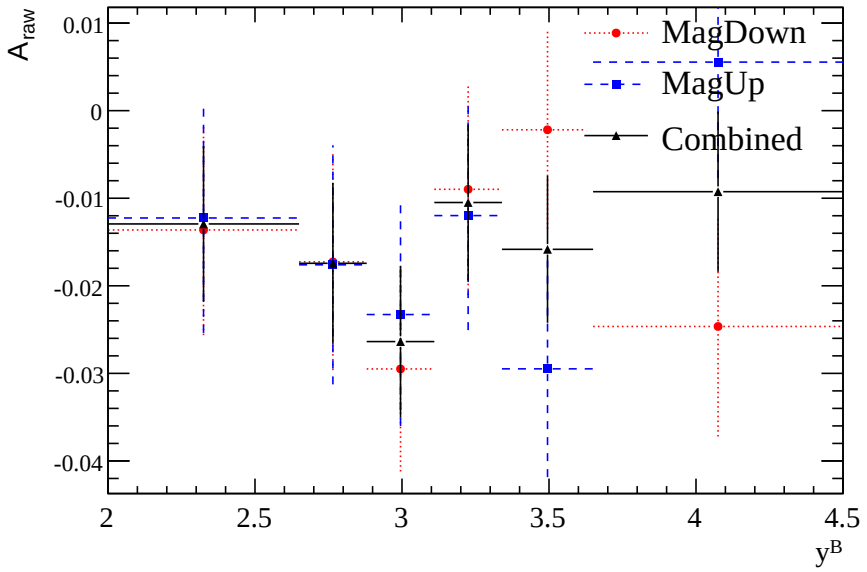

Figure 7.13: A_{raw} of 2011 data for MagUp (red dashed), MagDown (blue dashed) and combined (black solid), as a function of y^{B}.

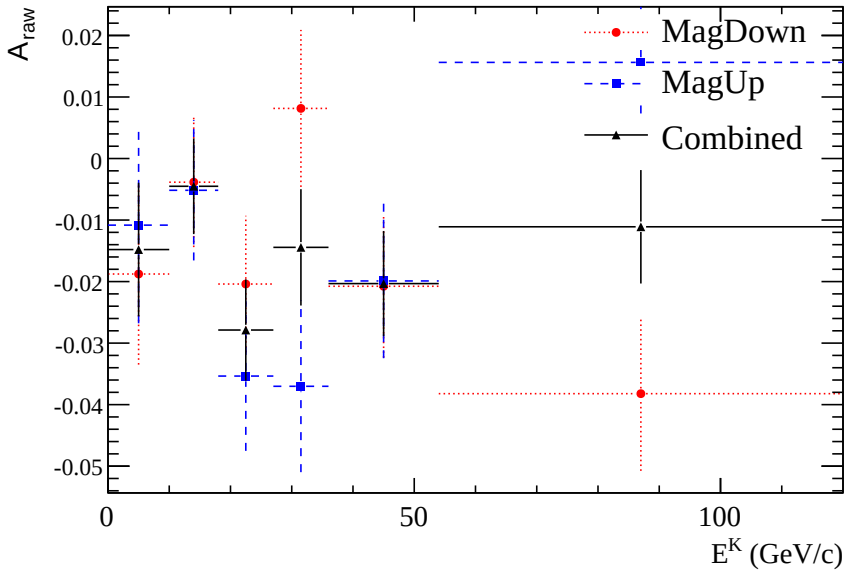

Figure 7.14: A_{raw} of 2011 data for MagUp (red dashed), MagDown (blue dashed) and combined (black solid), as a function of E^{K}.

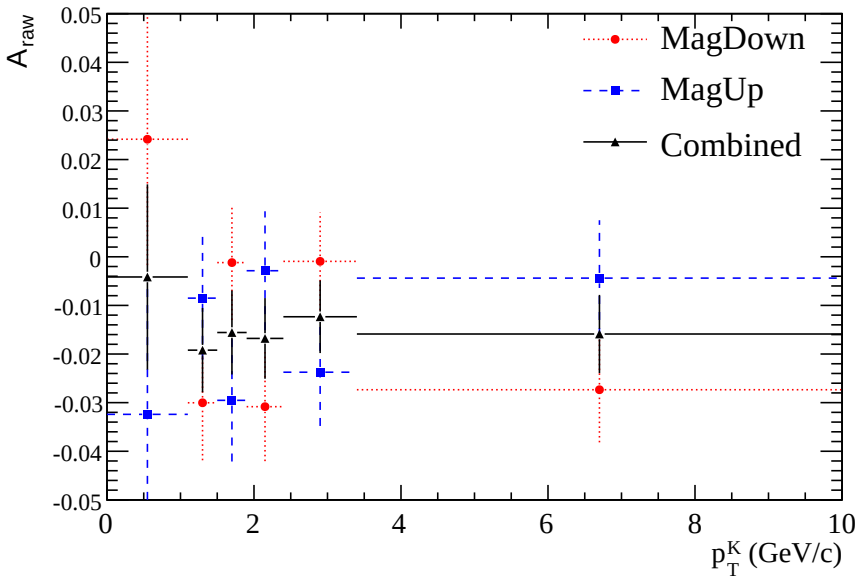

Figure 7.15: A_{raw} of 2011 data for MagUp (red dashed), MagDown (blue dashed) and combined (black solid), as a function of p_{T}^{K}.

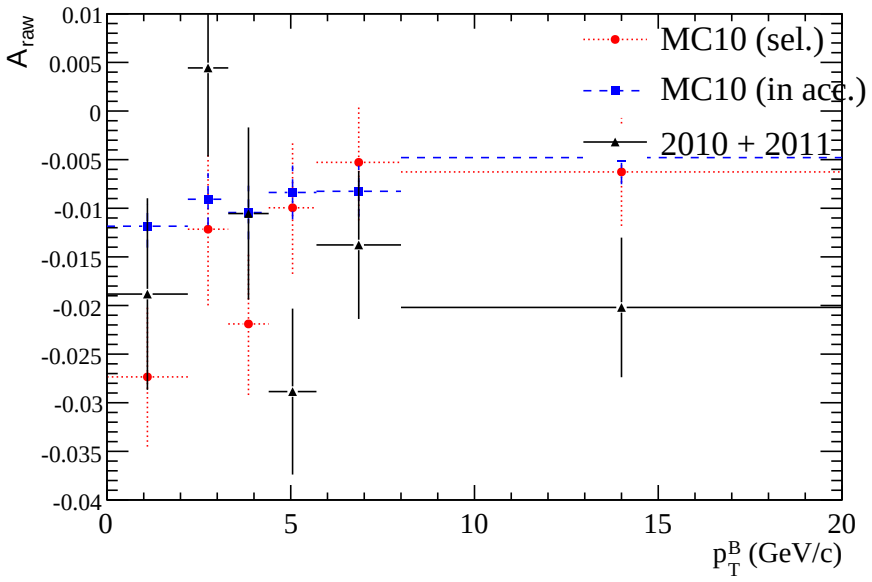

Figure 7.16: A_{raw} of 2011 data with combining polarities (black solid) alongside MC10 predictions of $A_{\text{sel/acc}}$ (red) dashed and A_{gen} (blue dashed), as a function of p_{T}^{B}.

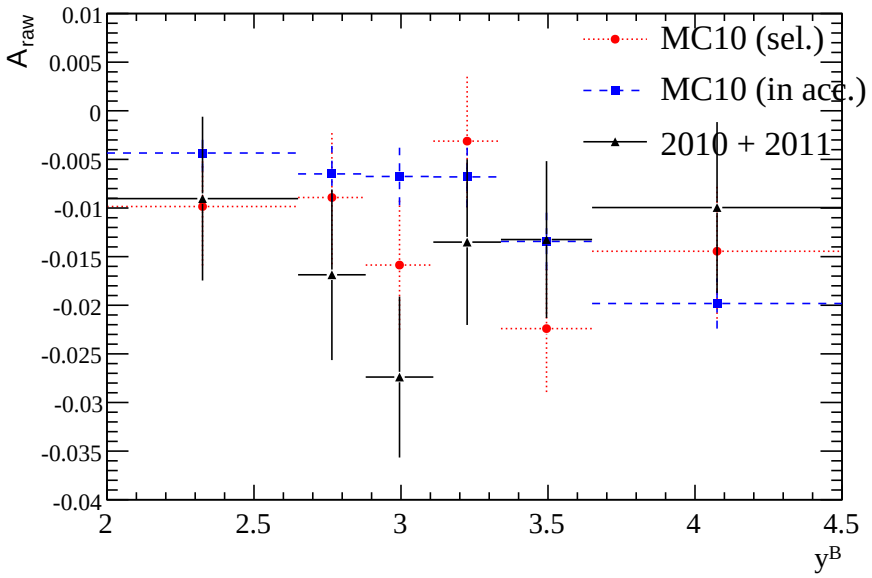

Figure 7.17: A_{raw} of 2011 data with combining polarities (black solid) alongside MC10 predictions of $A_{\text{sel/acc}}$ (red) dashed and A_{gen} (blue dashed), as a function of y^{B}.

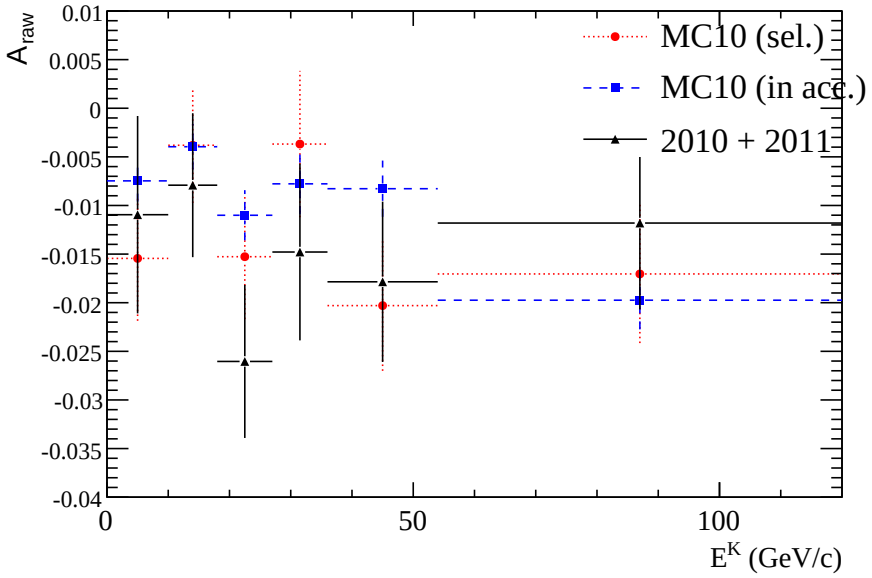

Figure 7.18: A_{raw} of 2011 data with combining polarities (black solid) alongside MC10 predictions of $A_{\text{sel/acc}}$ (red) dashed and A_{gen} (blue dashed), as a function of E^{K}.

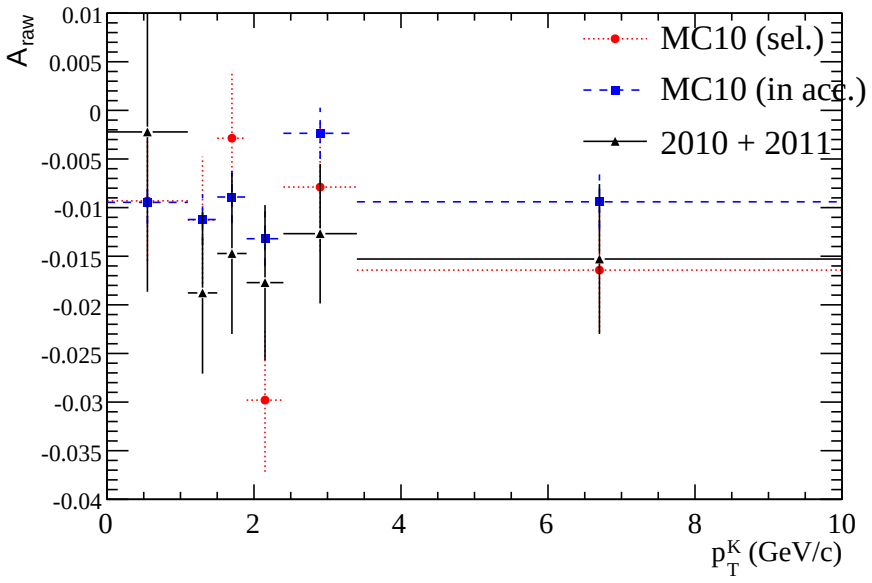

Figure 7.19: A_{raw} of 2011 data with combining polarities (black solid) alongside MC10 predictions of $A_{\text{sel/acc}}$ (red) dashed and A_{gen} (blue dashed), as a function of p_{T}^{K}.

between the left and right hemispheres of the detector can result in a geometric asymmetry of the kaon. It is expected that the left-right asymmetry of the T-station, and any other detector instrument in LHCb, are expected to be small enough that the geometric asymmetry contribution to A_{raw} cancels for opposing polarities.

There are some local regions in momentum space where, for a given magnet polarity, a K^+ (K^-) has 100% acceptance whereas a K^- (K^+) has 0% acceptance. These regions of large raw asymmetry are identified as part of a study into time-integrated CP violation of $\text{D}^0 \to \text{HH}$ decays at LHCb [83].

One such region coincides with the outer boundaries of the detector acceptance, where for example low momentum π^+ particles are swept further out from the detector by the magnet, while π^- particles are swept back in to the detector. Cutting on the x-coordinate momentum p_x of the $\pi^{\pm}$ as shown below excludes these boundary regions of asymmetry:

$$| p_x | \leq \alpha(p_z - p_0) \tag{7.8}$$

The degree of exclusion can be varied through the cut parameters α and p_0, which for this analysis are chosen to be 0.317 and 2400 MeV/c respectively.

Another region of large local asymmetry coincides with the beam pipe section at the T-stations. This corresponds to outward-moving tracks of zero vertical momentum that are deflected inwards by the magnetic field and pass through the un-instrumented region of the beam pipe instead of a T-station. Satisfying any one of the equations below excludes this region of large asymmetry:

$$| p_y/p_z | > 0.02 \tag{7.9}$$

$$p_x < p_1 - \beta_1 p_z \text{ for } | p_y/p_z | < 0.02 \tag{7.10}$$

$$p_x > p_2 - \beta_2 p_z \text{ for } | p_y/p_z | < 0.02 \tag{7.11}$$

If these fiducial cuts are not applied then any significant difference in the kinematic distributions between K^+ and K^-, arising at trigger or reconstruction levels, can manifest as potentially large second-order contributions to A_{raw}. Combining the polarities may then result in only a partial cancellation of these geometric asymmetries. It has been the continuing goal of this analysis to minimise any potential bias between K^+ and K^- distributions, through loose selection cuts and avoidance of the hadron trigger. It is nevertheless useful to test the A_{raw} stability with and without these fiducial cuts.

Using the 2011 data sample, we find that the majority of signal (and background) candidates pass the fiducial cuts, with a retention rate of 94%. A comparison of A_{raw} with and without the fiducial cuts are shown in Table 7.5. The difference in A_{raw} between the MagDown and MagUp polarities increases slightly but remains well within the statistical uncertainty. The central (combined) value also remains stable.

The $B^{\pm}$ reconstructed mass range is varied from $5.20 < m_B < 5.45$ GeV/c^2 to

$5.15 < m_B < 5.40$ GeV/c^2 to test the stability of the fit. As shown in Table 7.6 no significant change is observed in A_{raw} for MagUp, MagDown or the central value. As a further test on the fit stability, a Crystal Ball function is used instead of a single Gaussian to describe the signal. An illustration of these fits is shown in Figures 7.20 and 7.21, and a comparison of A_{raw} in Table 7.6 . There is a significant discrepency in A_{raw} between the fit methods for MagDown, and consequently for the central value. A systematic uncertainty of 0.5% is assigned to the A_{raw} single Gaussian result based on this difference.

Sample	Polarity	A_{raw} (%)
Without fiducial cuts		
2011	MagDown	-1.58 ± 0.49
2011	MagUp	-1.50 ± 0.53
2011	Combined	-1.54 ± 0.36
With fiducial cuts		
2011	MagDown	-1.38 ± 0.50
2011	MagUp	-1.69 ± 0.54
2011	Combined	-1.53 ± 0.37

Table 7.5: Comparison of bin-averaged A_{raw} with and without fiducial cuts.

7.2.4 Production asymmetry

A preliminary measurement of the $B^{\pm}$ production asymmetry can now be given, based on the measured charge asymmetry of $B^{\pm} \to J/\psi K^{\pm}$ decays from accumulated collision data (described in the previous section) and the predicted kaon interaction asymmetry from MC10 data (discussed in the previous chapter). This is more of an estimate as it relies on a rather large assumption that the Monte Carlo data correctly reproduces the kaon interaction asymmetry through the detector. It is necessary to assign a 1% systematic to the measurement of $A_{\text{sel/acc}}$ (6.7), which quantifies the kaon interaction asymmetry ($A^{\text{K}}_{\text{int}}$) in MC10 data:

Sample	Polarity	A_{raw} (%)
Single Gaussian ($5.20 < \text{m}_B < 5.45$ GeV/c^2)		
2011	MagDown	-1.58 ± 0.49
2011	MagUp	-1.50 ± 0.53
2011	Combined	-1.54 ± 0.36
Single Gaussian ($5.15 < \text{m}_B < 5.40$ GeV/c^2)		
2011	MagDown	-1.62 ± 0.49
2011	MagUp	-1.40 ± 0.53
2011	Combined	-1.51 ± 0.36
Crystal Ball (Un-constrained)		
2011	MagDown	-0.78 ± 0.49
2011	MagUp	-1.34 ± 0.53
2011	Combined	-1.06 ± 0.36
Crystal Ball (MC10-constrained parameters)		
2011	MagDown	-1.61 ± 0.49
2011	MagUp	-1.37 ± 0.53
2011	Combined	-1.49 ± 0.36

Table 7.6: Comparison of bin-averaged A_{raw} between different $\text{B}^{\pm}$ mass ranges and different fit methods.

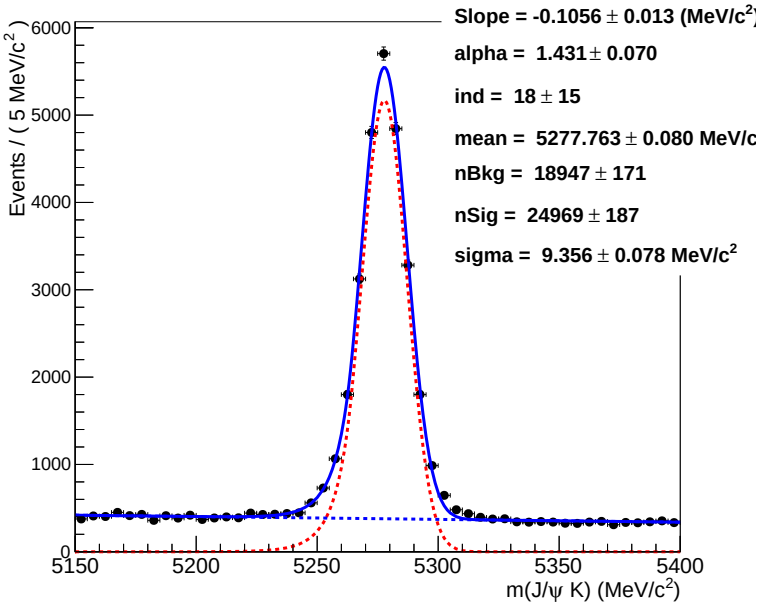

Figure 7.20: $B^{\pm}$ invariant mass distribution (black data-points) of selected candidates from 2011 MagDown sample, with Crystal Ball function (red dashed), linear function (blue dashed) and full fit (blue solid) overlaid. The parameter definitions of the Crystal Ball function, referenced from (7.2), are the mean ($\bar{x}$), ind (n), alpha (α) and sigma (σ).

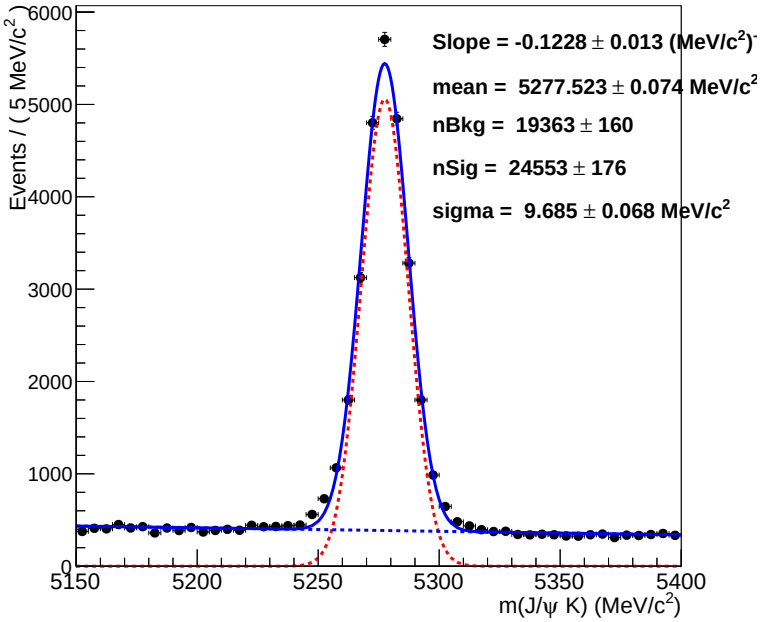

Figure 7.21: $B^{\pm}$ invariant mass distribution (black data-points) of selected candidates from 2011 MagDown sample, with single Gaussian (red dashed), linear function (blue dashed) and full fit (blue solid) overlaid.

$$\begin{aligned} A_{\text{int}}^{\text{K}} &= A_{\text{sel/acc}} \\ &= [-0.35 \pm 0.24 \text{ (stat.)} \ \pm 1.0 \text{ (sys.)}]\% \end{aligned} \tag{7.12}$$

The investigation of systematic uncertainties for the A_{raw} asymmetry, measured using collision data, is also only preliminary. We use the A_{raw} measurement obtained with a single Gaussian fit the $\text{B}^{\pm}$ mass, no fiducial cuts and which uses data accumulated over both magnet polarities and data-taking years (2010 and 2011). A 0.5% systematic uncertainty is assigned, based on the inaccuracies of the $\text{B}^{\pm}$ fit function:

$$A_{\text{raw}} = [-1.54 \pm 0.36 \text{ (stat.)} \ \pm 0.5 \text{ (sys.)}]\% \tag{7.13}$$

Then adapting the parameters of (5.10) to the current definitions and re-arranging:

$$\begin{aligned} A_{\text{p}}^{B} &= A_{\text{raw}} - A_{\text{int}}^{\text{K}} - A_{\text{CP}} \\ &= [-1.54 \pm 0.36 \pm 0.5]\% \\ &\quad [+0.35 \pm 0.24 \pm 1.0]\% \\ &\quad [-0.9 \pm 0.8]\% \\ &= [-2.09 \pm 1.20 \pm 0.8(\text{CP})]\% \end{aligned} \tag{7.14}$$

where the uncertainty related to the current CP-asymmetry measurement (0.8%) remains separate. The result is in good agreement with the two existing measurements for $\text{B}^{\pm}$ and B^{0} production asymmetry at LHCb, given in Table 5.1.

7.3 Summary

I have presented measurements of the $B^{\pm}$ cross-section and production asymmetry, using data collected by the LHCb detector in 2010 and 2011. Using 27.6 pb^{-1} of pp collisions at a centre-of-mass energy 7 TeV, a $B^{\pm}$ cross-section of [41.6 $\pm$ 0.6 (stat.) $\pm$ 3.0 (sys.) $\pm$ 4.2 (lumi.)] μb is obtained in the rapidity region 2 to 4.5. The differential cross-section shows good agreement with predictions obtained using the FONLL method. Using a larger data-set containing 371.1 pb^{-1} of pp collisions at a centre-of-mass energy 7 TeV, a charge asymmetry of [-1.54 ± 0.36 (stat.) $\pm$ 0.5 (sys.)]% is measured for $B^{\pm} \rightarrow J/\psi K^{\pm}$ decays. This is equivalent to a $B^{\pm}$ production asymmetry of [$-2.09 \pm 1.20 \pm 0.8$ (CP)]%.

Chapter 8

Conclusions

The start-up of the LHC in 2009 heralded an exciting time for particle physicists. LHCb has already made significant progress in the measurement of some physics parameters, including the ϕ_s phase (using $B_s \rightarrow J/\psi\phi$ decays) [84], forward backward asymmetry A_{FB} (using $B_d \rightarrow K^*\mu\mu$ decays) [85] and ΔA_{CP} [83] asymmetry differences (using charm decays). While it remains to be seen whether or not ϕ_s and A_{FB} converge with Standard Model predictions, ΔA_{CP} provides an interesting case for possible new physics effects.

LHCb relies on two RICH counters for separation and identification of hadrons. At the time of start-up of the LHC, the RICH detectors were fully commissioned with HPDs and ready to detect Cherenkov photons produced from charged particles. HPDs are tested regulary for ion feedback, providing reliable estimates of the HPD lifetime. Preparations are under way that will allow ion feedback to be measured using collision data, the first step of which has involved a comparison of ion feedback results under different pixel resolutions.

A cross-section determination of the light $B^{\pm}$ meson provides a powerful test of the accuracy with which we model perturbative and non-perturbative QCD processes. This measurement made use of the decay $B^{\pm} \rightarrow J/\psi K^{\pm}$, which has a clean experimental signature and large branching fraction. An analysis of Monte Carlo data yields a total signal detection efficiency of $[12.0 \pm 0.1]\%$ for $B^{\pm}$ mesons in the fiducial region ($0 < p_T^B < 20$ GeV/c) and ($2 < y^B < 4.5$). The contributing factors relate to geometric acceptance, reconstruction/selection, and trigger effects. An

analysis of pp collision data recorded in 2010 yields a cross-section measurement, in the equivalent fiducial region, of $\sigma_{B^\pm} = [41.6 \pm 0.6$ (stat.) ± 3.0 (sys.) $\pm$ 4.2 (lumi.)] μb. A comparison of the differential cross-section with an FONLL QCD calculation shows good agreement between the two data sets.

A determination of the $B^\pm$ charge asymmetry in the fiducial region using $B^\pm \to J/\psi K^\pm$ decays has also been performed. From an analysis of Monte Carlo data, charge asymmetries related to detector effects seem to be small. B-meson production asymmetries are allowed for in the Pythia fragmentation model, and this is observed in the Monte Carlo sample to be $[-0.90 \pm 0.11]$%. An analysis of collision data taken in 2010 and 2011 further confirmed the presence of a production asymmetry and possibly a small CP asymmetry, yielding $A_{\text{raw}} = [-1.54 \pm 0.36]$%. The results are consistent when split between magnet polarities, an indication that geometric asymmetries are limited. This is equivalent to an estimate of the $B^\pm$ production asymmetry at LHCb, of $[-2.09 \pm 1.20 \pm 0.8(\text{CP})]$%.

Bibliography

[1] A.D. Sakharov. Violation of CP Invariance, c Asymmetry, and Baryon Asymmetry of the Universe. *Pisma Zh.Eksp.Teor.Fiz.*, 5:32–35, 1967.

[2] J.H. Christenson, J.W. Cronin, V.L. Fitch, and R. Turlay. Evidence for the $\pi\pi$ Decay of the K(2)0 Meson. *Phys.Rev.Lett.*, 13:138–140, 1964.

[3] Makoto Kobayashi and Toshihide Maskawa. CP Violation in the Renormalizable Theory of Weak Interaction. *Prog.Theor.Phys.*, 49:652–657, 1973.

[4] L.M. Lederman. The discovery of the Upsilon, bottom quark, and B mesons. *Stanford 1992, The rise of the standard model*, 1992.

[5] K. Nakamura et al. Review of particle physics. Particle Data Group. *Phys.Lett.*, G 37:1, 2010.

[6] M. Khabibullin. Latest oscillation results from T2K. 2011.

[7] T. Blum, T. Doi, M. Hayakawa, T. Izubuchi, and N. Yamada. Determination of light quark masses from the electromagnetic splitting of pseudoscalar meson masses computed with two flavors of domain wall fermions. *Phys.Rev.*, D76:114508, 2007.

[8] S. Weinberg. A model of leptons. *Phys.Rev.*, 19:1264, 1967.

[9] C.S. Wu, E. Ambler, R.W. Hayward, D.D. Hoppes, and R.P. Hudson. Experimental test of parity conservation in beta decay. *Phys.Rev.*, 105:1413–1414, 1957.

[10] A Courtoy. The role of the running coupling constant in the unveiling of the hadronic structure. Technical Report arXiv:1111.6096, Nov 2011.

[11] Nicola Cabibbo. Unitary Symmetry and Leptonic Decays. *Phys.Rev.Lett.*, 10:531–533, 1963.

[12] S.L. Glashow, J. Iliopoulos, and L. Maiani. Weak Interactions with Lepton-Hadron Symmetry. *Phys.Rev.*, D2:1285–1292, 1970.

[13] J.E. Augustin et al. Discovery of a Narrow Resonance in e^+e^- Annihilation. *Phys.Rev.Lett.*, 33:1406–1408, 1974.

[14] J.J. Aubert et al. Experimental Observation of a Heavy Particle J. *Phys.Rev.Lett.*, 33:1404–1406, 1974. Technical report 96.

[15] T. Kobayashi and Z.Z. Xing. Remarks on the Kielanowski parametrization of the Kobayashi-Maskawa matrix. *Mod.Phys.Lett.*, A11:2531–2537, 1996.

[16] J. Charles et al. CP violation and the CKM matrix: Assessing the impact of the asymmetric B factories. *Eur.Phys.J.*, C41:1–131, 2005.

[17] Bernard Aubert et al. Observation of direct CP violation in $B^0 \to K^+\pi^-$ decays. *Phys.Rev.Lett.*, 93:131801, 2004.

[18] Victor Mukhamedovich Abazov et al. Measurement of the anomalous like-sign dimuon charge asymmetry with 9 fb^{-1} of $p\bar{p}$ collisions. *Phys.Rev.*, D84:052007, 2011. Submitted to Phys. Rev. D.

[19] I. Adachi, I. Aihara, H. Asner, D.M. Aulchenko, V. Aushev, et al. Precise measurement of the CP violation parameter $\sin 2\phi_1$ in $B^0 \to (c\bar{c})K^0$ decays. 2012.

[20] Alexander. M et al. Private communication.

[21] A. Alves, Augusto, et al. The LHCb Detector at the LHC. *JINST*, 3:S08005, 2008.

[22] Manuel Schiller. Results from LHCb: Prompt V0 production. *PoS*, DIS2010:137.

[23] J Van Tilburg and M Merk. *Track simulation and reconstruction in LHCb. oai:cds.cern.ch:885750.* PhD thesis, Vrije Univ. Amsterdam, 2005.

[24] S Borghi. Performance of the Tracking System at the LHCb Experiment. Dec 2010. LHCb-TALK-2010-094.

[25] Nicholas Styles and P J Clark. *RICH detector time alignment and studies of CP violation in the decay $B_s^0 \to \phi\phi$ at the LHCb experiment.* PhD thesis, Edinburgh, University of Edinburgh, 2009.

[26] D Pinci and A Sarti. Study of the MWPC gas gain behaviour as a function of the gas pressure and temperature. Technical Report LHCb-2005-079. CERN-LHCb-2005-079, CERN, Geneva, Oct 2005.

[27] D Pinci. *A triple-GEM detector for the muon system of the LHCb experiment.* PhD thesis, Cagliari U., 2003.

[28] M Adinolfi et al. Performance of the LHCb RICH photo-detectors and readout in a system test using charged particles from a 25 ns-structured beam. *Nucl. Instrum. Methods Phys. Res., A*, 603(3):287–293, 2009.

[29] C Blanks, F Soomro, and J Nardulli. The Laser Alignment and Monitoring System for the LHCb RICH detectors. Technical Report LHCb-PUB-2011-014. CERN-LHCb-PUB-2011-014, CERN, Geneva, Jun 2011. LHCb-INT-2010-039.

[30] R Antunes-Nobrega et al. *LHCb trigger system: Technical Design Report.* Technical Design Report LHCb. CERN, Geneva, 2003.

[31] J Albrecht, L de Paula, A Prez-Calero Yzquierdo, and F Teubert. Commissioning and Performance of the LHCb HLT1 muon trigger. Technical Report LHCb-PUB-2011-006. CERN-LHCb-PUB-2011-006. LHCb-INT-2010-042, CERN, Geneva, Feb 2011.

[32] G. Barrand et al. GAUDI - A software architecture and framework for building HEP data processing applications. *Comput. Phys. Commun.*, 140:45–55, 2001.

[33] Torbjorn Sjostrand, Stephen Mrenna, and Peter Z. Skands. PYTHIA 6.4 Physics and Manual. *JHEP*, 0605:026, 2006.

[34] S. Agostinelli and J. Allison. Geant4—a simulation toolkit. *Nuclear Instruments and Methods in Physics Research Section A: Accelerators, Spectrometers, Detectors and Associated Equipment*, 506(3):250 – 303, 2003.

[35] R. Aaij et al. Absolute luminosity measurements with the LHCb detector at the LHC. *JINST*, 7:P01010, 2012.

[36] S van der Meer. Calibration of the effective beam height in the isr. oai:cds.cern.ch:296752. Technical Report CERN-ISR-PO-68-31. ISR-PO-68-31, CERN, Geneva, 1968.

[37] H Burkhardt and P Grafstrm. Absolute luminosity from machine parameters. oai:cds.cern.ch:1056691. Technical Report LHC-PROJECT-Report-1019. CERN-LHC-PROJECT-Report-1019, 2007.

[38] M Ferro-Luzzi. Proposal for an absolute luminosity determination in colliding beam experiments using vertex detection of beam-gas interactions. *Nucl. Instrum. Methods Phys. Res., A*, 553(CERN-PH-EP-2005-023. 3):388–399. 17 p, May 2005.

[39] Andreas Schopper. Status of lhcb. Oct 2011. Linked to LHCb-TALK-2011-096.

[40] Stephan Eisenhardt. Production and tests of Hybrid Photon Detectors for the LHCb RICH detectors. *Nucl.Instrum.Meth.*, A595:142–145, 2008.

[41] L Carson, A Pickford, and P Soler. Measurement of the Photoelectron Detection Efficiency of the HPD Anode. Technical Report LHCb-2009-038. CERN-LHCb-2009-038, CERN, Geneva, Nov 2009.

[42] Fitzpatrick. C. Rich time alignment. 2010.

[43] G Aglieri-Rinella, T Gys, D Piedigrossi, and A Van Lysebetten. Performance studies of pixel hybrid photon detectors for the LHCb RICH counters. *Nucl. Phys. B, Proc. Suppl.*, 150:285–289, 2006.

[44] Graham Young-Min Kim and F Muheim. *RICH Particle Identification at the Present and Future LHCb Experiment . oai:cds.cern.ch:1370447.* PhD thesis, Edinburgh U., 2011.

[45] S. Eisenhardt. Private communication.

[46] T. Blake et al. Private communication.

[47] E. Ben-Haim. *The b Quark Fragmentation Function, From LEP to TeVatron.* PhD thesis, 2004.

[48] C. Gwenlan. Combined HERA Deep Inelastic Scattering Data and NLO QCD Fits. *Nucl.Phys.Proc.Suppl.*, 191:5–15, 2009.

[49] P Nason and G Ridolfi. Bottom Production. (hep-ph/0003142), 2000.

[50] C. Peterson et al. *Phys. Rev. D*, D:27, 1983.

[51] T. Sjostrand et al. PYTIHA 6.4, Physics and Manual. Technical Report FERMILAB-PUB-06-052-CD-T, March 2006. hep-ph/0603175.

[52] V.N. Gribov and N Lipatov, L. *Sov.J.Nucl.Phys*, 15:438, 1972.

[53] P. Altarelli and G Parisi. *Nucl. Phys. B*, 126:298, 1977.

[54] Dokshitzer. Yu. L. *Sov.Phys. JETP*, 46:641, 1977.

[55] A. Abulencia et al. Measurement of the $B^{\pm}$ production cross-section in $p\bar{p}$ collisions at $\sqrt{s} = 1.96$ TeV. *Phys.Rev.*, D75:012010, 2007.

[56] J. Pumplin, D.R. Stump, J. Huston, H.L. Lai, Pavel M. Nadolsky, et al. New generation of parton distributions with uncertainties from global QCD analysis. *JHEP*, 0207:012, 2002.

[57] V. Khachatryan et al. Measurement of the $B^{\pm}$ Production Cross Section in pp Collisions at $\sqrt{s} = 7$ TeV. *Phys.Rev.Lett.*, 106:112001, 2011.

[58] R. Aaij et al. Measurement of $\sigma(pp \to b\bar{b}X)$ at $\sqrt{s} = 7$ TeV in the forward region. *Phys.Lett.*, B694:209–216, 2010.

[59] W. K. Tung et al. Heavy quark mass effects in deep inelastic scattering and global QCD analysis. *JHEP*, 02:053, 2007.

[60] J.M Campbell and Ellis. K. MCFM— Monte Carlo for FeMtobarn processes *http://mcfm.fnal.gov/*.

[61] D Asner and Sw Banerjee. Averages of b-hadron, c-hadron, and tau-lepton properties. Technical Report arXiv:1010.1589, Oct 2010.

[62] R. Aaij et al. Measurement of the $B^{\pm}$ production cross-section at LHCb. Jul 2011. LHCb-ANA-2011-050.

[63] R. W. Lambert and F Muheim. *LHCb Hybrid Photon Detectors and Sensitivity to Flavour Specific Asymmetry in Neutral B-Meson Mixing. oai:cds.cern.ch:1154988.* PhD thesis, Edinburgh U., 2009.

[64] T. Sjostrand and Peter Z. Skands. Multiple interactions and the structure of beam remnants. *JHEP*, 0403:053, 2004.

[65] R. Aaji et al. Measurement of direct CP violation in charmless charged two-body B decays at LHCb. Apr 2011. LHCb-ANA-2011-023.

[66] R. Aaji et al. Charmless charged two-body B decays at LHCb with 2011 data. Jul 2011. LHCb-ANA-2011-060.

[67] K. Sakai and T. Kawasaki. Search for CP-violating charge asymmetry in $B^+ \to J/\psi\ K^\pm$ decays. *Conf.Proc.*, C100901:317–320, 2010.

[68] B.R. Ko et al. Search for CP Violation in the Decays $D^0 \to K^0_S P^0$. *Phys.Rev.Lett.*, 106:211801, 2011.

[69] S Miglioranzi and G Corti. Material interaction cross section studies. Technical Report LHCb-INT-2011-002. CERN-LHCb-INT-2011-002, CERN, Geneva, Jan 2011.

[70] V.M. Abazov et al. Study of direct CP violation in $B^\pm \to J/\psi K^\pm(\pi^\pm)$ decays. *Phys.Rev.Lett.*, 100:211802, 2008.

[71] S Miglioranzi, M Clemencic, C Corti, S Easo, C R Jones, M Pappagallo, and P Robbe. The LHCb Simulation Application, Gauss: Design, Evolution and Experience. Jan 2011. LHCb-PROC-2011-006; CERN-LHCb-PROC-2011-006.

[72] David J. Lange. The evtgen particle decay simulation package. *Nuclear Instruments and Methods in Physics Research Section A: Accelerators, Spectrometers, Detectors and Associated Equipment*, 462(12):152 – 155, 2001.

[73] P. Golonka, B. Kersevan, T. Pierzchala, E. Richter-Was, Z. Was, et al. The Tauola photos F environment for the TAUOLA and PHOTOS packages: Release. 2. *Comput.Phys.Commun.*, 174:818–835, 2006.

[74] G Barrand. Panoramix. 2005. CERN-2005-002-V-1; CERN-2005-002-V-2.

[75] G Lanfranchi, X Cid Vidal, S Furcas, M Gandelman, J A Hernando, J H Lopez, E Polycarpo, and A Sarti. The muon identification procedure of the lhcb experiment for the first data. Technical Report LHCb-PUB-2009-013. CERN-LHCb-PUB-2009-013, CERN, Geneva, Aug 2009.

[76] Fitzpatrick. C. simpletools: Handy command line tools for ntuple manipulation and analysis. 2009. LHCb-INT-2009-029.

[77] Amato. S et al. Hlt1 muon alley description. LHCb-2008-058; CERN-LHCb-2008-058, 2008.

[78] Measurement of B-hadron masses with exclusive $J/\psi X$ decays in 2010 data. May 2011. LHCb-ANA-2011-027.

[79] W D Hulsbergen. Decay chain fitting with a kalman filter. *Nucl. Instrum. Methods Phys. Res., A*, 552(physics/0503191):566–575. 17 p, Mar 2005.

[80] Yuehong Xie. sFit: a method for background subtraction in maximum likelihood fit. Technical Report arXiv:0905.0724, May 2009.

[81] A Jaeger, P Seyfert, M De Cian, J van Tilburg, and S Hansmann-Menzemer. Tracking performance of the lhcb spectrometer. Oct 2011. Linked to LHCb-TALK-2011-207.

[82] Tomasz Skwarnicki. A study of the radiative cascade transitions between the upsilon-prime and upsilon resonances. DESY-F31-86-02.

[83] R. Aaji et al. A search for time-integrated CP violation in $D^0 \to h^+h^-$ decays and a measurement of the D^0 production asymmetry. Jun 2011. LHCb-ANA-2011-010.

[84] A. Raaji et al. Tagged time-dependent angular analysis of $B_s \to J/\psi\phi$ decays at LHCb. 2012. LHCb-CONF-2012-002.

[85] R. Aaij et al. Differential branching fraction and angular analysis of the decay $B^0 \to K^{*0}\mu^+\mu^-$. 2011. LHCB-PAPER-2011-020, CERN-PH-EP-2011-211.